A STUDY OF TIME-DEPENDENT MILD-SLOPE EQUATIONS

by

Changhoon Lee

RESEARCH REPORT NO. CACR-94-19
September, 1994

Center for Applied Coastal Research
Ocean Engineering Laboratory
University of Delaware
Newark, DE 19716

TABLE OF CONTENTS

Chapter

1 INTRODUCTION 1

1.1 Review of Wave Transformation Models 2
1.2 Review of Wave Breaking Models 7
1.3 Description of the Present Study 11

2 COMPARISON OF THE TIME-DEPENDENT MILD-SLOPE EQUATIONS 13

2.1 Analytical Comparison of the Model Equations 16
2.2 Comparisons of Model Equations for Bichromatic Waves 45

3 NEW TIME-DEPENDENT MILD-SLOPE EQUATIONS . . . 57

3.1 Derivation of New Time-Dependent Mild-Slope Equations 58
3.2 Finite Difference Methods 72
3.3 Test of a New Model for Bichromatic Waves 74

4 TIME-DEPENDENT MILD-SLOPE EQUATIONS FOR BREAKING WAVES 81

4.1 Derivation of a Model for Breaking Waves 82
4.2 Smoothing Energy Dissipation Rate 87

5 APPLICATIONS TO SEVERAL CASES 96

5.1 Specification of Boundary Conditions and Discretization 96
5.2 Applications for Non-Breaking Waves 102

5.2.1 Berkhoff, Booij and Radder Shoal Experiment (Two-dimensional Monochromatic Waves) 102
5.2.2 Vincent and Briggs Shoal Experiment (Two-dimensional Monochromatic and Random Waves) 106

5.3 Applications for Breaking Waves 118

5.3.1 Horikawa and Kuo Horizontal and Sloping Bottom Experiment (One-Dimensional Monochromatic Waves) . . 118
5.3.2 Mase and Kirby Plane Beach Experiment (One-dimensional Random Waves) 124
5.3.3 Vincent and Briggs Shoal Experiment (Two-Dimensional Monochromatic and Random Waves) 129

6 CONCLUSIONS 139
REFERENCES 142

Appendix

A PARABOLIC APPROXIMATIONS FOR BREAKING WAVES 147

LIST OF FIGURES

2.1 $\frac{\bar{k}^2}{\bar{\omega}}\frac{\partial}{\partial\omega}(\bar{C}\bar{C}_g)$: dashed line, $\frac{1}{\bar{\omega}}\frac{\partial}{\partial\omega}(\bar{k}^2\bar{C}\bar{C}_g)$: dash-dotted line 15

2.2 Exact linear dispersion relations 19

2.3 Percent errors in $k/\bar{k}$ for Smith and Sprinks' model 20

2.4 Percent errors in $k/\bar{k}$ for Kubo et al.'s model 20

2.5 Dispersion relations for $\bar{k}h = 2\pi$ (dotted line: 2 percent confidence interval of exact solution, dashed line: Smith and Sprinks' model, dash-dotted line: Kubo et al.'s model, solid line: linear Schrödinger equation) 21

2.6 Dispersion relations for $\bar{k}h = 0.3\pi$ (dotted line: 2 percent confidence interval of exact solution, dashed line: Smith and Sprinks' model, dash-dotted line: Kubo et al.'s model, solid line: linear Schrödinger equation) 22

2.7 Dispersion relations for $\bar{k}h = 0.05\pi$ (dotted line: 2 percent confidence interval of exact solution, dashed line: Smith and Sprinks' model, dash-dotted line: Kubo et al.'s model, solid line: linear Schrödinger equation) 23

2.8 Shoaling coefficients for $h_0 = 1\ m$ 24

2.9 Percent errors in shoaling coefficient for Smith and Sprinks' model ($h_0 = 1\ m$, $\bar{f} = 1\ Hz$) 25

2.10 Percent errors in shoaling coefficient for Kubo et al.'s model ($h_0 = 1\ m$, $\bar{f} = 1\ Hz$) 25

2.11 Power spectrum of water surface elevations measured at water depth of 47 cm by Mase and Kirby (1992): case 1 26

2.12 Squared shoaling coefficients K_{s0}^2 for linear wave 28

2.13 Percent errors in squared shoaling coefficients K_s^2 for Smith and Sprinks' model 29

2.14 Percent errors in squared shoaling coefficients K_s^2 for Kubo et al.'s model 29

2.15 Cumulative sum of power spectra in all water depths using K_{s0}^2 . 30

2.16 Percent errors in cumulative sum of power spectra in all water depths for Smith and Sprinks' model 31

2.17 Percent errors in cumulative sum of power spectra in all water depths for Kubo et al.'s model 31

2.18 Percent errors in total energy in all water depths when frequency bandwidth is equal (solid line: Smith and Sprinks' model using weight-averaged frequencies, dashed line: Smith and Sprinks' model using centered frequencies, dash-dotted line: Kubo et al.'s model using weight-averaged frequencies, dotted line: Kubo et al.'s model using centered frequencies) 33

2.19 Squared particle velocities at $z = 0$ 36

2.20 Percent errors in squared particle velocities at $z = 0$ (Smith and Sprinks' model with 4 frequency bands using weight-averaged frequencies) 37

2.21 Percent errors in squared particle velocities at $z = 0$ (Kubo et al.'s model with 4 frequency bands using weight-averaged frequencies) 37

2.22 Percent errors in variance of particle velocities at $z = 0$ when frequency bandwidth is equal (solid line: Smith and Sprinks' model using weight-averaged frequencies, dashed line: Smith and Sprinks' model using centered frequencies, dash-dotted line: Kubo et al.'s model using weight-averaged frequencies, dotted line: Kubo et al.'s model using centered frequencies) 38

2.23 Percent errors in variance of particle velocities at $z = -h$ when frequency bandwidth is equal (solid line: Smith and Sprinks' model using weight-averaged frequencies, dashed line: Smith and Sprinks' model using centered frequencies, dash-dotted line: Kubo et al.'s model using weight-averaged frequencies, dotted line: Kubo et al.'s model using centered frequencies) 39

2.24 $-\frac{\bar{k}^2}{\bar{\omega}}\frac{\bar{\omega}''}{2}$: solid line, $-\frac{\bar{k}^2}{\bar{\omega}}\frac{\bar{C}_g}{2\bar{\omega}}(\bar{C} - \bar{C}_g)$: dashed line, $-\frac{\bar{k}^2}{\bar{\omega}}\{\bar{\omega}'' + \frac{\bar{C}_g}{2\bar{\omega}}(2\bar{C}_g - \bar{C})\}$: dash-dotted line 43

2.25 Percent errors in $k/\bar{k}$ for linear Schrödinger equation 44

2.26 Water surface elevations for $\bar{k}h = 2\pi$, $\Delta k/\bar{k} = 0.15$ (solid line: exact solution, dashed line: Radder and Dingemans' model, dash-dotted line: Kubo et al.'s model) 51

2.27 Propagation of wave phase and wave groups for $\bar{k}h = 2\pi$, $\Delta k/\bar{k} = 0.15$ (dashed line: wave phase, dash-dotted line: wave groups) (a) Radder and Dingemans' model, (b) Kubo et al.'s model 52

2.28 Water surface elevations for $\bar{k}h = 0.3\pi$, $\Delta k/\bar{k} = 0.15$ (solid line: exact solution, dashed line: Radder and Dingemans' model, dash-dotted line: Kubo et al.'s model) 53

2.29 Propagation of wave phase and wave groups for $\bar{k}h = 0.3\pi$, $\Delta k/\bar{k} = 0.15$ (dashed line: wave phase, dash-dotted line: wave groups) (a) Radder and Dingemans' model, (b) Kubo et al.'s model 54

2.30 Water surface elevations for $\bar{k}h = 0.05\pi$, $\Delta k/\bar{k} = 0.15$ (solid line: exact solution, dashed line: Radder and Dingemans' model, dash-dotted line: Kubo et al.'s model) 55

2.31 Propagation of wave phase and wave groups for $\bar{k}h = 0.05\pi$, $\Delta k/\bar{k} = 0.15$ (dashed line: wave phase, dash-dotted line: wave groups) (a) Radder and Dingemans' model, (b) Kubo et al.'s model 56

3.1 α_3: dashed line, β_3: dash-dotted line 61

3.2 Percent errors in $k/\bar{k}$ for new model (3.7) 64

3.3 Percent errors in $k/\bar{k}$ for new model (3.14) 64

3.4 Dispersion relations for $\bar{k}h = 2\pi$ (dotted line: 2 percent confidence interval of exact solution, solid line: linear Schrödinger equation, dashed line: new model (3.7), dash-dotted line: new model (3.14)) 65

3.5 Dispersion relations for $\bar{k}h = 0.3\pi$ (dotted line: 2 percent confidence interval of exact solution, solid line: linear Schrödinger equation, dashed line: new model (3.7), dash-dotted line: new model (3.14)) 66

3.6 Dispersion relations for $\bar{k}h = 0.05\pi$ (dotted line: 2 percent confidence interval of exact solution, solid line: linear Schrödinger equation, dashed line: new model (3.7), dash-dotted line: new model (3.14)) 67

3.7 Percent errors in squared particle velocities at $z = 0$ (new model (3.7) with 4 frequency bands using weight-averaged frequencies) 69

3.8 Percent errors in squared particle velocities at $z = 0$ (new model (3.14) with 4 frequency bands using weight-averaged frequencies) 69

3.9 Percent errors in variance of particle velocities at $z = 0$ when frequency bandwidth is equal (solid line: new model (3.7) using weight-averaged frequencies, dashed line: new model (3.7) using centered frequencies, dash-dotted line: new model (3.14) using weight-averaged frequencies, dotted line: new model (3.14) using centered frequencies) 70

3.10 Percent errors in variance of particle velocities at $z = -h$ when frequency bandwidth is equal (solid line: new model (3.7) using weight-averaged frequencies, dashed line: new model (3.7) using centered frequencies, dash-dotted line: new model (3.14) using weight-averaged frequencies, dotted line: new model (3.14) using centered frequencies) 71

3.11 Water surface elevations for $\bar{k}h = 2\pi$, $\Delta k/\bar{k} = 0.15$ (solid line: exact solution, dashed line: new model (3.14), dash-dotted line: Kubo et al.'s model) 75

3.12 Propagation of wave phase and wave groups for $\bar{k}h = 2\pi$, $\Delta k/\bar{k} = 0.15$, new model (3.14) (dashed line: wave phase, dash-dotted line: wave groups) 76

3.13 Water surface elevations for $\bar{k}h = 0.3\pi$, $\Delta k/\bar{k} = 0.15$ (solid line: exact solution, dashed line: new model (3.14), dash-dotted line: Kubo et al.'s model) 77

3.14 Propagation of wave phase and wave groups for $\bar{k}h = 0.3\pi$, $\Delta k/\bar{k} = 0.15$, new model (3.14) (dashed line: wave phase, dash-dotted line: wave groups) 78

3.15 Water surface elevations for $\bar{k}h = 0.05\pi$, $\Delta k/\bar{k} = 0.15$ (solid line: exact solution, dashed line: new model (3.14), dash-dotted line: Radder and Dingemans' model) 79

3.16 Propagation of wave phase and wave groups for $\bar{k}h = 0.05\pi$, $\Delta k/\bar{k} = 0.15$, new model (3.14) (dashed line: wave phase, dash-dotted line: wave groups) 80

4.1 Geometric similarity between a hydraulic jump and a broken wave 83

4.2 One-dimensional simple smoothing (solid line: $n = 0$, dashed line: $n = 5$, dash-dotted line: $n = 10$, dotted line: n =15) (a) results, (b) spectral densities 89

4.3 Wave heights with different numbers of successive applications $n = 0, 5, 10$, and 15 (o: measured data, solid line: computed results, dashed line: results from shoaling coefficient) 91

4.4 Results after two-dimensional simple smoothing with $n = 0, 1, 2$, and 3 94

4.5 Spectral densities after two-dimensional simple smoothing with $n = 0, 1, 2$, and 3 (solid line: $n = 0$, dashed line: $n = 1$, dash-dotted line: $n = 2$, dotted line: $n = 3$) 95

5.1 Generated particle velocities $u(t)$ at wavemaker boundary $z = 0, x = 0$ for Mase and Kirby's (1992) case 1 with 6 frequency components (solid line: real part, dashed line: imaginary part) (a) first frequency component, (b) second frequency component, (c) third frequency component, (d) fourth frequency component, (e) fifth frequency component, (d) sixth frequency component . 98

5.2 Generated particle velocities $u(t)$ at wavemaker boundary $z = 0, x = 0, y = 45\ ft$ for Vincent and Briggs' (1989) case N5 with 3 frequency components (solid line: real part, dashed line: imaginary part) (a) first frequency component, (b) second frequency component, (c) third frequency component 100

5.3 Experimental setup by Berkhoff et al. (1982) 103

5.4 Comparison among linear model (dashed lines), nonlinear model (solid lines), and experimental data of Berkhoff et al. (1982) (section 1 - section4) 107

5.5 Comparison among linear model (dashed lines), nonlinear model (solid lines), and experimental data of Berkhoff et al. (1982) (section 5 - section8) 108

5.6 Experimental setup by Vincent and Briggs (1989) 109

5.7 TMA frequency spectra (narrow frequency band) and directional spreading functions (solid lines : $\sigma_0 = 10°$, dashed lines : $\sigma_0 = 30°$) 110

5.8 Water surface elevations at t = 260 s (case M2) 114

5.9 Water surface elevations at t = 260 s (case N4) 115

5.10 Water surface elevations at t = 260 s (case B4) 116

5.11 Measured and predicted normalized wave heights on section 4 for cases M2, N4, and B4 (o: measured wave height, solid line: predicted wave height) 117

5.12 Wave breaking parameters for Horikawa and Kuo's (1965) horizontal bottom with $T = 1\ s$, $h_c = 15\ cm$ (a) $\circ$: $(H/h)_b$, $*$: $(H/h)_r$, (b) $+$: γ 119

5.13 (a) Attenuation of wave height with different values of γ for $H_0/L_0 = 0.100$, $(H/h)_b = 0.89$, $(H/h)_r = 0.37$ (dashed line: $\gamma = 0.8$, solid line: $\gamma = 0.9$, dash-dotted line: $\gamma = 1.0$, dotted line: shoaling coefficient), (b) energy dissipation rates (D_b) for $H_0/L_0 = 0.100$, $(H/h)_b = 0.89$, $(H/h)_r = 0.37$, $\gamma = 0.9$ 120

5.14 Wave breaking parameters for 1/65 sloping bottom and $T = 1.6\ s$ (a) $\circ$: $(H/h)_b$, $*$: $(H/h)_r$, (b) γ 122

5.15 (a) Attenuation of wave height with different values of γ for $H_0/L_0 = 0.065$, $(H/h)_b = 0.78$, $(H/h)_r = 0.35$ (dashed line: $\gamma = 0.3$, solid line: $\gamma = 0.4$, dash-dotted line: $\gamma = 0.5$, dotted line: shoaling coefficient), (b) energy dissipation rates (D_b) for $H_0/L_0 = 0.065$, $(H/h)_b = 0.78$, $(H/h)_r = 0.35$, $\gamma = 0.4$. 123

5.16 Relation between $(H/h)_b$ and γ ($\circ$: horizontal bottom, dashed line: regression line for horizontal bottom, $*$: 1/65 sloping bottom, dash-dotted line: regression line for 1/65 sloping bottom) 124

5.17 Experimental setup by Mase and Kirby (1992) (Wei and Kirby, 1993) 125

5.18 Normalized wave heights (dashed line: measured data, solid line: whole frequency component, $\circ$: first frequency component, $*$: second frequency component, $\times$: third frequency component, $+$: fourth frequency component, $\circ$ and $\times$: fifth frequency component, $\circ$ and $+$: sixth component) 127

5.19 Water surface elevations from $t = 16\ s$ to $t = 160\ s$ at $16\ s$ interval for case 1 with 6 frequency bands 128

5.20 Energy dissipation rates $(D_b + D_s)$ from $t = 16\ s$ to $t = 160\ s$ at $16\ s$ interval for case 1 with 6 frequency bands 128

5.21 Water surface elevations at $t = 39$ s for case M3 with $(H/h)_b = 0.8$, $(H/h)_r = 0.35$ and $\gamma = 1$ (solid line: contour of water surface elevations, dashed line: contour of bottom topography, arrow: wave vector) 130

5.22 Energy dissipation rates (D_b) at $t = 39$ s for case M3 with $(H/h)_b = 0.8$, $(H/h)_r = 0.35$ and $\gamma = 1$ (solid line: contour of energy dissipation rates, dashed line: contour of bottom topography) 131

5.23 Water surface elevations from $t = 3.9$ s to $t = 39$ s at 3.9 s intervals along the center line parallel to x axis for case M3 with $(H/h)_b = 0.8$, $(H/h)_r = 0.35$ and $\gamma = 1$ 132

5.24 Energy dissipation rates (D_b) from $t = 3.9$ s to $t = 39$ s at 3.9 s intervals along the center line parallel to x axis for case M3 with $(H/h)_b = 0.8$, $(H/h)_r = 0.35$ and $\gamma = 1$ 133

5.25 Measured and computed normalized wave heights along section 4 for case M3 (o: measured data, solid line: computed results). . . 134

5.26 Water surface elevations at $t = 130$ s for case N5 (solid line: contour of water surface elevations, dashed line: contour of bottom topography) 135

5.27 Energy dissipation rates (D_b) at $t = 130$ s for case N5 (solid line: contour of energy dissipation rates, dashed line: contour of bottom topography) 136

5.28 Normalized wave heights along section 4 for case N5 (o: measured data, solid line: computed results) 136

5.29 Water surface elevations at $t = 130$ s for case B5 (solid line: contour of water surface elevations, dashed line: contour of bottom topography) 137

5.30 Energy dissipation rates (D_b) at $t = 130$ s for case B5 (solid line: contour of energy dissipation rates, dashed line: contour of bottom topography) 138

5.31 Normalized wave heights along section 4 for case B5 (o: measured data, solid line: computed results) 138

A.1 Separation of directional power spectra 150

LIST OF TABLES

5.1 Test conditions considered for Vincent and Briggs' (1989) shoal experiment (non-breaking waves) 111

5.2 Test conditions considered for Vincent and Briggs' (1989) shoal experiment (breaking waves) 129

Chapter 1

INTRODUCTION

Two thirds of the earth is covered by the ocean, supplying people with natural resources such as food, oil, recreation, etc., but also causing troubles such as storms with big waves. For a long time, people have been interested in how water waves are generated, how they are transformed, and finally how they break.

Water waves are generated mainly by the wind stress or other sources such as earthquakes, ship motions, or tides. Gentle winds at first disturb the calm water from time to time, producing small capillary waves. These local disturbances quickly die away. If the winds increase in speed, ripples develop on the surface. If the wind continues, gravity waves may develop. The longer and harder the wind blows, the larger the waves that are produced.

As waves leave the generation area, they spread out by wave dispersion, with the longest-period waves traveling the fastest. Viscous damping is important to the short-period waves but has little effect on the long-period waves. Acting together, wave dispersion and viscous damping narrow the wave spectrum and change the complex sea in the generation area to regular swell waves. Nonlinear effects such as wave-wave interaction continue for a short distance outside the generation area and are important in wave energy dissipation. Once waves have

reached a regular swell condition they may travel for thousands of kilometers across the entire ocean basin with relatively little additional energy loss.

As waves feel the bottom, they undergo the transformations of shoaling, refraction, and diffraction. The wave velocity and length progressively decrease, and the height increases with decreasing water depth (shoaling). The direction of wave propagation changes with decreasing depth of water, as the crests tend to parallel the depth contours (refraction). If breakwaters or other structures block the wave propagation, wave energy is shielded by the structures, creating a shadow zone (diffraction).

As the waves undergo further shoaling, the wave train becomes a series of peaked crests separated by relatively flat troughs. Finally, the crests become oversteepened and unstable, and they break. During wave breaking, there is an energy transformation from mechanical to heat energy resulting in energy dissipation. The breaking waves propagate until they reach a stable condition, after which they propagate without breaking; otherwise, they break until they disappear.

In the following sections, we review some wave transformation models and wave breaking models with statements why this study is motivated. Finally, we describe how this study proceeds.

1.1 Review of Wave Transformation Models

Wave refraction was first studied using a ray method by O'Brien (1942) for a single wave ray and generalized by Munk and Arthur (1952) for a set of rays. Wave rays, or lines which are everywhere normal to the wave crests, are assumed to be in the direction of wave advance and energy propagation. The wave amplitude

is calculated based on the assumption that the energy does not cross the rays, and so wave shoaling is included in the ray method. The main problem in the ray method is that because diffraction is not considered, the energy becomes infinite when the rays cross. Such problems in wave crossings can be overcome by methods such as that of Bouws and Battjes (1982), who estimated the wave energy from the rays passing through a number of subregions, each ray being considered as a carrier of a certain amount of wave power.

Diffraction of water waves around a semi-infinite breakwater was first solved analytically by Penney and Price (1952) based on Sommerfeld's (1896) solution in optics. Approximate solutions for waves diffracted behind a breakwater or a breakwater gap were also obtained by the method of superposition. If the water depth changes significantly near the breakwater, refraction is also important. For this case, ray models solving for each wave ray emanating radially from the breakwater tip have been developed by Larsen (1978) and Southgate (1985). However, these models cannot be used near ray crossings.

Combined refraction and diffraction was first studied by Ludwig (1966) in order to provide locally valid solutions for the Helmholtz equation near a caustic. The solution uses Airy functions, which are sinusoidal in the illuminated zone, damp exponentially in the shadow zone, and are transitional between sinusoidal and exponentially damping behavior in the vicinity of the caustic, with values of nearly double the incident wave on the caustic itself. The combined refraction and diffraction of water waves on a slowly varying bottom was studied by Berkhoff (1972), who derived the mild-slope equation:

$$\nabla \cdot (CC_g \nabla \hat{\phi}) + k^2 CC_g \hat{\phi} = 0 \tag{1.1}$$

where ∇ is the horizontal gradient operator, k is the local wavenumber, C and C_g are phase and group velocities, respectively, and the function $\hat{\phi}$ is related to the

velocity potential ϕ by

$$\phi = \frac{\cosh k(z+h)}{\cosh kh}\hat{\phi}e^{-i\omega t} \tag{1.2}$$

Berkhoff's equation (1.1) is applicable only to monochromatic waves and is of elliptic type, so it requires the surrounding boundary conditions and significant work on efficient solution methods.

A time-dependent mild-slope equation was first developed by Smith and Sprinks (1975) by means of Green's second identities applied to the velocity potential. The model equation is

$$\frac{\partial^2 \tilde{\phi}}{\partial t^2} - \nabla \cdot (\bar{C}\bar{C}_g \nabla \tilde{\phi}) + (\bar{\omega}^2 - \bar{k}^2 \bar{C}\bar{C}_g)\tilde{\phi} = 0 \tag{1.3}$$

where $\bar{C}$ and $\bar{C}_g$ are phase and group velocities, respectively, of a narrow-banded wave with carrier angular frequency $\bar{\omega}$ and wavenumber $\bar{k}$. The function $\tilde{\phi}$ is related to the velocity potential ϕ by

$$\phi = \frac{\cosh \bar{k}(z+h)}{\cosh \bar{k}h}\tilde{\phi} \tag{1.4}$$

The time-dependent mild-slope equation (1.3) reproduces Berkhoff's equation (1.1) for monochromatic waves and reproduces the long wave equation in shallow water.

A system of the time-dependent mild-slope equations was derived based on the Hamiltonian theory of water waves by Radder and Dingemans (1985). The model equations are

$$\frac{\partial \eta}{\partial t} = -\nabla \cdot (\frac{\bar{C}\bar{C}_g}{g}\nabla \tilde{\phi}) + \frac{(\bar{\omega}^2 - \bar{k}^2 \bar{C}\bar{C}_g)}{g}\tilde{\phi} \tag{1.5}$$

$$\frac{\partial \tilde{\phi}}{\partial t} = -g\eta \tag{1.6}$$

where g is the gravitational acceleration. The water surface elevation η may be eliminated from equations (1.5) and (1.6) in order to obtain Smith and Sprinks' equation (1.3).

The time-dependent mild-slope equation was extended by Booij (1981) to include the effects of ambient currents using a variational principle. Some errors were corrected by Kirby (1984) to obtain the model equation

$$\frac{D^2\tilde{\phi}}{Dt^2} + (\nabla \cdot \mathbf{U})\frac{D\tilde{\phi}}{Dt} - \nabla \cdot (\bar{C}\bar{C}_g \nabla\tilde{\phi}) + (\bar{\sigma}^2 - \bar{k}^2\bar{C}\bar{C}_g)\tilde{\phi} = 0 \tag{1.7}$$

where the total derivative $\frac{D}{Dt}$ is

$$\frac{D}{Dt} = (\frac{\partial}{\partial t} + \mathbf{U} \cdot \nabla), \tag{1.8}$$

$\mathbf{U}(x, y)$ is the ambient current and $\bar{\sigma}$ is the wave intrinsic frequency which satisfies the dispersion relation

$$\bar{\sigma}^2 = (\bar{\omega} - \bar{\mathbf{k}} \cdot \mathbf{U})^2 = g\bar{k} \tanh \bar{k}h. \tag{1.9}$$

Recently, a time-dependent mild-slope equation for linear waves under the combined effects of depth variation and rotation was developed by Kirby and Lee (1993). The model equation is

$$\frac{\partial^3\eta}{\partial t^3} - \nabla \cdot (gF_1\nabla\frac{\partial\eta}{\partial t}) + \epsilon^2\bar{\omega}^2\frac{\partial\eta}{\partial t} + gF_2(1-\epsilon^2)\frac{\partial\eta}{\partial t} - \frac{\epsilon g\bar{\omega}}{\cosh^2\bar{\lambda}h}J(h,\eta) = 0 \tag{1.10}$$

where

$$F_1 = \int_{-h}^{0} (\frac{\cosh\bar{\lambda}(h+z)}{\cosh\bar{\lambda}h})^2 dz \tag{1.11}$$

$$F_2 = \int_{-h}^{0} (\frac{\partial}{\partial z}(\frac{\cosh\bar{\lambda}(h+z)}{\cosh\bar{\lambda}h}))^2 dz, \tag{1.12}$$

$\epsilon = f/\bar{\omega}$ is the inverse Rossby number, $J(h,\eta)$ is the Jacobian of h and η, and $\bar{\lambda}$ is the inverse length scale of the vertical variation of the pressure and horizontal velocity fields, and gives the dispersion relation

$$\bar{\omega}^2 = g\bar{\lambda}\tanh\bar{\lambda}h. \tag{1.13}$$

The model reproduces the usual finite-depth mild-slope equation (1.3) in the absence of rotation, and also reproduces the long wave equation when the ratio of

wavelength to water depth is large, either with or without the additional effect of rotation.

If waves are progressive and the deviation of the wave direction from an assumed principal direction is small, the parabolic approximation, which is more efficient than the mild-slope equation (which is either hyperbolic (equations (1.3), (1.5) and (1.6), (1.7), (1.10)) or elliptic (equation (1.1))), may be used. The parabolic approximation uses the fact that in the shadow boundary of a scatter, the modulation of wave amplitude is more rapid in the direction tangential to wave fronts than in the direction of wave rays. The basic idea was originated for electromagnetic waves by Leontovich and Fock (1944). For water waves, the first application was given by Liu and Mei (1976), who found the linearized wave field in the neighborhood of a breakwater on a beach with parallel depth contours. For two-dimensional bathymetry the first extension was given by Radder (1979), who developed a parabolic approximation to Berkhoff's equation (1.1) based on the use of a splitting matrix, which divides the wave field into transmitted and reflected components, and assumes the reflected field is negligible. The nonlinearity which is significant near the focal region was considered in the parabolic approximations by Kirby and Dalrymple (1983). The restriction to small angles can be relaxed by adding higher order derivatives; see Kirby (1986). A model for very wide-angle diffraction was developed by Dalrymple and Kirby (1988), Dalrymple et al. (1989) and was extended to nonlinear Stokes waves by Suh et al. (1990). They decomposed the entire wave field into an angular spectrum by applying a Fourier transformation with respect to alongshore coordinate to the mild-slope equation. Therefore, the model is limited to the assumption of periodicity in the alongshore direction.

Recently, Kirby et al. (1992) presented a number of computations using

Radder and Dingemans' equations (1.5) and (1.6), and extended those to progressive nonlinear Stokes waves. At the same time, Kubo et al. (1992) have developed a different type of time-dependent mild-slope equation

$$\nabla \cdot (\bar{C}\bar{C}_g \nabla \hat{\phi}) + \bar{k}^2 \bar{C}\bar{C}_g \hat{\phi} + i\nabla \cdot (\frac{\partial}{\partial \omega}(\bar{C}\bar{C}_g)\nabla \frac{\partial \hat{\phi}}{\partial t}) + i\frac{\partial}{\partial \omega}(\bar{k}^2 \bar{C}\bar{C}_g)\frac{\partial \hat{\phi}}{\partial t} = 0 \quad (1.14)$$

which was derived by extending the terms CC_g and k^2CC_g in Berkhoff's equation (1.1) into Taylor series in $\Delta\omega$, and eliminating powers of $\Delta\omega$ using the relation $\frac{\partial \hat{\phi}}{\partial t} = -i\Delta\omega\hat{\phi}$ for narrow-banded spectra. They also showed the propagation of the wave groups to verify the linear dispersive properties of the model equation.

The analysis of the dispersion relation and modulation of wave amplitudes (which is described in detail in Chapter 2) reveals that Smith and Sprinks' equation (1.3) (or, equivalently, Radder and Dingemans' equations (1.5) and (1.6)) is more accurate in shallower water ($\bar{k}h \leq 0.2\pi$) and Kubo et al.'s equation (1.14) is more accurate in deeper water ($\bar{k}h > 0.2\pi$). So, a new time-dependent mild-slope equation is needed which is most accurate in whole range of water depth.

1.2 Review of Wave Breaking Models

Three types of breakers are commonly recognized; spilling, plunging, and surging. In spilling breakers the wave gradually peaks until the crest becomes unstable and cascades down as white water. In plunging breakers the shoreward face of the wave becomes vertical, curls over, and plunges down as an intact mass of water. Surging breakers peak up as if to plunge, but then the base of the wave surges up the beach face so that the crest collapses and disappears. In general, spilling breakers tend to occur on beaches of very low slope, plunging breakers are associated with steeper beaches and waves of intermediate steepness, and surging occurs on high-gradient beaches with waves of low steepness (Patrick

and Wiegel, 1955). Galvin (1968) identifies a fourth type of breaking waves, a collapsing breaker, which is intermediate between plunging and surging types. He has established that this sequence (with gradual transitions) corresponds to increasing values of $\frac{H_0}{L_0 s^2}$ or $\frac{H_b}{gT^2 s^2}$, where H is the wave height, L is the wavelength, T is the wave period, s is the beach slope and subscripts 0 and b represents the value at deep water and breaking point, respectively.

The most basic of the breaking criteria is that if the velocity of the water at the crest exceeds the phase velocity of the wave form the crest will topple forward and break. Two breaking criteria can be specified in deep and shallow water depths. In deep water, the wave steepness is significant in determining the breaking criteria. Michell (1893) found theoretically the breaking criteria

$$(\frac{H}{L})_b = 0.142 \tag{1.15}$$

which is valid only in deep water. The limiting steepness for progressive waves in any depth of water is given by Miche (1944) as

$$(\frac{H}{L})_b = 0.142 \tanh(\frac{2\pi h}{L})_b \tag{1.16}$$

In shallow water, the wave height to water depth ratio becomes significant in determining the breaking criteria. McCowan (1891) found the breaking criteria for a solitary wave to be

$$(\frac{H}{h})_b = 0.78 \tag{1.17}$$

Field measurements on ocean beaches with very low gradients reported by Sverdrup and Munk (1947) agreed with the value of McCowan's breaking criteria, so this value has been widely accepted. Iversen (1951) found that, on laboratory beaches, higher breaking criteria exist on beaches with steeper slopes and the breaker height index $\frac{H_b}{H_0}$ decreases with increasing incident wave steepness.

The steady state equation for the wave breaking models is

$$\frac{\partial}{\partial x}(EC_g) = -D_b E \tag{1.18}$$

where E is the wave energy per unit surface area and D_b is the energy dissipation rate. Breaking models can be separated into three main categories: those that resolve the instantaneous state of motion, treating the breaking wave as a bore; those that give a more global description of the waves in terms of spatial variation of their integral properties, treating the sea locally as a uniform wave train; and those that use experimental data.

For the first category, treating the breaking wave as a bore, Lamb (1932) derived the energy dissipation rate per unit span for breaking waves using conservation of mass and momentum across a bore connecting two regions of uniform flow. Battjes and Janssen (1978) derived a model to predict the dissipation rate for random breaking waves using a bore of the corresponding height while the probability of the occurrence of the wave breaking is estimated by a Rayleigh distribution with an upper cut-off. Thornton and Guza (1983) derived the energy dissipation rate for random breaking waves using observed wave distributions. Svendsen (1984) developed a dimensionless energy dissipation rate which depends on wave height to water depth ratio and wave crest elevation to wave height ratio.

For the second category, treating the sea locally as a uniform wave train, Dally et al. (1985) proposed that the energy dissipation rate for regular breaking waves is proportional to the excess of energy flux over a pre-determined stable value. This was motivated by Horikawa and Kuo's (1966) experimental data where it was observed that the decay of wave heights of breaking waves stops when they reach a stable wave height, with a wave height to water depth ratio of 0.35 to 0.4. Dally et al.'s dissipation rate was extended to random breaking

waves by Dally and Dean (1986) and also was extended to the parabolic mild-slope equation by Kirby and Dalrymple (1986).

For the third category, Isobe (1987) developed an energy dissipation rate based on experimental data as

$$\begin{aligned} D_b &= \frac{5}{4} s \sqrt{\frac{g}{h}} \sqrt{\frac{\gamma - \gamma_\tau}{\gamma_s - \gamma_\tau}} \sqrt{\frac{\tanh kh}{kh}} (1 + s_2) \\ &\quad \cdot \{1 - \frac{5(1 - s_2)(1 + s_2) + 2s_2(s_2 \cosh 2kh - 1)}{5(1 + s_2)^2}\} \end{aligned} \tag{1.19}$$

where

$$s_2 = \frac{2kh}{\sinh 2kh}, \tag{1.20}$$

s is the bottom slope, γ is the ratio of water particle velocity to wave phase velocity, and γ_s and γ_τ are the values at the wave recovery point and on bottom of uniform slope, respectively, determined by

$$\gamma_s = 0.4(0.57 + 5.3s) \tag{1.21}$$

$$\gamma_\tau = 0.135 \tag{1.22}$$

Isobe used a breaking criterion proposed by Watanabe et al. (1984), who employed the ratio of water particle velocity to wave phase velocity as a breaker index in order to predict the breaking point accurately in the linear wave analysis. The breaking criterion is

$$\gamma_b = 0.53 - 0.3e^{-3\sqrt{h_b/L_0}} + 5s^{\frac{3}{2}} e^{-45(\sqrt{h_b/L_0} - 0.1)^2} \tag{1.23}$$

Kubo et al. (1992) modified the energy dissipation rate in equation (1.19) as dimensionless variable given by

$$f_{D_b} = \frac{5}{2} s \sqrt{\frac{\gamma - \gamma_\tau}{\gamma_s - \gamma_\tau}} \sqrt{\frac{1}{kh}} \tag{1.24}$$

and used the energy dissipatation rate in the time-dependent mild-slope equation (1.14) resulting in

$$\nabla\cdot(\bar{C}\bar{C}_g\nabla\hat{\phi})+\bar{k}^2\bar{C}\bar{C}_g(1+if_{D_b})\hat{\phi}+i\nabla\cdot(\frac{\partial}{\partial\omega}(\bar{C}\bar{C}_g)\nabla\frac{\partial\hat{\phi}}{\partial t})+\frac{\partial}{\partial\omega}(\bar{k}^2\bar{C}\bar{C}_g)(1+if_{D_b})\frac{\partial\hat{\phi}}{\partial t}=0 \tag{1.25}$$

The equations (1.19) and (1.23) were derived semi-empirically for a uniformly sloping bottom, and were used on non-uniformly sloping bottoms by assuming the points on the bottoms are locally uniform.

The time-dependent mild-slope equation is applicable from deep to shallow water. To extend the model to the surf zone, we need a wave breaking model to be included in the time-dependent mild-slope equation. The breaking model should be applicable for a complicated bottom slope and should dictate the propagation of the breaking waves with decay of wave height until a stable condition is reached.

1.3 Description of the Present Study

The natural phenomenon of wave propagation is highly complicated with nonlinearity and turbulence. So, we need to simplify the problem to get a solution. First, we assume the water to be incompressible and irrotational, which enables us to use the velocity potential. Second, we neglect the viscous effects of water near the bottom and the water surface. Third, we neglect the nonlinear wave-wave interactions.

In Chapter 2, we compare the two time-dependent mild-slope equations (1.3) (or, equivalently, (1.5) and 1.6)) and (1.14) in terms of the dispersion relation, energy transport, modulation of wave amplitudes, and also by theoretical and numerical analysis for bichromatic waves.

In Chapter 3, we derive two new time-dependent mild-slope equations

which satisfy the linear Schrödinger equation for the modulation of wave amplitudes and compare these equations with the two existing time-dependent mild-slope equations in terms of the dispersion relation, energy transport, and also by numerical simulation for bichromatic waves in order to verify that the new equation is more accurate than the existing equations.

In Chapter 4, we derive an energy dissipation rate caused by wave breaking using the geometric similarity between a breaking wave and a bore, and include the dissipation rate in the time-dependent mild-slope equations. A method of successive 3 point averaging is suggested for use during computation to get stable solutions.

In Chapter 5, we apply non-breaking and breaking versions of Radder and Dingemans' model to several cases including one-dimensional and two-dimensional, monochromatic and random, and non-breaking and breaking waves.

In Chapter 6, we summarize this study and conclude with some suggestions for further study.

Chapter 2

COMPARISON OF THE TIME-DEPENDENT MILD-SLOPE EQUATIONS

The combined refraction and diffraction of water waves on a slowly varying bottom was studied by Berkhoff (1972) using the mild-slope equation:

$$\nabla \cdot (CC_g \nabla \hat{\phi}) + k^2 CC_g \hat{\phi} = 0 \tag{2.1}$$

where ∇ is the horizontal gradient operator, k is the local wavenumber, C and C_g are phase and group velocities, respectively, and the function $\hat{\phi}$ is related to the velocity potential ϕ by

$$\phi = \frac{\cosh k(z+h)}{\cosh kh} \hat{\phi} e^{-i\omega t} \tag{2.2}$$

Berkhoff's equation (2.1) is applicable only to monochromatic waves.

A time-dependent mild-slope equation was first developed by Smith and Sprinks (1975) by means of Green's second identities applied to the velocity potential. The model equation is

$$\frac{\partial^2 \tilde{\phi}}{\partial t^2} - \nabla \cdot (\bar{C}\bar{C}_g \nabla \tilde{\phi}) + (\bar{\omega}^2 - \bar{k}^2 \bar{C}\bar{C}_g)\tilde{\phi} = 0 \tag{2.3}$$

where $\bar{C}$ and $\bar{C}_g$ are phase and group velocities, respectively, of a narrow-banded wave with carrier angular frequency $\bar{\omega}$ and wavenumber $\bar{k}$. The function $\tilde{\phi}$ is related to the velocity potential ϕ by

$$\phi = \frac{\cosh \bar{k}(z+h)}{\cosh \bar{k}h} \tilde{\phi} \tag{2.4}$$

A system of the time-dependent mild-slope equations was derived based on the Hamiltonian theory of water waves by Radder and Dingemans (1985). The model equations are

$$\frac{\partial \eta}{\partial t} = -\nabla \cdot (\frac{\bar{C}\bar{C}_g}{g}\nabla\tilde{\phi}) + \frac{(\bar{\omega}^2 - \bar{k}^2\bar{C}\bar{C}_g)}{g}\tilde{\phi} = F(\tilde{\phi}) \tag{2.5}$$

$$\frac{\partial \tilde{\phi}}{\partial t} = -g\eta \tag{2.6}$$

The water surface elevation η may be eliminated from equations (2.5) and (2.6) in order to obtain Smith and Sprinks' equation (2.3).

Kirby et al. (1992) presented a number of computations using the time-dependent mild-slope equations (2.5) and (2.6). They studied the propagation of wave groups in order to verify the linear dispersive properties of the model, and then tested the model against several existing data sets, including the wave focusing experiments by Berkhoff et al. (1982) (monochromatic waves) and Vincent and Briggs (1989) (monochromatic and random waves).

Kubo et al. (1992) developed a different type of time-dependent mild-slope equation

$$\nabla \cdot (\bar{C}\bar{C}_g\nabla\hat{\phi}) + \bar{k}^2\bar{C}\bar{C}_g\hat{\phi} + i\nabla \cdot (\frac{\partial}{\partial\omega}(\bar{C}\bar{C}_g)\nabla\frac{\partial\hat{\phi}}{\partial t}) + i\frac{\partial}{\partial\omega}(\bar{k}^2\bar{C}\bar{C}_g)\frac{\partial\hat{\phi}}{\partial t} = 0 \tag{2.7}$$

which was derived by extending the terms CC_g and k^2CC_g in Berkhoff's equation (2.1) in Taylor series in $\Delta\omega$, and then substituting for $\Delta\omega$ using the relation $\frac{\partial\hat{\phi}}{\partial t} = -i\Delta\omega\hat{\phi}$ for narrow banded spectra. They also showed the propagation of wave groups to verify the linear dispersive properties of the model. The last two terms in equation (2.7) are added in order to correct Berkhoff's equation (2.1) for time-dependent problems. The values of the terms $\frac{\partial}{\partial\omega}(\bar{C}\bar{C}_g)$ and $\frac{\partial}{\partial\omega}(\bar{k}^2\bar{C}\bar{C}_g)$ are given by

$$\frac{\partial}{\partial\omega}(\bar{C}\bar{C}_g) = \frac{\bar{\omega}}{\bar{k}^2}(\frac{\bar{C}_g}{\bar{C}} - 1 + \frac{\bar{k}\bar{\omega}''}{\bar{C}_g})$$

$$= \frac{\bar{\omega}}{\bar{k}^2}\{2(\bar{n}-1)+\frac{2\bar{n}-1}{2\bar{n}}(1-(2\bar{n}-1)\cosh 2\bar{k}h)\} \quad (2.8)$$

$$\frac{\partial}{\partial\omega}(\bar{k}^2\bar{C}\bar{C}_g) = 2\bar{\omega}+\bar{k}^2\frac{\partial}{\partial\omega}(\bar{C}\bar{C}_g)$$

$$= \bar{\omega}\{2\bar{n}+\frac{2\bar{n}-1}{2\bar{n}}(1-(2\bar{n}-1)\cosh 2\bar{k}h)\} \quad (2.9)$$

where $\bar{n}=\bar{C}_g/\bar{C}=\frac{1}{2}(1+\frac{2\bar{k}h}{\sinh 2\bar{k}h})$.

The values of $\frac{\bar{k}^2}{\bar{\omega}}\frac{\partial}{\partial\omega}(\bar{C}\bar{C}_g)$ and $\frac{1}{\bar{\omega}}\frac{\partial}{\partial\omega}(\bar{k}^2\bar{C}\bar{C}_g)$ are shown in Figure 2.1, from which we see that the second to last term in equation (2.7) becomes zero in very shallow water and the last term becomes $+i\bar{\omega}\frac{\partial\hat{\phi}}{\partial t}$ and $+2i\bar{\omega}\frac{\partial\hat{\phi}}{\partial t}$ in very deep and shallow waters, respectively.

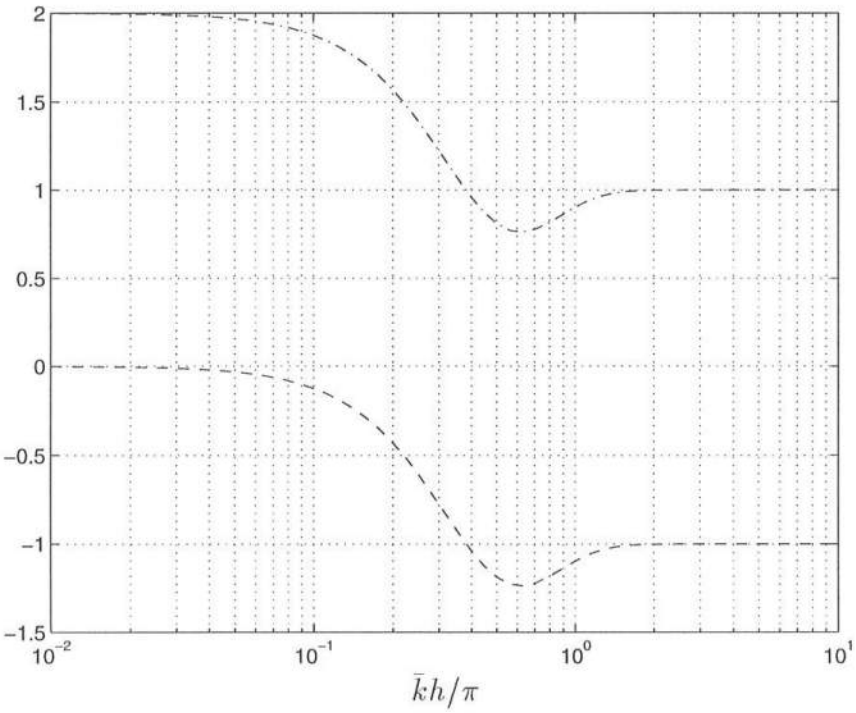

Figure 2.1: $\frac{\bar{k}^2}{\bar{\omega}}\frac{\partial}{\partial\omega}(\bar{C}\bar{C}_g)$: dashed line, $\frac{1}{\bar{\omega}}\frac{\partial}{\partial\omega}(\bar{k}^2\bar{C}\bar{C}_g)$: dash-dotted line

First, we compare the two models (2.3) (or, equivalently, (2.5) and (2.6))

and (2.7) from a geometric optics point of view, which yields the dispersion relation and the transport equation for wave energy. Secondly, we compare the two models in terms of wave kinematics, that is, we see how well the two models approximate particle velocities u for some examples. Thirdly, we compare the two models one-dimensionally in the horizontal direction for constant water depth against the linear Schrödinger equation, which is the equation for modulation of wave amplitudes accurate to $O(\Delta k)^2$ and serves as a benchmark for other leading order envelope equations. Fourthly, bichromatic waves are simulated numerically to see how well the two models predict the propagation of wave phase and groups against exact solutions.

2.1 Analytical Comparison of the Model Equations

For the case where variation in the wave train is very slow relative to variations in the domain topography, the propagation of surface waves is often treated from the geometric optics point of view, which leads to the usual ray approximation.

For Smith and Sprinks' model, the geometric optics approximation is constructed by substituting the ansatz

$$\tilde{\phi}(x,y,t) = A(x,y,t)e^{i(\int k_x dx + \int k_y dy - \omega t)} \tag{2.10}$$

where $A(x,y,t)$ is a complex amplitude which modulates in space and time and k_x and k_y are local wavenumbers in x and y directions, into equation (2.3), which yields

$$-(\omega^2 - \bar{\omega}^2)A + (k^2 - \bar{k}^2)\bar{C}\bar{C}_g A - \nabla\cdot(\bar{C}\bar{C}_g\nabla A) - i\frac{1}{A}\nabla\cdot(A^2\mathrm{k}\bar{C}\bar{C}_g) = 0 \tag{2.11}$$

Separation of real and imaginary part of the resulting equation leads to an eikonal equation for the phase function

$$\frac{\omega^2 - \bar{\omega}^2}{\bar{C}\bar{C}_g} = k^2 - \bar{k}^2 - \frac{\nabla \cdot (\bar{C}\bar{C}_g \nabla A)}{\bar{C}\bar{C}_g A} \tag{2.12}$$

and a transport equation for wave energy

$$\nabla \cdot (A^2 \mathbf{k} \bar{C}\bar{C}_g) = 0 \tag{2.13}$$

It is usually assumed that for bottom of small slopes, the last term in equation (2.12) is second order in the small parameter and thus negligibly small (Keller, 1958). Retention of the small term allows for the inclusion of weak diffraction corrections in grid-based refraction schemes. Neglecting terms that are second-order small in equation (2.12) leads to the following dispersion relation

$$\frac{k}{\bar{k}} = \sqrt{1 + \frac{(\frac{\omega}{\bar{\omega}})^2 - 1}{\bar{n}}} \tag{2.14}$$

For Kubo et al.'s model, the geometric optics approximation is constructed by substituting the ansatz

$$\hat{\phi}(x, y, t) = \tilde{\phi} e^{i\bar{\omega}t} = A(x, y, t) e^{i(\int k_x dx + k_y dy - (\omega - \bar{\omega})t)} \tag{2.15}$$

into equation (2.7), which yields

$$\begin{aligned} &(\omega - \bar{\omega})\{\frac{\partial}{\partial \omega}(\bar{k}^2 \bar{C}\bar{C}_g) - k^2 \frac{\partial}{\partial \omega}(\bar{C}\bar{C}_g)\}A - (k^2 - \bar{k}^2)\bar{C}\bar{C}_g A + \nabla \cdot (\bar{C}\bar{C}_g \nabla A) \\ &+(\omega - \bar{\omega})\nabla \cdot (\frac{\partial}{\partial \omega}(\bar{C}\bar{C}_g)\nabla A) + i\frac{1}{A}\nabla \cdot [A^2 \mathbf{k}\{\bar{C}\bar{C}_g + (\omega - \bar{\omega})\frac{\partial}{\partial \omega}(\bar{C}\bar{C}_g)\}] = 0 \end{aligned} \tag{2.16}$$

Separation of the real and imaginary part of the resulting equation leads to an eikonal equation for the phase function

$$\begin{aligned} &\frac{\omega - \bar{\omega}}{\bar{C}\bar{C}_g}\{\frac{\partial}{\partial \omega}(\bar{k}^2 \bar{C}\bar{C}_g) - k^2 \frac{\partial}{\partial \omega}(\bar{C}\bar{C}_g)\} \\ &= k^2 - \bar{k}^2 - \frac{\nabla \cdot (\bar{C}\bar{C}_g \nabla A)}{\bar{C}\bar{C}_g A} - (\omega - \bar{\omega})\frac{\nabla \cdot (\frac{\partial}{\partial \omega}(\bar{C}\bar{C}_g)\nabla A)}{\bar{C}\bar{C}_g A} \end{aligned} \tag{2.17}$$

and a transport equation for wave energy

$$\nabla \cdot [A^2 \mathbf{k}\{\bar{C}\bar{C}_g + (\omega - \bar{\omega})\frac{\partial}{\partial \omega}(\bar{C}\bar{C}_g)\}] = 0 \tag{2.18}$$

The last two terms in equation (2.17) represent weak diffraction with additional correcting term obtained by Taylor series expansion. Neglecting diffraction terms in equation (2.17) leads to the following dispersion relation

$$\frac{k}{\bar{k}} = \sqrt{1 + \frac{2(\frac{\omega}{\bar{\omega}} - 1)}{\bar{n} + (\frac{\omega}{\bar{\omega}} - 1)\frac{\bar{k}^2}{\bar{\omega}}\frac{\partial}{\partial \omega}(\bar{C}\bar{C}_g)}} \tag{2.19}$$

These dispersion relations, equations (2.14) and (2.19), can be compared against the exact dispersion relation for linear wave:

$$(\frac{\omega}{\bar{\omega}})^2 = \frac{k}{\bar{k}}\frac{\tanh \frac{k}{\bar{k}}\bar{k}h}{\tanh \bar{k}h} \tag{2.20}$$

The exact dispersion relation is shown in Figure 2.2. The percent errors in $k/\bar{k}$ for Smith and Sprinks' model and Kubo et al.'s model are shown in Figures 2.3 and 2.4, which show that Kubo et al.'s model gives closer dispersion relation to the exact dispersion relation in deep and intermediate-depth waters, whereas Smith and Sprinks' model gives closer dispersion relation in shallow water. Figures 2.5 - 2.7 show the dispersion relations for exact solution, Smith and Sprinks' model, Kubo et al.'s model, and the linear Schrödinger equation in deep water ($\bar{k}h = 2\pi$), intermediate-depth water ($\bar{k}h = 0.3\pi$), and in shallow water ($\bar{k}h = 0.05\pi$). The dispersion relation for the linear Schrödinger equation is described by equation (2.35) which is accurate to $O(\Delta k)^2$. At deep water with $\bar{k}h = 2\pi$, Smith and Sprinks' model has lower valid boundary of $\omega/\bar{\omega} = 0.7$ and Kubo et al.'s model has lower valid boundary of $\omega/\bar{\omega} = 0.5$. At intermediate-depth water with $\bar{k}h = 0.3\pi$, Smith and Sprinks' model has lower valid boundary of $\omega/\bar{\omega} = 0.45$ and Kubo et al.'s model has lower valid boundary of $\omega/\bar{\omega} = 0.35$. At shallow water with

$\bar{k}h = 0.05\pi$, Smith and Sprinks' model has lower valid boundary of $\omega/\bar{\omega} = 0.1$ and Kubo et al.'s model has lower valid boundary of $\omega/\bar{\omega} = 0.5$. The upper range of $\omega/\bar{\omega}$ for valid solutions is much larger than the lower range of $\omega/\bar{\omega}$ for valid solutions.

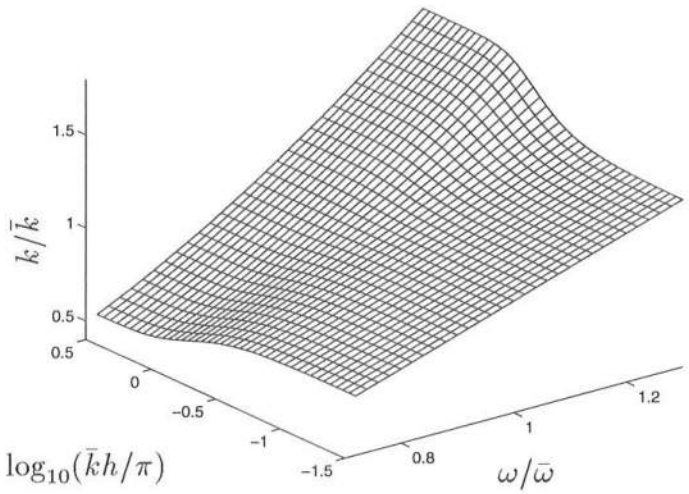

Figure 2.2: Exact linear dispersion relations

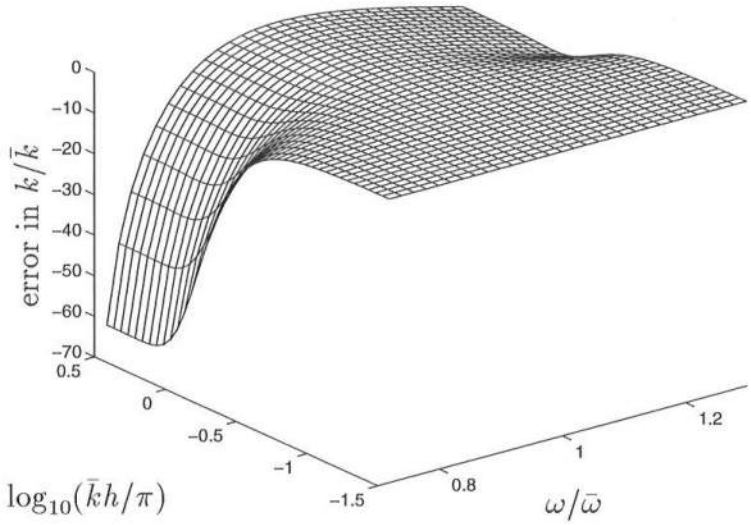

Figure 2.3: Percent errors in $k/\bar{k}$ for Smith and Sprinks' model

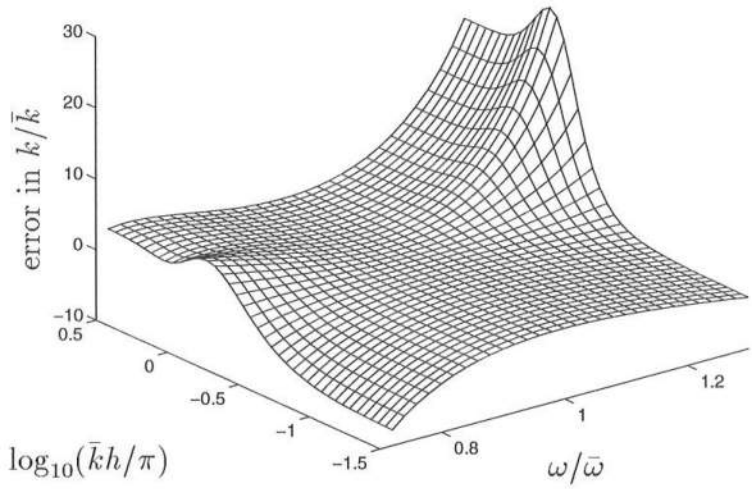

Figure 2.4: Percent errors in $k/\bar{k}$ for Kubo et al.'s model

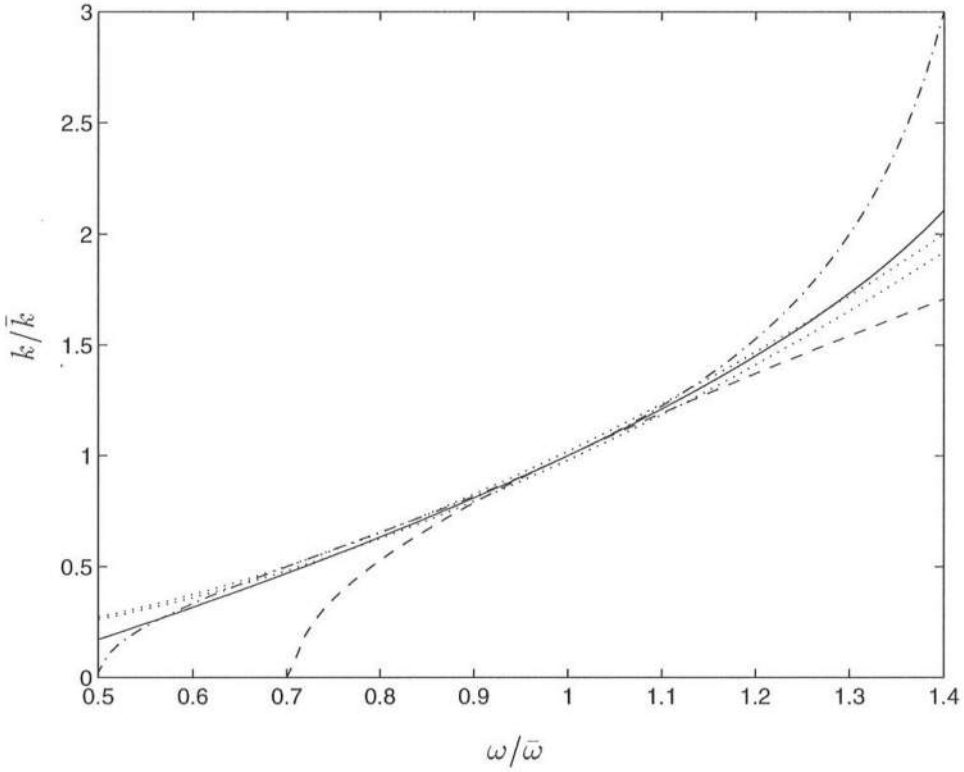

Figure 2.5: Dispersion relations for $\bar{k}h = 2\pi$ (dotted line: 2 percent confidence interval of exact solution, dashed line: Smith and Sprinks' model, dash-dotted line: Kubo et al.'s model, solid line: linear Schrödinger equation)

The transport equations for wave energy can be compared against the transport equation for the linear wave energy:

$$\nabla \cdot (A^2 \mathbf{k} C C_g) = 0 \tag{2.21}$$

The exact linear shoaling coefficient can be obtained from equation (2.21) as

$$K_{s0} = \frac{A}{A_0} = \sqrt{\frac{C_{g0}}{C_g}} \tag{2.22}$$

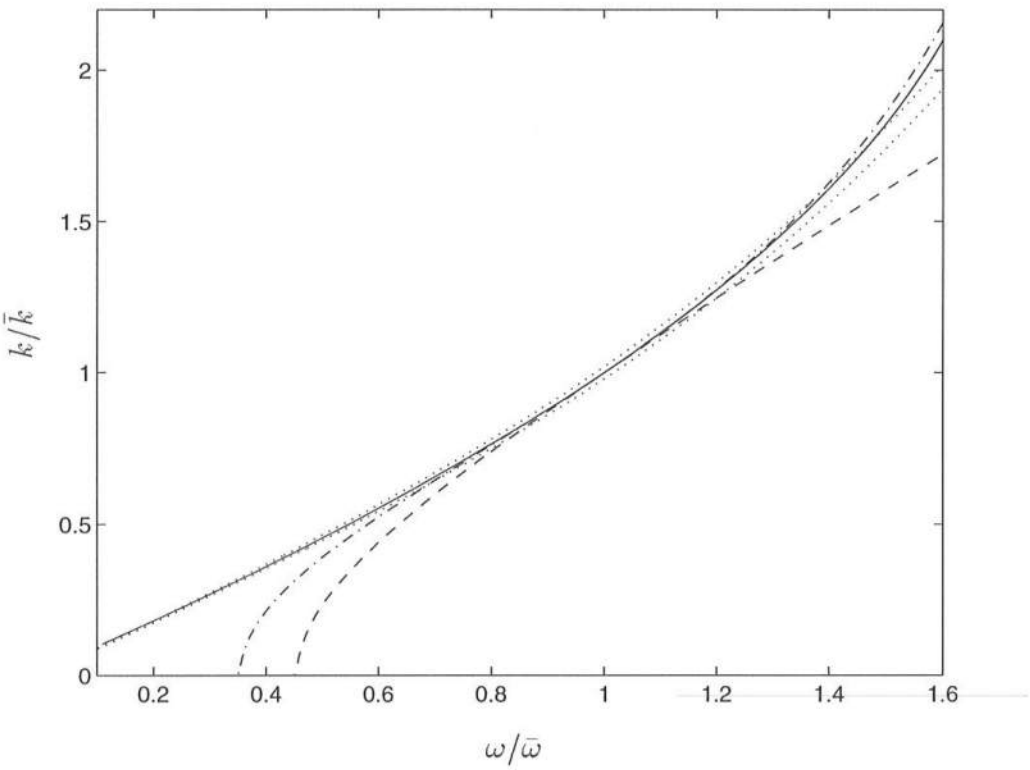

Figure 2.6: Dispersion relations for $\bar{k}h = 0.3\pi$ (dotted line: 2 percent confidence interval of exact solution, dashed line: Smith and Sprinks' model, dash-dotted line: Kubo et al.'s model, solid line: linear Schrödinger equation)

where the subscript 0 denotes the reference point. The linear shoaling coefficient for Smith and Sprinks' model can be obtained from equation (2.13) as

$$K_s = \frac{A}{A_0} = \sqrt{\frac{k_0 \bar{C}_0 \bar{C}_{g0}}{k \bar{C} \bar{C}_g}} \tag{2.23}$$

The linear shoaling coefficient for Kubo et al.'s model can be obtained from equation (2.18) as

$$K_s = \frac{A}{A_0} = \sqrt{\frac{k_0 \{(\bar{C}\bar{C}_g)_0 + (\omega - \bar{\omega}) \frac{\partial}{\partial \omega} (\bar{C}\bar{C}_g)_0\}}{k \{\bar{C}\bar{C}_g + (\omega - \bar{\omega}) \frac{\partial}{\partial \omega} (\bar{C}\bar{C}_g)\}}} \tag{2.24}$$

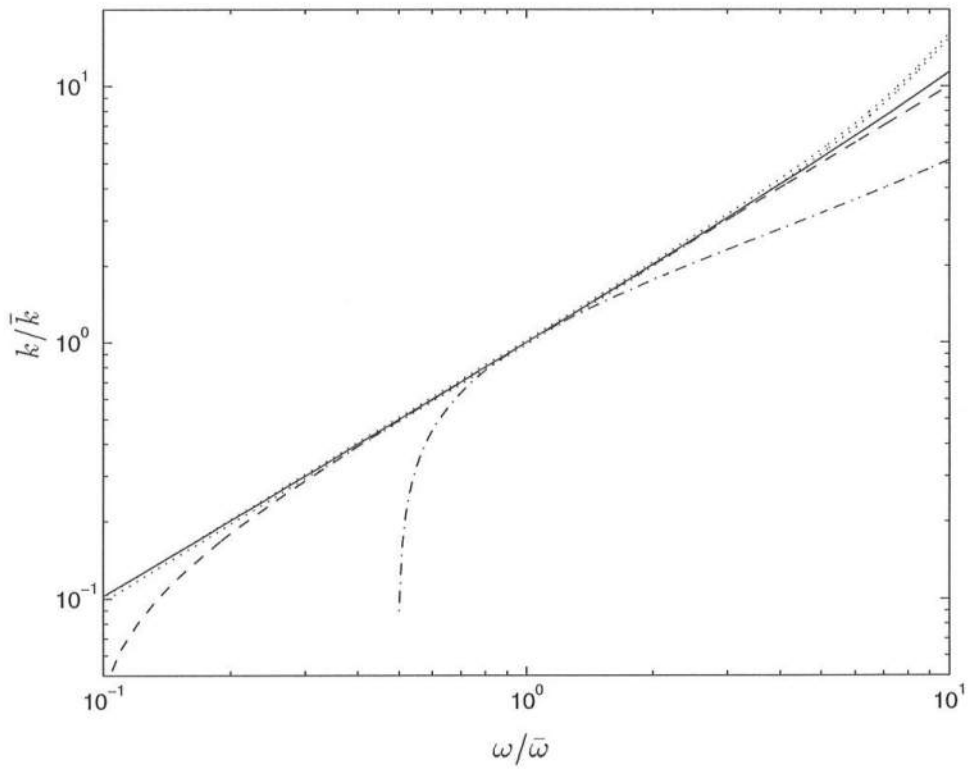

Figure 2.7: Dispersion relations for $\bar{k}h = 0.05\pi$ (dotted line: 2 percent confidence interval of exact solution, dashed line: Smith and Sprinks' model, dash-dotted line: Kubo et al.'s model, solid line: linear Schrödinger equation)

The linear shoaling coefficients for reference water depth $h_0 = 1\ m$ and frequencies from $f = 0.6\ Hz$ to $f = 1.4\ Hz$ are shown in Figure 2.8 where the shoaling coefficient decreases and then increases as water depth decreases. At lower frequencies, the turning starts deeper water, so the maximum shoaling coefficient at water depth $h = 0.01\ m$ is 2.21 at the lowest frequency. Figures 2.9 and 2.10 show the percent errors for Smith and Sprinks' model and Kubo et al.'s model, respectively, when the representative frequency is $\bar{f} = 1\ Hz$ with $\bar{k}h_0 = 1.28\pi$ at $h_0 = 1\ m$ and $\bar{k}h = 0.06\pi$ at $h = 1\ cm$. Smith and Sprinks' model gives smaller shoaling coefficients at lower frequencies and larger shoaling

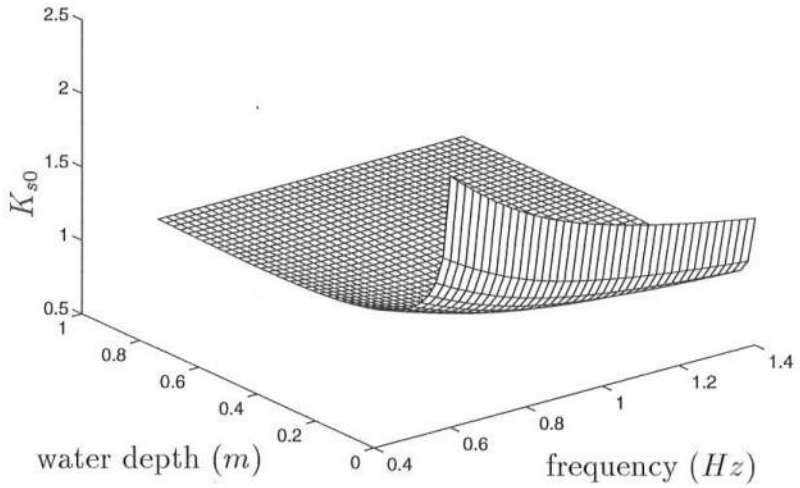

Figure 2.8: Shoaling coefficients for $h_0 = 1\ m$

coefficients at higher frequencies in all water depths relative to the exact shoaling coefficients. Kubo et al.'s model gives smaller shoaling coefficients at both lower and higher frequencies in water depth shallower than 0.4 m and gives singular solutions of the shoaling coefficients at frequencies higher than $f = 1.4\ Hz$. The singularity happens when the value of $\bar{C}\bar{C}_g + (\omega - \bar{\omega})\frac{\partial}{\partial\omega}(\bar{C}\bar{C}_g)$ becomes zero. The value of $\frac{\partial}{\partial\omega}(\bar{C}\bar{C}_g)$ is 0 in shallow water and -$\bar{\omega}/\bar{k}^2$ in deep water (see Figure 2.1), so the singularity of the shoaling coefficients happens always at higher frequencies.

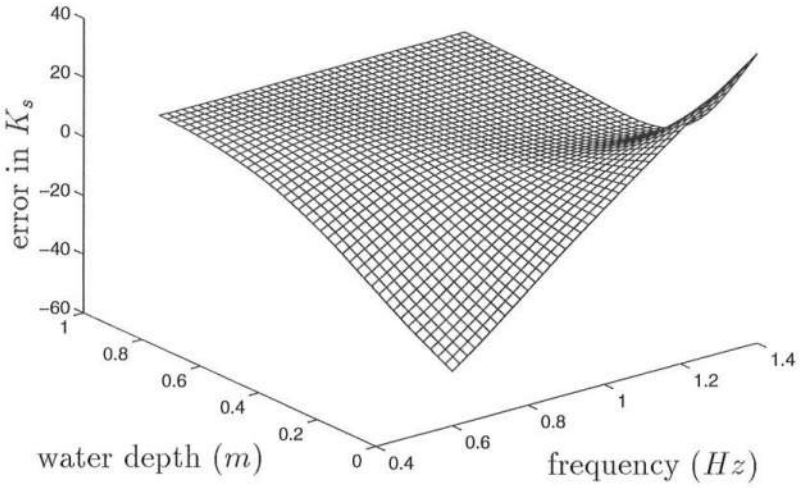

Figure 2.9: Percent errors in shoaling coefficient for Smith and Sprinks' model ($h_0 = 1\ m$, $\bar{f} = 1\ Hz$)

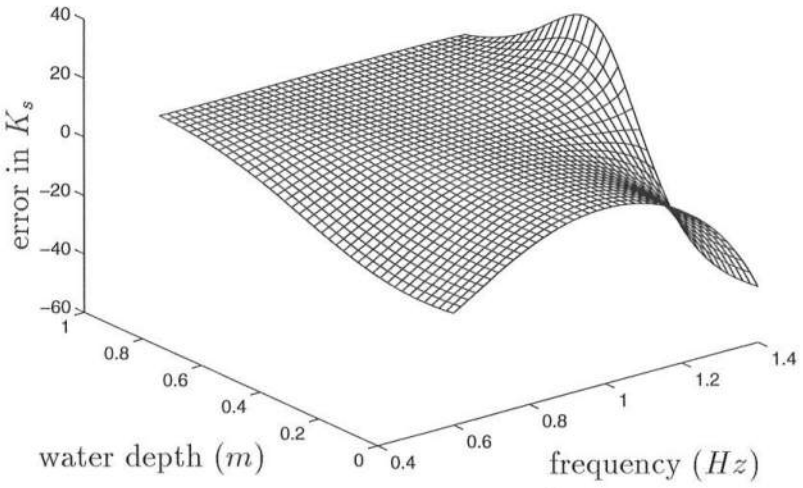

Figure 2.10: Percent errors in shoaling coefficient for Kubo et al.'s model ($h_0 = 1\ m$, $\bar{f} = 1\ Hz$)

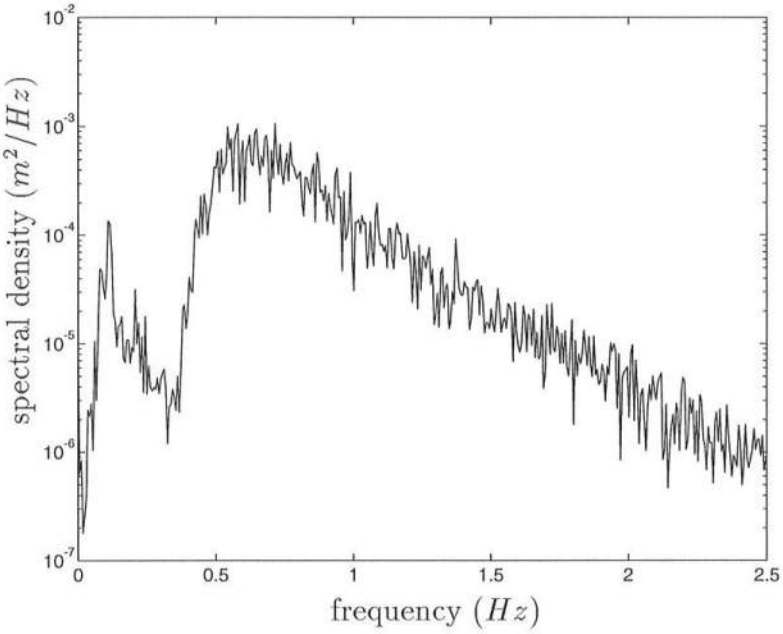

Figure 2.11: Power spectrum of water surface elevations measured at water depth of 47 cm by Mase and Kirby (1992): case 1

We test the shoaling of the two models for a case with experimental data. Mase and Kirby (1992) conducted two types of experiments measuring the water surface elevations for random waves over a plane beach. The waves were generated offshore at water depth $h_0 = 47$ cm and the waves propagated over a 1/20 sloping bottom. We use the first type of experiment which generates waves with plunging breakers. The measured power spectrum of water surface elevations at $h_0 = 47$ cm is shown in Figure 2.11. We exclude the lower and upper 2 percent spectra from the whole spectrum to get reasonable solutions, giving a frequency range of $f = 0.38$ - 1.61 Hz. We subdivide the spectrum into 2, 4, 6, or 8 components with equal frequency bandwidths. We select the representative frequencies by a weighted average or median. For a weighted average case, we get the representative frequencies by averaging the frequencies with weight of the corresponding spectral

densities.

First, we compute the squared shoaling coefficients K_{s0}^2 for linear waves which is shown in Figure 2.12. We then multiply the squared shoaling coefficients K_{s0}^2 by the power spectrum at $h_0 = 47\ cm$ to get the power spectrum over the whole range of water depths from $h = 47\ cm$ to $h = 1\ cm$. Next, we compute the squared shoaling coefficients K_s^2 from equation (2.23) (Smith and Sprinks' model) or equation (2.24) (Kubo et al.'s model). We define the percent error in the squared shoaling coefficient as $100 \times (K_s^2 - K_{s0}^2)/K_{s0}^2$. Some plots of the percent error are shown in Figure 2.13 (Smith and Sprinks' model) and Figure 2.14 (Kubo et al.'s model) for cases with 4 frequency bands using weight-averaged representative frequencies. Then, we compute the cumulative sum of the power spectra from $f = 0.38\ Hz$ to $f = 1.61\ Hz$ in each water depth using the shoaling coefficients K_{s0}^2 and K_s^2. The cumulative power spectra in each water depth using K_{s0}^2 are shown in Figure 2.15. The percent error in the cumulative sum of the power spectrum, $100 \times \sum_{n=1}^{n=m}(K_s^2 - K_{s0}^2)S(f_n)\Delta f / \sum_{n=1}^{n=N} K_{s0}^2 S(f_n)\Delta f$, is shown in Figure 2.16 (Smith and Sprinks' model) and Figure 2.17 (Kubo et al.'s model).

For Smith and Sprinks' model, the maximum 50 percent error in the squared shoaling coefficient occurs in the second frequency band and the error is always negative for frequencies lower than $\bar{f}$ and is always positive for frequencies higher than $\bar{f}$, so the percent error in cumulative sum of the power spectrum almost cancels in each frequency band. The percent error in the total energy is positive and below +1 percent in the all water depths, and the error in the total energy is higher in shallower water depth.

For Kubo et al.'s model, the maximum -10 percent error occurs in the third frequency band, and the error is negative in almost all water depths. The percent error in the cumulative sum of the power spectrum becomes larger and

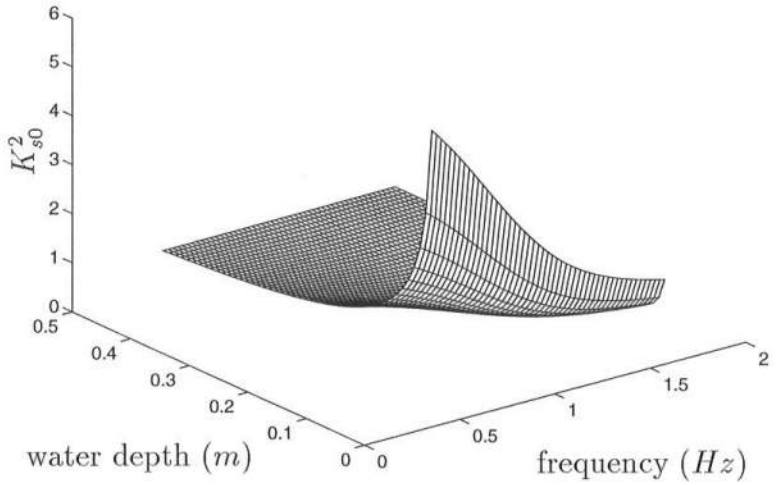

Figure 2.12: Squared shoaling coefficients K_{s0}^2 for linear wave

the percent error in the total energy is negative and above -0.7 percent in all water depths. The error in the total energy is highest in water depth of 18 cm.

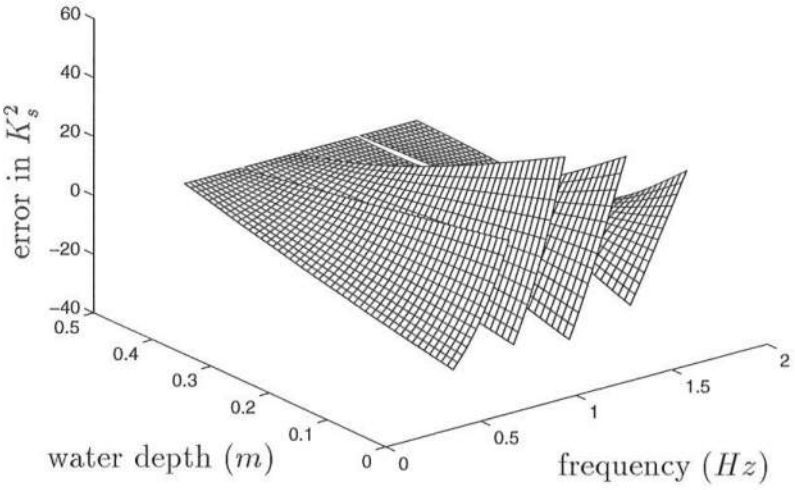

Figure 2.13: Percent errors in squared shoaling coefficients K_s^2 for Smith and Sprinks' model

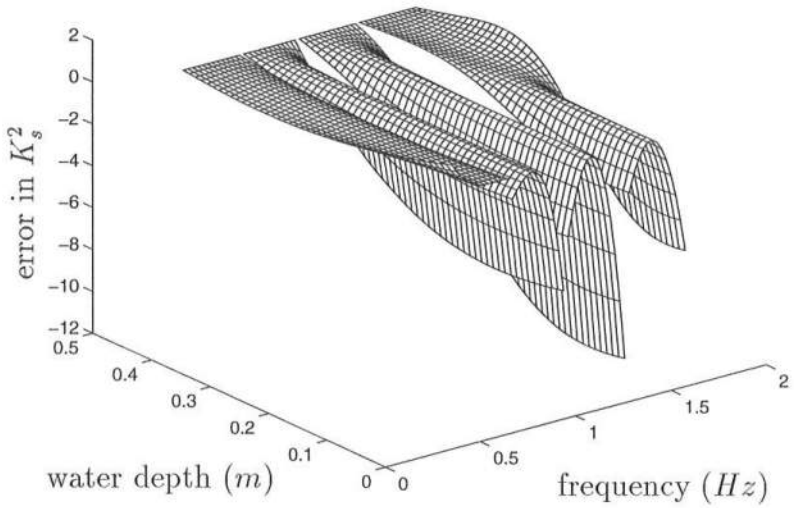

Figure 2.14: Percent errors in squared shoaling coefficients K_s^2 for Kubo et al.'s model

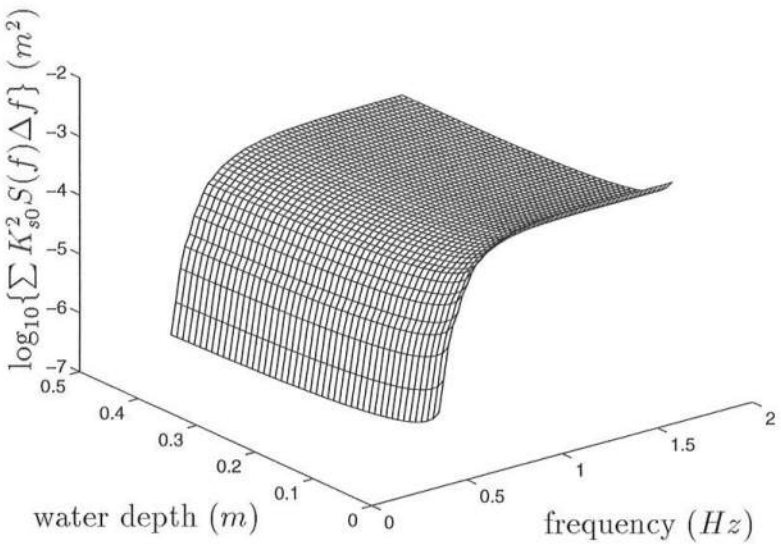

Figure 2.15: Cumulative sum of power spectra in all water depths using K_{s0}^2

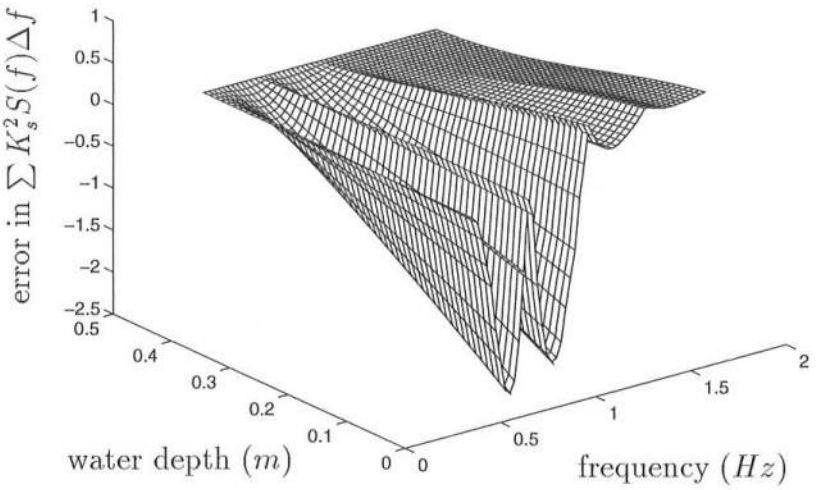

Figure 2.16: Percent errors in cumulative sum of power spectra in all water depths for Smith and Sprinks' model

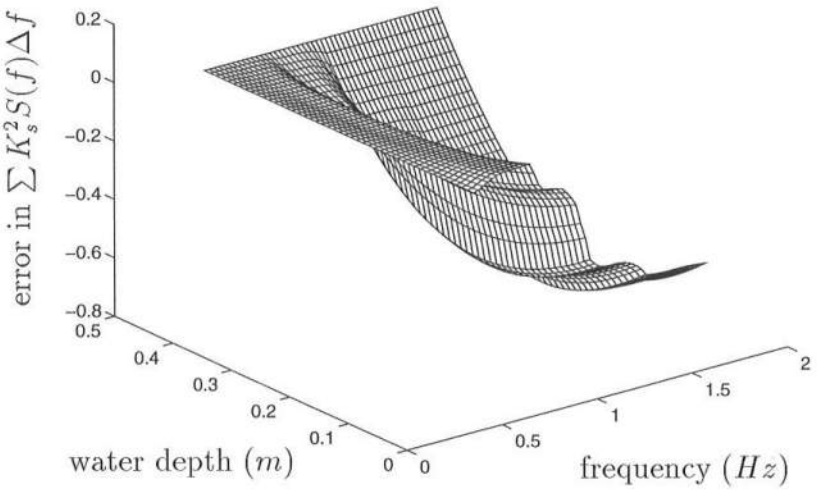

Figure 2.17: Percent errors in cumulative sum of power spectra in all water depths for Kubo et al.'s model

The percent errors in total energy $100 \times \frac{\sum (K_s^2 - K_{s0}^2) S(f) \Delta f}{\sum K_{s0}^2 S(f) \Delta f}$ in all water depths for cases with 2, 4, 6, and 8 frequency bands of equal width are shown in Figure 2.18, where the solid line represents Smith and Sprinks' model using weight-averaged frequencies, the dashed line represents Smith and Sprinks' model using centered frequencies, the dash-dotted line represents Kubo et al.'s model using weight-averaged frequencies, and the dotted line represents Kubo et al.'s model using centered frequencies. From Figure 2.18 we can find that the choice of the representative frequencies for Kubo et al.'s model does not make a considerable difference in errors in total energy, while the choice of the representative frequencies for Smith and Sprinks' model does make a significant difference. If the frequency bandwidth is large, for example the case with 2 bands, Kubo et al.'s model yields more error in total energy than Smith and Sprinks' model. But, as the frequency bandwidth becomes smaller, Kubo et al.'s model yields less error in total energy than Smith and Sprinks' model. The difference in errors between Smith and Sprinks' model and Kubo et al.'s model becomes larger and then smaller as the bandwidth becomes smaller.

We compare the two models in terms of wave kinematics. For irregular waves, the particle velocity in x direction can be described as

$$u = \sum_n \frac{a_n g k_n}{\omega_n} \frac{\cosh k_n(z+h)}{\cosh k_n h} e^{i(k_n x - \omega_n t)} \tag{2.25}$$

where n represents each frequency component. When the time-dependent mild-slope equation is used in obtaining the particle velocity in x direction, we get the following equation

$$u = \sum_n \frac{a_n g k_n}{\omega_n} \frac{\cosh \bar{k}_n(z+h)}{\cosh \bar{k}_n h} e^{i(k_n x - \omega_n t)} \tag{2.26}$$

where the representative wavenumber $\bar{k}_n$ is used in considering the depth effects as $\frac{\cosh \bar{k}_n(z+h)}{\cosh \bar{k}_n h}$. Also, the wavenumber k_n in equation (2.26) is obtained from the model

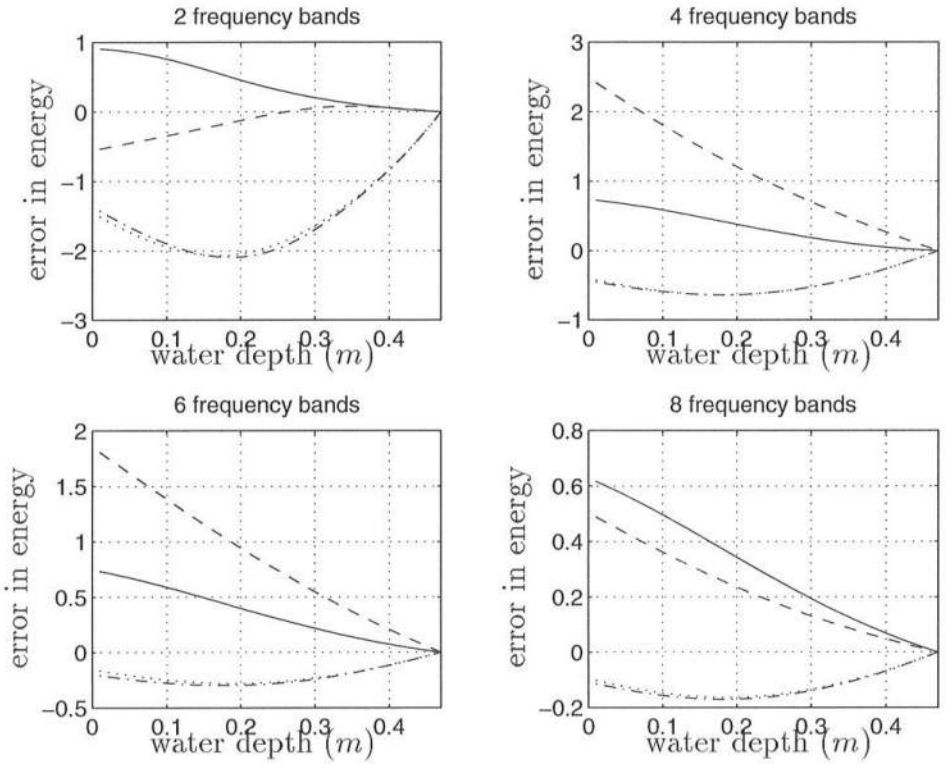

Figure 2.18: Percent errors in total energy in all water depths when frequency bandwidth is equal (solid line: Smith and Sprinks' model using weight-averaged frequencies, dashed line: Smith and Sprinks' model using centered frequencies, dash-dotted line: Kubo et al.'s model using weight-averaged frequencies, dotted line: Kubo et al.'s model using centered frequencies)

dispersion relations (2.14) and (2.19), and so is different from the wavenumber k_n in equation (2.25). Therefore, there are differences between the particle velocities u between equation (2.25) and (2.26).

We compare the particle velocities in terms of the variance of the particle velocities. The squared the particle velocity $|u|^2$ can be be obtained by multiplying u by the conjugate of u. The average of squared the particle velocity $\overline{|u|^2}$, which

is variance of u or energy of u, can be obtained as

$$\overline{|u|^2} = \sum_n \{\frac{a_n g k_n}{\omega_n} \frac{\cosh k_n(z+h)}{\cosh k_n h}\}^2 \tag{2.27}$$

from equation (2.25). When the time-dependent mild-slope equation is used, the variance of u can be obtained as

$$\overline{|u|^2} = \sum_n \{\frac{a_n g k_n}{\omega_n} \frac{\cosh \bar{k}_n(z+h)}{\cosh \bar{k}_n h}\}^2 \tag{2.28}$$

We can get the amplitude of water surface elevation from power spectrum as

$$a_n = \sqrt{2K_s^2 S(f_n)\Delta f} \tag{2.29}$$

We test the difference of the variance of the particle velocities for the case of experiments done by Mase and Kirby (1992). We use the first type of experiment which generates waves with plunging breakers. The measured power spectrum of water surface elevations at $h_0 = 47\ cm$ is shown in Figure 2.11. We exclude the lower and upper 2 percent spectra from the whole spectrum, so the frequency range is $f = 0.38 - 1.61\ Hz$. We subdivide the concerning spectrum into 2, 4, 6, or 8 components with equal frequency bandwidth. We select the representative frequencies by a weighted average or median.

First, the wave kinematics at the free surface $z = 0$ is analyzed. We compute the amplitude of the particle velocities from equations (2.25) and (2.26) and compute the percent error. Figure 2.19 shows the squared amplitude of the particle velocities. Figures 2.20 and 2.21 show the percent errors in the squared amplitude of the particle velocities for Smith and Sprinks' model and Kubo et al.'s model. Figure 2.22 shows the percent errors in the variance of particle velocities over the whole range of water depths for 2, 4, 6, or 8 frequency bands with equal bandwidth.

As the bandwidth becomes smaller, the percent errors in variance of particle velocities become smaller. Smith and Sprinks' model yields smaller errors when using weight-averaged frequencies than when using centered frequencies except with 8 frequency bands. The choice of representative frequencies does not make a sufficient difference. Roughly, Kubo et al.'s model yields smaller errors than Smith and Sprinks' model. When Smith and Sprinks' model uses 4 frequency bands and weight-averaged frequencies, the maximum error in variance of u is -2 percent. When Kubo et al.'s model uses 4 frequency bands and weight-averaged frequencies, the maximum error in variance of u is -1.8 percent.

Smith and Sprinks' model yields negative errors in deeper water and positive errors in shallower water. In deeper water, the error in the shoaling coefficient is almost zero, and the error in wavenumber is negative, so the error in variance of u is negative. In shallower water the error in the shoaling coefficient is positive, and the error in wavenumber is almost zero, so the error in variance of u is positive. On the contrary, Kubo et al.'s model yields positive errors in deeper water and negative errors in shallower water. In deeper water, the error in shoaling coefficient is almost zero, and the error in wavenumber is positive, so the error in variance of u is positive. In shallower water, the error in shoaling coefficient is negative, and the error in wavenumber is negative, so the error in variance of u is negative.

Second, we analyze the wave kinematics at the bottom $z = -h$. The percent errors in the variance of particle velocities at $z = -h$ in all water depths are shown in Figure 2.23. As the particle velocities are analyzed from water surface $z = 0$ to bottom $z = -h$, the vertical effect $\cosh \bar{k}(z + h)/\cosh \bar{k}h$ is considered. So the errors in variance of u at the bottom are different from those at the water surface.

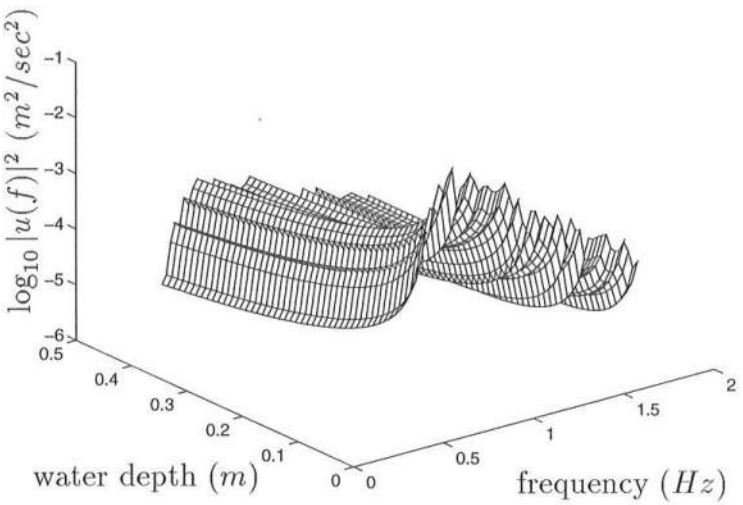

Figure 2.19: Squared particle velocities at $z = 0$

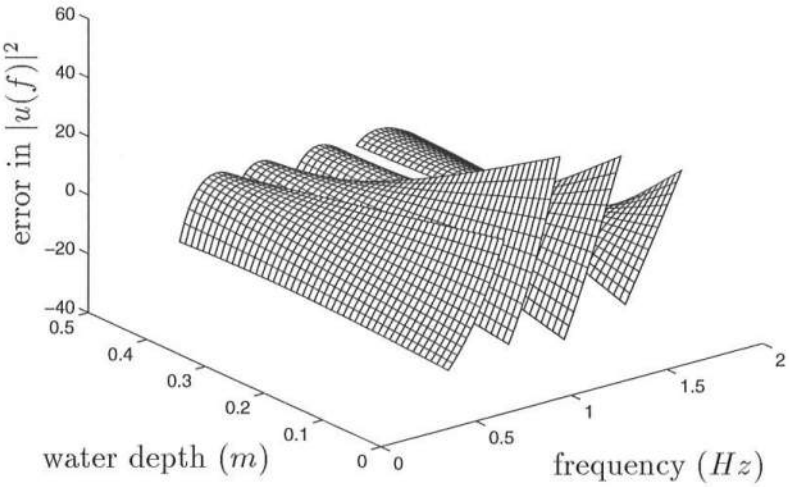

Figure 2.20: Percent errors in squared particle velocities at $z = 0$ (Smith and Sprinks' model with 4 frequency bands using weight-averaged frequencies)

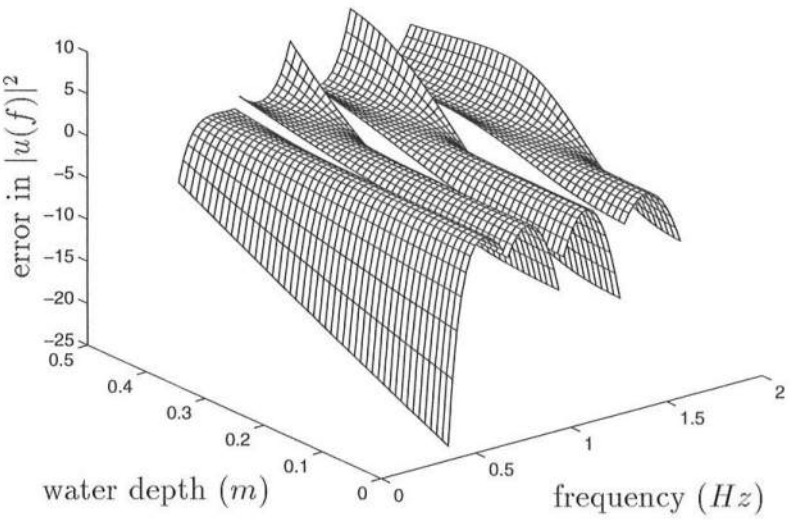

Figure 2.21: Percent errors in squared particle velocities at $z = 0$ (Kubo et al.'s model with 4 frequency bands using weight-averaged frequencies)

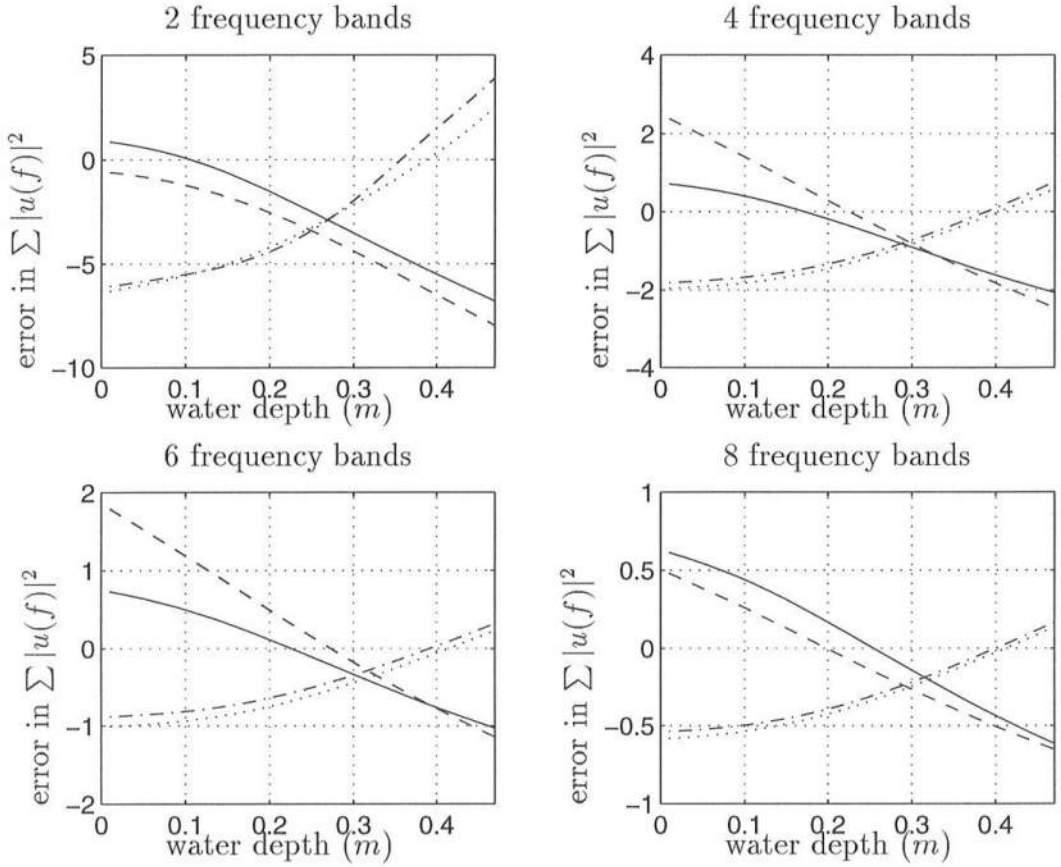

Figure 2.22: Percent errors in variance of particle velocities at $z = 0$ when frequency bandwidth is equal (solid line: Smith and Sprinks' model using weight-averaged frequencies, dashed line: Smith and Sprinks' model using centered frequencies, dash-dotted line: Kubo et al.'s model using weight-averaged frequencies, dotted line: Kubo et al.'s model using centered frequencies)

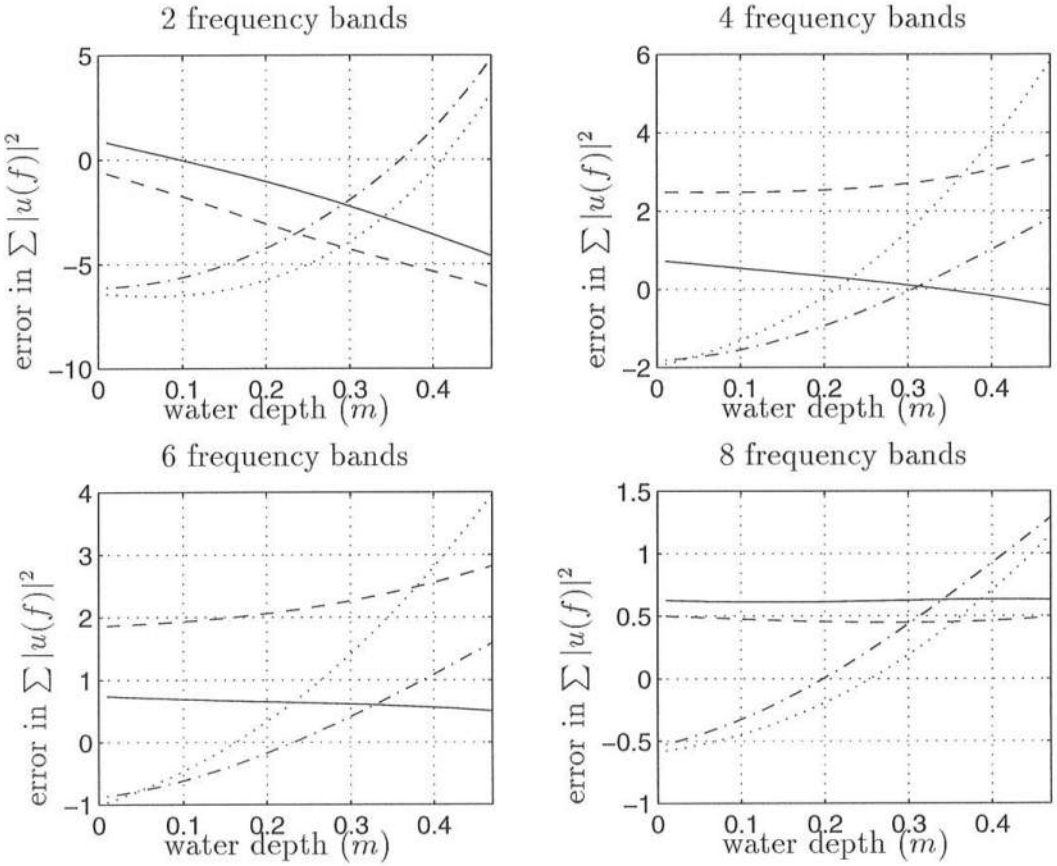

Figure 2.23: Percent errors in variance of particle velocities at $z = -h$ when frequency bandwidth is equal (solid line: Smith and Sprinks' model using weight-averaged frequencies, dashed line: Smith and Sprinks' model using centered frequencies, dash-dotted line: Kubo et al.'s model using weight-averaged frequencies, dotted line: Kubo et al.'s model using centered frequencies)

For constant water depth, the two models can be compared against the Schrödinger equation, which is an equation for modulation of wave amplitudes accurate to $O(\Delta k)^2$ and serves a benchmark for other leading order envelope equations. We analyze the problems in one dimension horizontally, *i.e.*, x direction which is assumed to be the direction perpendicular to the wave crest. The velocity potential $\tilde{\phi}$ in Smith and Sprinks' equation (2.3) can be defined as

$$\tilde{\phi}(x,t) = Ae^{i(\int k dx - \omega t)} = \bar{A}(x,t)e^{i(\int \bar{k} dx - \bar{\omega} t)} \tag{2.30}$$

where $\bar{A}(x,t)$, which modulates in space and time, is the amplitude obtained by extracting the harmonic terms with carrier wavenumber $\bar{k}$ and frequency $\bar{\omega}$ from the velocity potential $\tilde{\phi}$. We have the following relations for the amplitude $\bar{A}$:

$$\bar{A} = Ae^{i(\int (k-\bar{k})dx - (\omega - \bar{\omega})t)} \tag{2.31}$$

$$\frac{\partial \bar{A}}{\partial t} = -i(\omega - \bar{\omega})\bar{A} \tag{2.32}$$

$$\frac{\partial \bar{A}}{\partial x} = i(k - \bar{k})\bar{A} \tag{2.33}$$

$$\frac{\partial^2 \bar{A}}{\partial x^2} = -(k - \bar{k})^2 \bar{A} \tag{2.34}$$

The local angular frequency $\omega(k)$ can be approximated by a few terms in the Taylor series expansion to $O(\Delta k)^2$:

$$\omega = \bar{\omega} + \bar{\omega}'(k - \bar{k}) + \bar{\omega}'' \frac{(k - \bar{k})^2}{2} \tag{2.35}$$

where the superscript prime means the derivative with respect to the wavenumber. After multiplying equation (2.35) by $\bar{A}$ and rearranging, we have

$$(\omega - \bar{\omega})\bar{A} = \bar{C}_g(k - \bar{k})\bar{A} + \bar{\omega}'' \frac{(k - \bar{k})^2}{2}\bar{A} \tag{2.36}$$

where $\bar{\omega}'$ is replaced by the group velocity $\bar{C}_g$. Then, the linear Schrödinger equation for modulation of wave amplitudes $\bar{A}$ can be obtained using the relations (2.31) – (2.34):

$$\frac{\partial \bar{A}}{\partial t} + \bar{C}_g \frac{\partial \bar{A}}{\partial x} - \frac{i}{2}\bar{\omega}'' \frac{\partial^2 \bar{A}}{\partial x^2} = 0 \tag{2.37}$$

This equation and the dispersion relation (2.35) will be used as a reference in comparing the range of validity of the two mild-slope equations. Substitution of equation (2.30) into Smith and Sprinks' equation (2.3) gives the equation for modulation of wave amplitudes $\bar{A}$:

$$-2i\bar{\omega}(\frac{\partial \bar{A}}{\partial t}+\bar{C}_g\frac{\partial \bar{A}}{\partial x})+\frac{\partial^2 \bar{A}}{\partial t^2}-\bar{C}\bar{C}_g\frac{\partial^2 \bar{A}}{\partial x^2}=0 \tag{2.38}$$

or

$$\frac{\partial \bar{A}}{\partial t}+\bar{C}_g\frac{\partial \bar{A}}{\partial x}-\frac{i}{2}\frac{\bar{C}_g}{\bar{\omega}}(\bar{C}-\bar{C}_g)\frac{\partial^2 \bar{A}}{\partial x^2}=0 \tag{2.39}$$

where we use the following relation accurate to $O(\Delta k)$:

$$\frac{\partial \bar{A}}{\partial t}+\bar{C}_g\frac{\partial \bar{A}}{\partial x}=0 \tag{2.40}$$

The velocity potential $\hat{\phi}$ in Kubo et al.'s equation (2.7) can be defined as

$$\hat{\phi}(x,t)=\tilde{\phi}(x,t)e^{i\bar{\omega}t}=Ae^{i(\int kdx-(\omega-\bar{\omega})t)}=\bar{A}(x,t)e^{i\int \bar{k}dx} \tag{2.41}$$

Substitution of equation (2.41) into Kubo et al.'s equation (2.7) gives the equation for modulation of wave amplitudes $\bar{A}$:

$$2i\bar{\omega}(\frac{\partial \bar{A}}{\partial t}+\bar{C}_g\frac{\partial \bar{A}}{\partial x})+\bar{C}\bar{C}_g\frac{\partial^2 \bar{A}}{\partial x^2}+i\frac{\partial}{\partial \omega}(\bar{C}\bar{C}_g)(\frac{\partial^3 \bar{A}}{\partial x^2\partial t}+2i\bar{k}\frac{\partial^2 \bar{A}}{\partial x\partial t})=0 \tag{2.42}$$

or

$$\frac{\partial \bar{A}}{\partial t}+\bar{C}_g\frac{\partial \bar{A}}{\partial x}-i\{\bar{\omega}''+\frac{\bar{C}_g}{2\bar{\omega}}(2\bar{C}_g-\bar{C})\}\frac{\partial^2 \bar{A}}{\partial x^2}=0 \tag{2.43}$$

where we use the relation (2.40) and neglect the term smaller than $O(\Delta k)^2$.

Figure 2.24 shows the coefficients of $\frac{\partial^2 \bar{A}}{\partial x^2}$ multiplied by $\bar{k}^2/\bar{\omega}$ in equations (2.37), (2.39), and (2.43). Smith and Sprinks' model satisfies the Schrödinger equation in very shallow water ($\bar{k}h \simeq 0$), and the error becomes larger at intermediate-depth water with largest error at $\bar{k}h \simeq 0.7\pi$ after which the error becomes smaller in deep water and becomes constant in very deep water. Kubo et al.'s model

satisfies the Schrödinger equation at a point of intermediate depth ($\bar{k}h \simeq 0.3\pi$) and, from the point, the error increases in both deeper water and shallower water with a positive error in deeper water and a negative error in shallower water. The maximum error occurs in very shallow water for Kubo et al.'s model. The coefficient of $\frac{\partial^2 \bar{A}}{\partial x^2}$ for Smith and Sprinks' model is closer to the coefficient for the linear Schrödinger equation at $\bar{k}h \leq 0.2\pi$ than for Kubo et al.'s model. The coefficient of $\frac{\partial^2 \bar{A}}{\partial x^2}$ for Kubo et al.'s model is closer to the coefficient for the linear Schrödinger equation at $\bar{k}h > 0.2\pi$ than for Smith and Sprinks' model.

Figure 2.25 shows the percent errors in $k/\bar{k}$ for the linear Schrödinger equation, which can be compared with Figure 2.3 for Smith and Sprinks' model and Figure 2.4 for Kubo et al.'s model. These figures show that the percent errors in $k/\bar{k}$ for the linear Schrödinger equation are much smaller than those for Smith and Sprinks' model (2.3) and Kubo et al.'s model (2.7). The dispersion relations for the linear Schrödinger equation for deep water ($\bar{k}h = 2\pi$), intermediate-depth water ($\bar{k}h = 0.3\pi$), and shallow water ($\bar{k}h = 0.05\pi$) are shown in Figures 2.5 - 2.7 by the solid line.

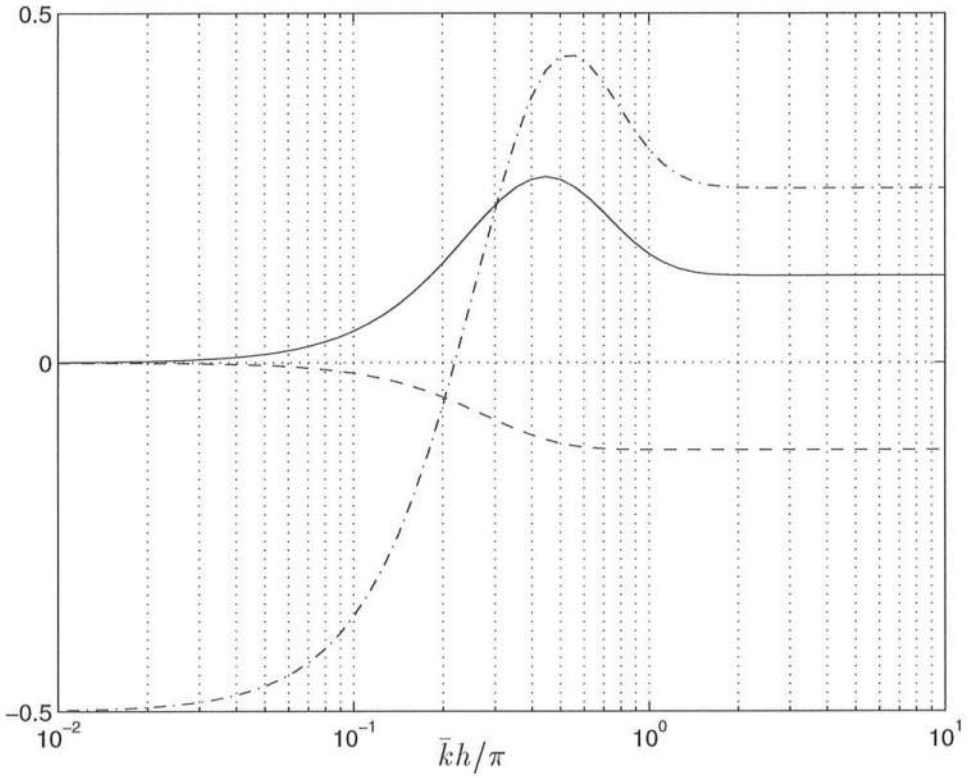

Figure 2.24: $-\frac{\bar{k}^2}{\bar{\omega}}\frac{\bar{\omega}''}{2}$: solid line, $-\frac{\bar{k}^2}{\bar{\omega}}\frac{\bar{C}_g}{2\bar{\omega}}(\bar{C}-\bar{C}_g)$: dashed line, $-\frac{\bar{k}^2}{\bar{\omega}}\{\bar{\omega}''+\frac{\bar{C}_g}{2\bar{\omega}}(2\bar{C}_g-\bar{C})\}$: dash-dotted line

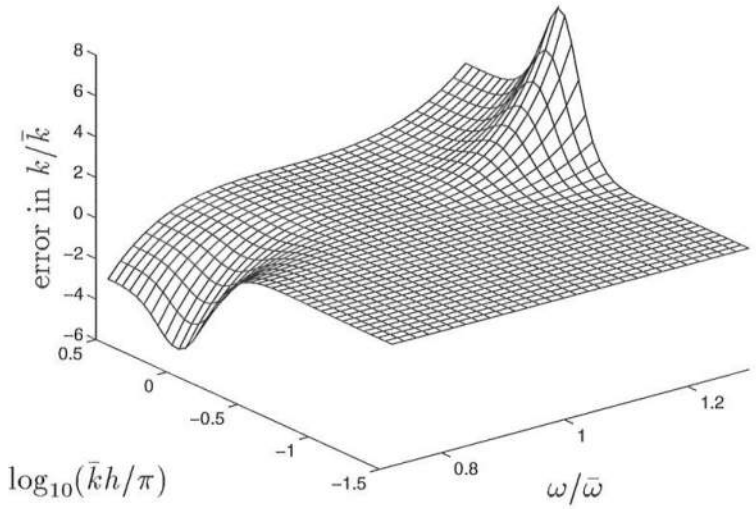

Figure 2.25: Percent errors in $k/\bar{k}$ for linear Schrödinger equation

2.2 Comparisons of Model Equations for Bichromatic Waves

We compare the two models analytically and numerically for wave trains with slightly different wavelengths $k_+ = \bar{k} + \Delta k$ and $k_- = \bar{k} - \Delta k$ with $\Delta k/\bar{k} \ll 1$ (Mei, 1989):

$$\tilde{\phi} = A_0\{e^{i(k_+ x - \omega_+ t)} + e^{i(k_- x - \omega_- t)}\} \tag{2.44}$$

where $k_\pm$ satisfies the following dispersion relation

$$\omega_\pm^2 = g k_\pm \tanh k_\pm h \tag{2.45}$$

Approximating $\omega_\pm$ to $O(\Delta k)^2$, we have

$$\omega_\pm = [\bar{\omega} \pm \bar{\omega}'\Delta k + \bar{\omega}''\frac{(\Delta k)^2}{2} \pm \cdots]_k \tag{2.46}$$

so that we have the velocity potential

$$\tilde{\phi} = 2A_0 \cos\{\Delta k(x - \bar{\omega}'t)\} e^{i\{\bar{k}x - (\bar{\omega} + \bar{\omega}''\frac{(\Delta k)^2}{2})t\}} + O(\Delta k)^3 \tag{2.47}$$

Over the space and time scale $O(\Delta k)^{-1}$, the envelope modulates and moves at $\bar{\omega}'$; however, over the time scale $O(\Delta k)^{-2}$, the phase, in particular the frequency, changes. This example suggests that there is a cascade of time scales $O(1), O(\Delta k)^{-1}, O(\Delta k)^{-2}, \cdots$, and so on. Substitution of equation (2.47) into Smith and Sprinks' equation (2.3) yields

$$2A_0(\Delta k)^2\{\bar{\omega}'(\frac{\bar{\omega}}{\bar{k}} - \bar{\omega}') - \bar{\omega}\bar{\omega}''\} \cos\{\Delta k(x - \bar{\omega}'t)\} e^{i\{\bar{k}x - (\bar{\omega} + \bar{\omega}''\frac{(\Delta k)^2}{2})t\}} + O(\Delta k)^3 = 0 \tag{2.48}$$

which becomes zero in very shallow water and non-zero otherwise. The term $\bar{\omega}'(\frac{\bar{\omega}}{\bar{k}} - \bar{\omega}') - \bar{\omega}\bar{\omega}''$ in equation (2.48) can be seen in the difference of the coefficients of $\frac{\partial^2 \bar{A}}{\partial x^2}$ between equations (2.37) and (2.39).

For the present case, the velocity potential $\hat{\phi}$ in Kubo et al.'s equation (2.7) can be written as

$$\hat{\phi} = \tilde{\phi} e^{i\bar{\omega}t} = 2A_0 \cos\{\Delta k(x - \bar{\omega}'t)\} e^{i\{\bar{k}x - \bar{\omega}''\frac{(\Delta k)^2}{2}t\}} + O(\Delta k)^3 \tag{2.49}$$

Substitution of equation (2.49) into Kubo et al.'s equation (2.7) yields

$$2A_0(\Delta k)^2\{\bar{\omega}'(\frac{\bar{\omega}}{\bar{k}}-2\bar{\omega}')-\bar{\omega}\bar{\omega}''\}\cos\{\Delta k(x-\bar{\omega}'t)\}e^{i\{\bar{k}x-\bar{\omega}''\frac{(\Delta k)^2}{2}t\}}+O(\Delta k)^3=0 \quad (2.50)$$

which becomes zero at $\bar{k}h \simeq 0.3\pi$ and non-zero otherwise. The term $\bar{\omega}'(\frac{\bar{\omega}}{\bar{k}}-2\bar{\omega}')-\bar{\omega}\bar{\omega}''$ can be seen in the difference of the coefficients of $\frac{\partial^2\bar{A}}{\partial x^2}$ between equations (2.37) and (2.43).

We test the two models numerically. The difference of wavenumber is specified as $\Delta k/\bar{k}$=0.15. We use Radder and Dingemans' equations (2.5) and (2.6) instead of Smith and Sprinks' equation (2.3).

In order to dissipate wave energy at downwave boundaries, we presently use a wave damping layer at the downwave boundary. For Radder and Dingemans' equation, the linear dynamic free surface boundary condition (2.6) is modified to (Kirby et al., 1992)

$$\frac{\partial\tilde{\phi}}{\partial t}=-g\eta-D_s\tilde{\phi}=G(\tilde{\phi},\eta) \quad (2.51)$$

where

$$D_s = \begin{cases} 0, & x<x_{sponge} \\ \bar{\omega}\frac{e^{F^n}-1}{e-1}, & x\geq x_{sponge} \end{cases} \quad (2.52)$$

$$F = \frac{x-x_{sponge}}{x_{max}-x_{sponge}}, \quad (2.53)$$

the sponge length x_{sponge} is specified as 2.5 times the wave length at the sponge layer. Equation (2.51) can be combined with equation (2.5) to yield a modification of Smith and Sprinks' equation:

$$\frac{\partial^2\tilde{\phi}}{\partial t^2}+D_s\frac{\partial\tilde{\phi}}{\partial t}-\nabla\cdot(\bar{C}\bar{C}_g\nabla\tilde{\phi})+(\bar{\omega}^2-\bar{k}^2\bar{C}\bar{C}_g)\tilde{\phi}=0 \quad (2.54)$$

by using the following relation

$$\frac{\partial\eta}{\partial t}=-\frac{1}{g}(\frac{\partial^2\tilde{\phi}}{\partial t^2}+D_s\frac{\partial\tilde{\phi}}{\partial t}) \quad (2.55)$$

For monochromatic waves with the velocity potential $\tilde{\phi} = \hat{\phi}e^{-i\omega t}$, we obtain the following equation:

$$\nabla \cdot (CC_g \nabla \hat{\phi}) + (k^2 CC_g + i\omega D_s)\hat{\phi} = 0 \tag{2.56}$$

or

$$\nabla \cdot (CC_g \nabla \hat{\phi}) + k^2 CC_g (1 + i\frac{D_s}{\omega n})\hat{\phi} = 0 \tag{2.57}$$

Kubo et al.'s equation (2.7) can include the damping terms as

$$\begin{aligned} &\nabla \cdot (\bar{C}\bar{C}_g \nabla \hat{\phi}) + \bar{k}^2 \bar{C}\bar{C}_g (1 + if_{D_s})\hat{\phi} \\ &+i\nabla \cdot (\frac{\partial}{\partial \omega}(\bar{C}\bar{C}_g)\nabla \frac{\partial \hat{\phi}}{\partial t}) + i\frac{\partial}{\partial \omega}(\bar{k}^2 \bar{C}\bar{C}_g)(1 + if_{D_s})\frac{\partial \hat{\phi}}{\partial t} = 0 \end{aligned} \tag{2.58}$$

where

$$f_{D_s} = \frac{D_s}{\bar{\omega}\bar{n}} \tag{2.59}$$

Equation (2.58) with f_{D_s} in equation (2.59) can be compared to the model for breaking waves (1.25) with the energy dissipation coefficient f_{D_b} in equation (1.24).

A fourth order Adams-Bashforth-Moulton predictor-corrector method is used to discretize modified Radder and Dingemans' equations (2.5) and (2.51) in time. In order to discretize terms with spatial differentiation, we use the fourth order discretization:

$$\left[\frac{\partial f}{\partial x}\right]_i = \begin{cases} \frac{1}{12\Delta x}(-3f_{i-1} - 10f_i + 18f_{i+1} - 6f_{i+2} + f_{i+3}), & i\text{=}2 \\ \frac{1}{12\Delta x}(f_{i-2} - 8f_{i-1} + 8f_{i+1} - f_{i+2}), & i\text{=}3,4,\cdots,\text{I-3,I-2} \\ \frac{1}{12\Delta x}(-3f_{i+1} - 10f_i + 18f_{i-1} - 6f_{i-2} + f_{i-3}), & i\text{=I-1} \end{cases}$$

$$\left[\frac{\partial^2 f}{\partial x^2}\right]_i = \begin{cases} \frac{1}{12(\Delta x)^2}(11f_{i-1} - 20f_i + 6f_{i+1} + 4f_{i+2} - f_{i+3}), & i\text{=}2 \\ \frac{1}{12(\Delta x)^2}(-f_{i-2} + 16f_{i-1} - 30f_i + 16f_{i+1} - f_{i+2}), & i\text{=}3,4,\cdots,\text{I-3,I-2} \\ \frac{1}{12(\Delta x)^2}(11f_{i+1} - 20f_i + 6f_{i-1} + 4f_{i-2} - f_{i-3}), & i\text{=I-1} \end{cases} \tag{2.60}$$

In the Adams-Bashforth predictor step, we have

$$\begin{aligned}\eta^{n+1} &= \eta^n + \frac{\Delta t}{24}\{55F^n - 59F^{n-1} + 37F^{n-2} - 9F^{n-3}\} \\ \tilde{\phi}^{n+1} &= \tilde{\phi}^n + \frac{\Delta t}{24}\{55G^n - 59G^{n-1} + 37G^{n-2} - 9G^{n-3}\}\end{aligned} \tag{2.61}$$

and in the Adams-Moulton corrector step, we have

$$\begin{aligned}\eta^{n+1} &= \eta^n + \frac{\Delta t}{24}\{9F^{n+1} + 19F^n - 5F^{n-1} + F^{n-2}\} \\ \tilde{\phi}^{n+1} &= \tilde{\phi}^n + \frac{\Delta t}{24}\{9G^{n+1} + 19G^n - 5G^{n-1} + G^{n-2}\}\end{aligned} \tag{2.62}$$

where the superscript n denotes the time step. If the errors between predicted and corrected values are small enough, we proceed to the next time step; otherwise, we repeat correcting until we get small errors. The wavemaker boundary condition for the modified Radder and Dingemans' model is specified as

$$\tilde{\phi}_2 - \tilde{\phi}_1 = u\Delta x \tag{2.63}$$

where $u(t)$ is particle velocity in x direction which needs to be specified. At the downwave boundary a reflective boundary condition is used:

$$\begin{aligned}\tilde{\phi}_I - \tilde{\phi}_{I-1} &= 0 \\ \eta_I - \eta_{I-1} &= 0\end{aligned} \tag{2.64}$$

A modified Kubo et al.'s equation (2.58) is discretized in time by means of the Crank-Nicolson method which is second order in $O(\Delta t)^2$. The Crank-Nicolson method is implicit, so is not restricted by the stability criteria. In order to discretize terms with spatial differentiation, we use the second order discretization:

$$\left[\frac{\partial f}{\partial x}\right]_i = \frac{1}{2\Delta x}(f_{i+1} - f_{i-1}), \quad i = 2, 3, \cdots, \text{I-2,I-1}$$

$$\left[\frac{\partial^2 f}{\partial x^2}\right]_i = \frac{1}{(\Delta x)^2}(f_{i+1} - 2f_i + f_{i-1}), \quad i = 2, 3, \cdots, \text{I-2,I-1} \tag{2.65}$$

In order to discretize terms with time differentiation we use the second order discretization:

$$\begin{aligned}
&\frac{1}{2}\Big([\frac{\partial}{\partial x}\{(\bar{C}\bar{C}_g)\frac{\partial\hat{\phi}}{\partial x}\}+\bar{k}^2\bar{C}\bar{C}_g(1+if_{D_s})\hat{\phi}]^n \\
&+[\frac{\partial}{\partial x}\{(\bar{C}\bar{C}_g)\frac{\partial\hat{\phi}}{\partial x}\}+\bar{k}^2\bar{C}\bar{C}_g(1+if_{D_s})\hat{\phi}]^{n+1}\Big) \\
+\frac{i}{\Delta t}\Big([\frac{\partial}{\partial x}\{\frac{\partial}{\partial\omega}(\bar{C}\bar{C}_g)\frac{\partial\hat{\phi}}{\partial x}\}+\frac{\partial}{\partial\omega}(\bar{C}\bar{C}_g)(1+if_{D_s})\hat{\phi}]^{n+1}- \\
[\frac{\partial}{\partial x}\{\frac{\partial}{\partial\omega}(\bar{C}\bar{C}_g)\frac{\partial\hat{\phi}}{\partial x}\}+\frac{\partial}{\partial\omega}(\bar{C}\bar{C}_g)(1+if_{D_s})\hat{\phi}]^{n}\Big)=0
\end{aligned} \tag{2.66}$$

which gives a tridiagonal matrix with unknowns $\hat{\phi}_{i-1}^{n+1}$, $\hat{\phi}_i^{n+1}$ and $\hat{\phi}_{i+1}^{n+1}$. The unknowns, $\hat{\phi}^{n+1}$, are solved by the Thomas algorithm (Thomas, 1949). The wavemaker boundary condition for the modified Kubo et al.'s model is specified as

$$\hat{\phi}_2-\hat{\phi}_1=ue^{i\bar{\omega}t}\Delta x \tag{2.67}$$

where $u(t)$ is particle velocity in x direction which needs to be specified. At the downwave boundary a reflective boundary condition is used:

$$\hat{\phi}_I-\hat{\phi}_{I-1}=0 \tag{2.68}$$

First, we test the two models for deep water ($\bar{k}h=2\pi$). The water depth is 1 m, the wave height is 0.15 m, the carrier wave period (T) is 0.80046 s, the carrier wavelength (L) is 1 m, and the total length of the computational domain is 20 m. We use a time step (Δt) and grid size (Δx) small enough to obtain convergent solutions. It is determined that, for Radder and Dingemans' model, $\Delta t=T/100$ s, $\Delta x=L/20$ m, and, for Kubo et al.'s model, $\Delta t=T/10$ s, $\Delta x=L/100$ m. Figure 2.26 shows the water surface elevations from $t=50T$ to $t=55T$ with a half wave period interval where the solid lines are exact solutions of equation (2.44), the dashed lines are results from Radder and Dingemans' equation and the dash-dotted lines are results from Kubo et al.'s equation. Kubo et al.'s model

yields more accurate solutions than Radder and Dingemans' model. Figure 2.27 shows the propagation of wave phase and wave groups for Radder and Dingemans' model and Kubo et al.'s model. The wave phase propagation is plotted through the zero-up crossings of water surface elevations from $t = 50T$ to $t = 55T$ and the wave group propagation is plotted through the nodes of wave amplitudes from $t = 50T$ to $t = 55T$.

Second, we test the two models for intermediate-depth water ($\bar{k}h = 0.3\pi$). The water depth is 1 m, the wave height is 0.15 m, the carrier wave period (T) is 2.4085 s, the carrier wavelength (L) is 6.67 m, and the total length of the computational domain is 150 m. It is determined that, for Radder and Dingemans' model, $\Delta t = T/80$ s, $\Delta x = L/13.33$ m, and, for Kubo et al.'s model, $\Delta t = T/10$ s, $\Delta x = L/66.67$ m. Figure 2.28 shows the water surface elevations from $t = 40T$ to $t = 45T$ with a half wave period interval where the solid lines are exact solutions of equation (2.44), the dashed lines are results from Radder and Dingemans' equation and the dash-dotted lines are results from Kubo et al.'s equation. Kubo et al.'s model yields more accurate solutions than Radder and Dingemans' model. Figure 2.29 shows the propagation of the wave phase and groups from $t = 40T$ to $t = 50T$ for Radder and Dingemans' model and Kubo et al.'s model.

Third, we test the two models for shallow water ($\bar{k}h = 0.05\pi$). The water depth is 1 m, the wave height is 0.15 m, the carrier wave period (T) is 12.8258 s, the carrier wavelength (L) is 40 m, and the total length of the computational domain is 800 m. It is determined that, for Radder and Dingemans' model, $\Delta t = T/100$ s, $\Delta x = L/16$ m, and, for Kubo et al.'s model, $\Delta t = T/10$ s, $\Delta x = L/40$ m. Figure 2.30 shows the water surface elevations from $t = 30T$ to $t = 35T$ with a half wave period interval where the solid lines are exact solutions of equation (2.44), the dashed lines are results from Radder and Dingemans' equation

and the dash-dotted lines are results from Kubo et al.'s equation. Radder and Dingemans' model yields more accurate solutions than Kubo et al.'s model. Figure 2.31 shows the propagation of the wave phase and wave groups from $t = 30T$ to $t = 40T$ for Radder and Dingemans' model and Kubo et al.'s model.

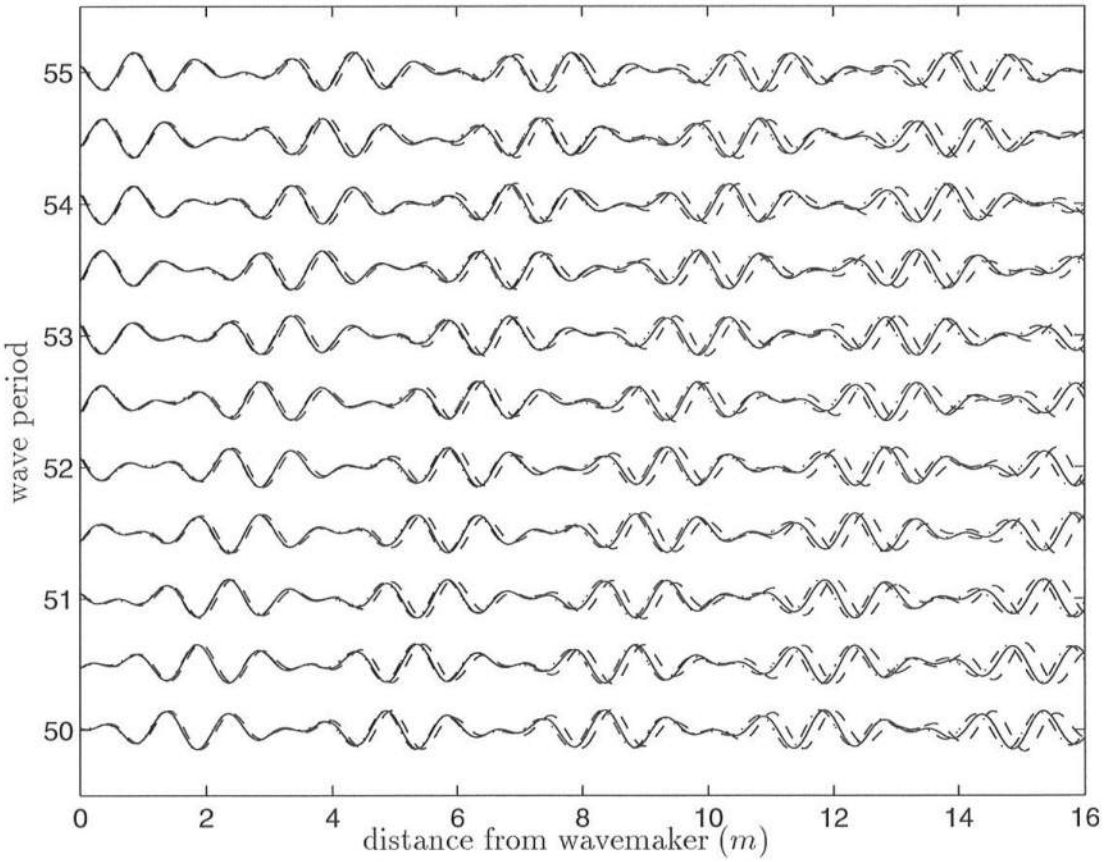

Figure 2.26: Water surface elevations for $\bar{k}h = 2\pi$, $\Delta k/\bar{k} = 0.15$ (solid line: exact solution, dashed line: Radder and Dingemans' model, dash-dotted line: Kubo et al.'s model)

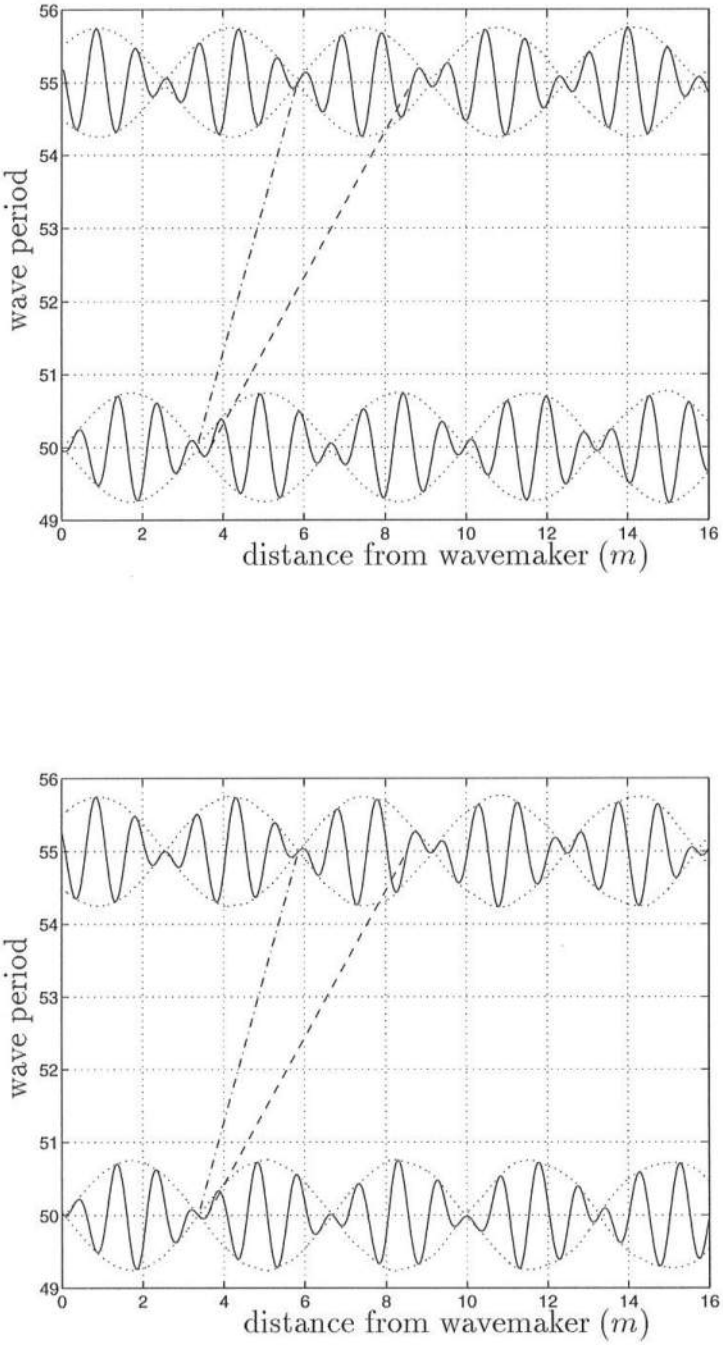

Figure 2.27: Propagation of wave phase and wave groups for $\bar{k}h = 2\pi$, $\Delta k/\bar{k} = 0.15$ (dashed line: wave phase, dash-dotted line: wave groups) (a) Radder and Dingemans' model, (b) Kubo et al.'s model

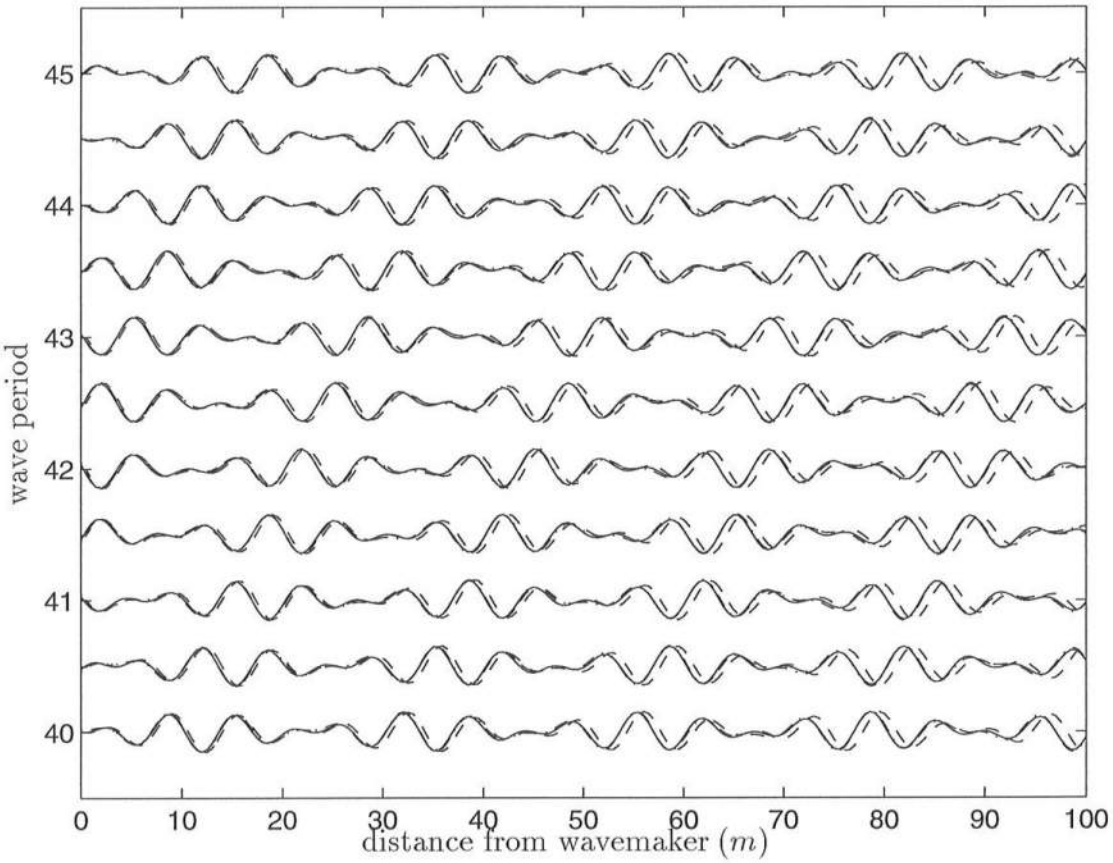

Figure 2.28: Water surface elevations for $\bar{k}h = 0.3\pi$, $\Delta k/\bar{k} = 0.15$ (solid line: exact solution, dashed line: Radder and Dingemans' model, dash-dotted line: Kubo et al.'s model)

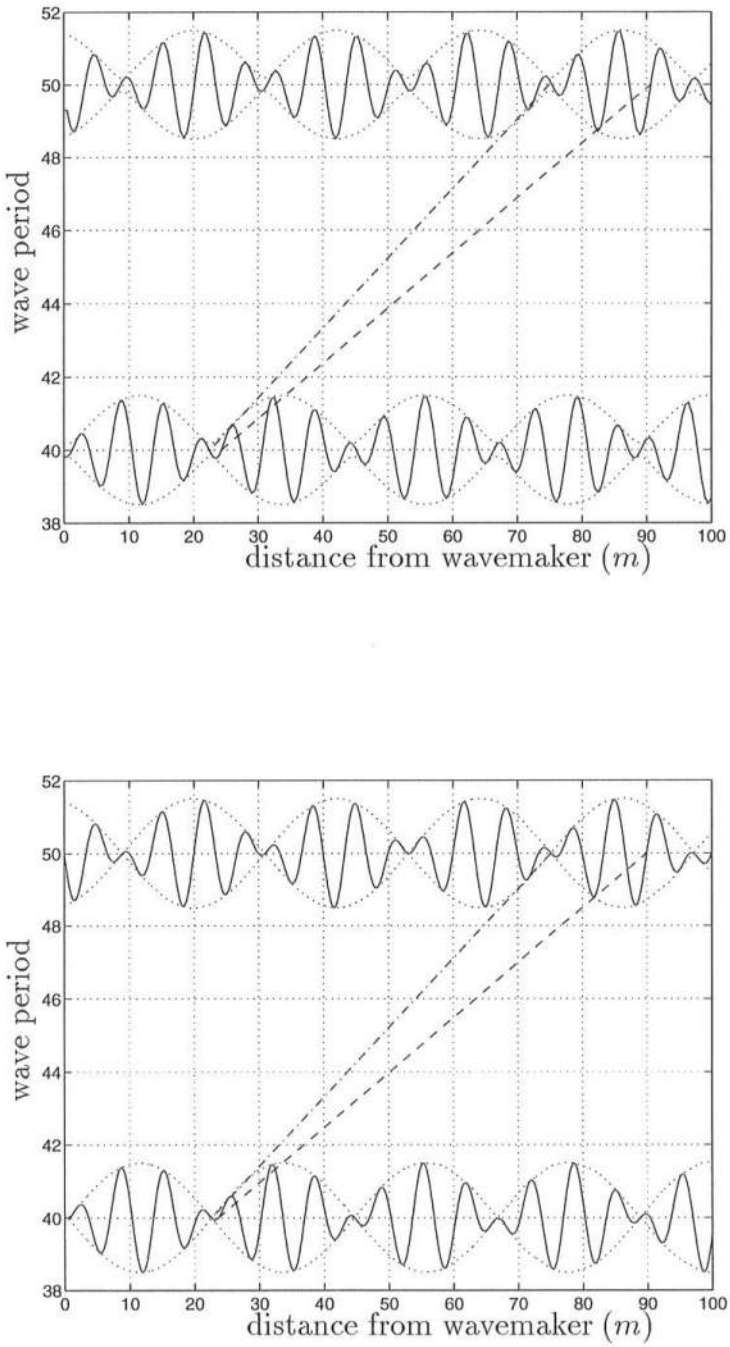

Figure 2.29: Propagation of wave phase and wave groups for $\bar{k}h = 0.3\pi$, $\Delta k/\bar{k} = 0.15$ (dashed line: wave phase, dash-dotted line: wave groups) (a) Radder and Dingemans' model, (b) Kubo et al.'s model

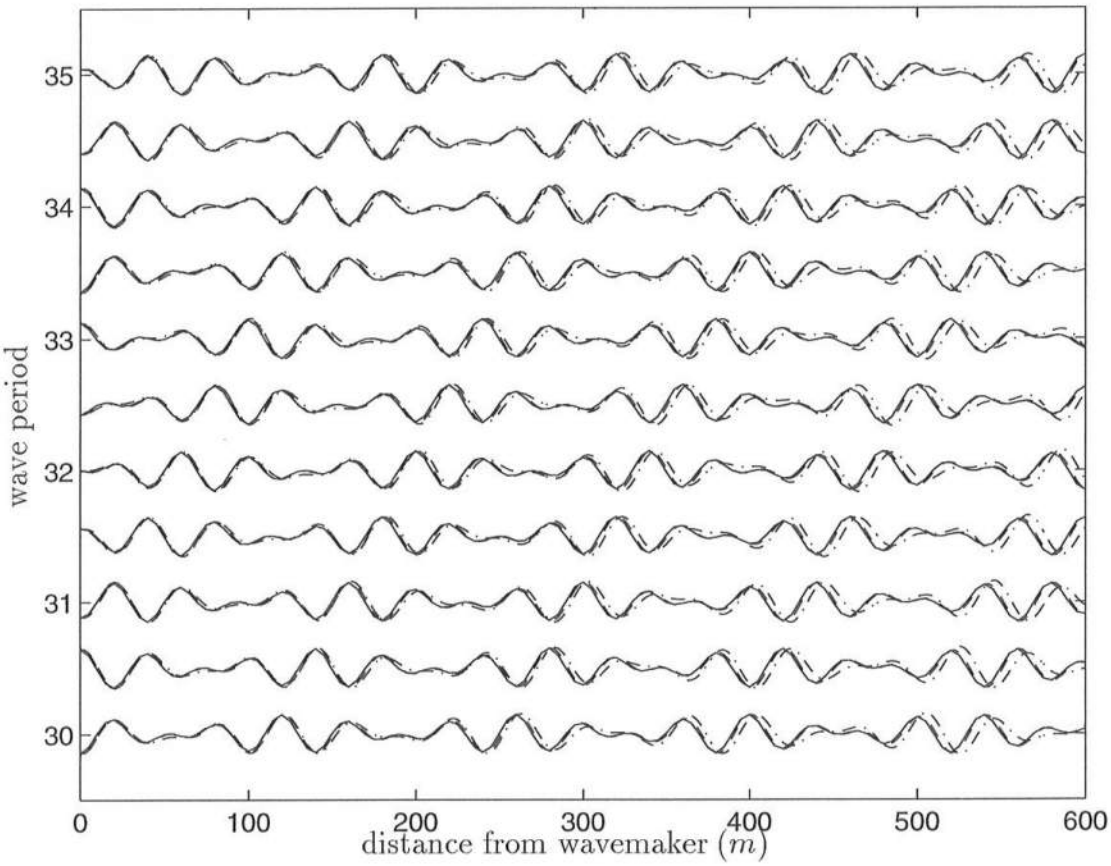

Figure 2.30: Water surface elevations for $\bar{k}h = 0.05\pi$, $\Delta k/\bar{k} = 0.15$ (solid line: exact solution, dashed line: Radder and Dingemans' model, dash-dotted line: Kubo et al.'s model)

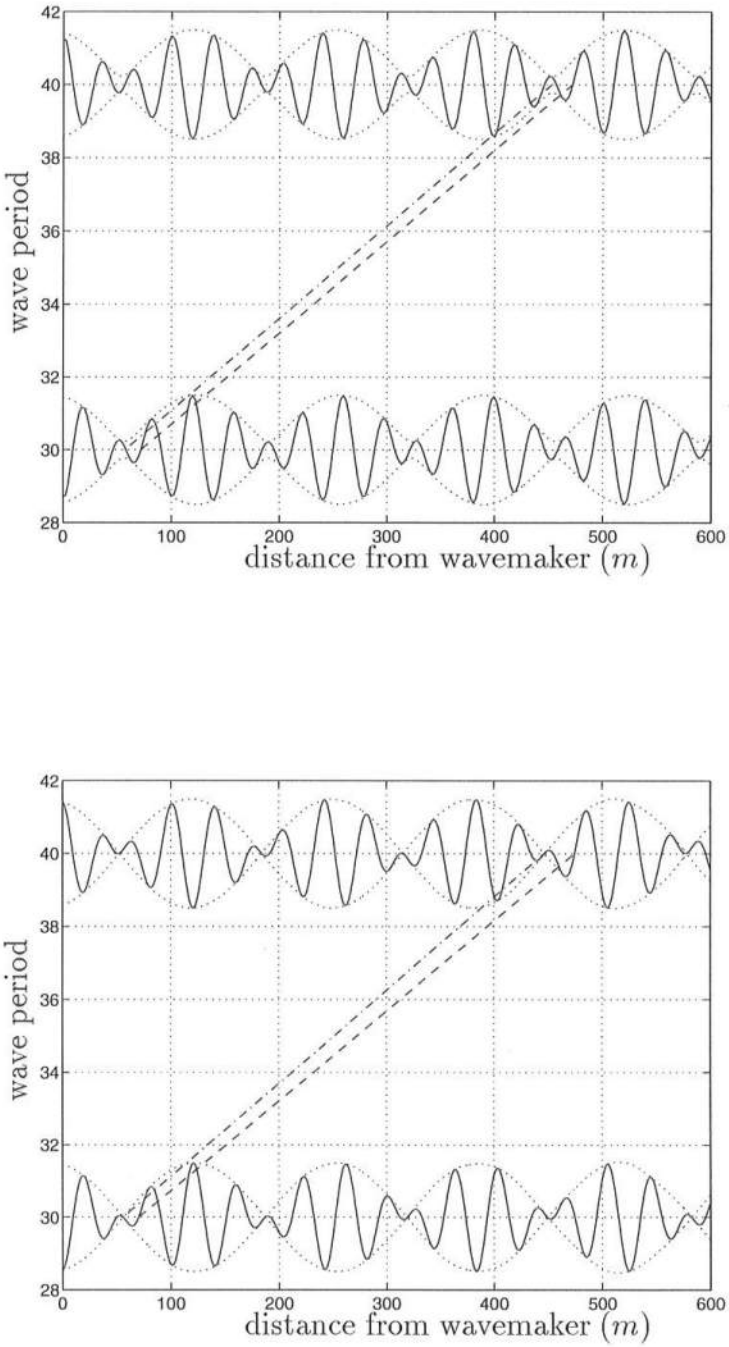

Figure 2.31: Propagation of wave phase and wave groups for $\bar{k}h = 0.05\pi$, $\Delta k/\bar{k} = 0.15$ (dashed line: wave phase, dash-dotted line: wave groups) (a) Radder and Dingemans' model, (b) Kubo et al.'s model

Chapter 3

NEW TIME-DEPENDENT MILD-SLOPE EQUATIONS

We found in Chapter 2 that neither of the two existing time-dependent mild-slope equations satisfies the linear Schrödinger equation in all water depths, from deep to shallow water. It is found that Smith and Sprinks' model (2.3) is more accurate in shallow water and satisfies the linear Schrödinger equation in very shallow water ($\bar{k}h \simeq 0$) and Kubo et al.'s model (2.7) is more accurate in intermediate-depth and deep water and satisfies the linear Schrödinger equation at a point of intermediate-depth water ($\bar{k}h \simeq 0.3\pi$). Here we suggest two new time-dependent mild-slope equations both of which satisfy the linear Schrödinger equation and both of which are more accurate than Smith and Sprinks' and Kubo et al.'s models (2.3) and (2.7) in all water depths. The new time-dependent mild-slope equations are analyzed and compared with the two existing models from a geometric optics point of view, which yields the dispersion relation and the transport equation for wave energy. The new time-dependent mild-slope equations are also analyzed in view of wave kinematics. The case of bichromatic waves is tested analytically and numerically to see how well the second new time-dependent mild-slope equation predicts the propagation of the wave phase and groups.

3.1 Derivation of New Time-Dependent Mild-Slope Equations

We found that neither Smith and Sprinks' model (2.3) nor Kubo et al.'s model (2.7) satisfies the linear Schrödinger equation in all water depths. We modify the two models by adding correcting terms in order to derive models which satisfy the linear Schrödinger equation. The new time-dependent mild-slope equations are valid one-dimensionally in the horizontal direction.

First, we suggest the following time-dependent mild-slope equation using Smith and Sprinks' equation (2.3):

$$\frac{\partial^2\tilde{\phi}}{\partial t^2} - \frac{\partial}{\partial x}(\bar{C}\bar{C}_g\frac{\partial\tilde{\phi}}{\partial x}) + (\bar{\omega}^2 - \bar{k}^2\bar{C}\bar{C}_g)\tilde{\phi} + \alpha_1\tilde{\phi} + \alpha_2\frac{\partial\tilde{\phi}}{\partial t} + \alpha_3\frac{\partial^2\tilde{\phi}}{\partial t^2} = 0 \tag{3.1}$$

where the coefficients, α_1, α_2 and α_3, will be chosen to make equation (3.1) satisfy the linear Schrödinger equation (2.37). Substitution of equation (2.30) into equation (3.1) yields the equation for modulation of wave amplitudes $\bar{A}$:

$$\begin{aligned} &-2i\bar{\omega}(\frac{\partial\bar{A}}{\partial t} + \bar{C}_g\frac{\partial\bar{A}}{\partial x}) + (\alpha_1 - i\alpha_2\bar{\omega} - \alpha_3\bar{\omega}^2)\bar{A} \\ &+(\alpha_2 - 2i\alpha_3\bar{\omega})\frac{\partial\bar{A}}{\partial t} + (1+\alpha_3)\frac{\partial^2\bar{A}}{\partial t^2} - \bar{C}\bar{C}_g\frac{\partial^2\bar{A}}{\partial x^2} = 0 \end{aligned} \tag{3.2}$$

or

$$\begin{aligned} &\frac{\partial\bar{A}}{\partial t} + \bar{C}_g\frac{\partial\bar{A}}{\partial x} + i\frac{1}{2\bar{\omega}}(\alpha_1 - i\alpha_2\bar{\omega} - \alpha_3\bar{\omega}^2)\bar{A} \\ &+i\frac{1}{2\bar{\omega}}(\alpha_2 - 2i\alpha_3\bar{\omega})\frac{\partial\bar{A}}{\partial t} + i\frac{1}{2\bar{\omega}}(\alpha_3\bar{C}_g + \bar{C}_g - \bar{C})\bar{C}_g\frac{\partial^2\bar{A}}{\partial x^2} = 0 \end{aligned} \tag{3.3}$$

where we use equation (2.40). If equation (3.3) is matched to the linear Schrödinger equation (2.37), we can find the coefficients as

$$\alpha_1 = -\alpha_3\bar{\omega}^2 \tag{3.4}$$

$$\alpha_2 = 2i\alpha_3\bar{\omega} \tag{3.5}$$

$$\alpha_3 = \frac{1}{\bar{C}_g^2}\{-\bar{\omega}\bar{\omega}'' + \bar{C}_g(\bar{C} - \bar{C}_g)\} \tag{3.6}$$

So, we get a new time-dependent mild-slope equation

$$\frac{\partial^2\tilde{\phi}}{\partial t^2} - \frac{\partial}{\partial x}(\bar{C}\bar{C}_g\frac{\partial\tilde{\phi}}{\partial x}) + (\bar{\omega}^2 - \bar{k}^2\bar{C}\bar{C}_g)\tilde{\phi} + \alpha_3(\frac{\partial^2\tilde{\phi}}{\partial t^2} + 2i\bar{\omega}\frac{\partial\tilde{\phi}}{\partial t} - \bar{\omega}^2\tilde{\phi}) = 0 \tag{3.7}$$

In very shallow water ($\bar{k}h \simeq 0$), α_3 becomes zero, and the suggested equation (3.7) is the same as Smith and Sprinks' equation (2.3). The value of α_3 can be seen in the difference of the coefficients of $\frac{\partial^2\bar{A}}{\partial x^2}$ between equations (2.37) and (2.39), and also in the coefficient of equation (2.48) for bichromatic waves.

Second, we suggest the following time-dependent mild-slope equation using Kubo et al.'s equation (2.7):

$$\frac{\partial}{\partial x}(\bar{C}\bar{C}_g\frac{\partial\hat{\phi}}{\partial x}) + \bar{k}^2\bar{C}\bar{C}_g\hat{\phi} + i\frac{\partial}{\partial x}\{\frac{\partial}{\partial\omega}(\bar{C}\bar{C}_g)\frac{\partial^2\hat{\phi}}{\partial x\partial t}\} + i\frac{\partial}{\partial\omega}(\bar{k}^2\bar{C}\bar{C}_g)\frac{\partial\hat{\phi}}{\partial t} + \beta_1\hat{\phi} + \beta_2\frac{\partial\hat{\phi}}{\partial t} + \beta_3\frac{\partial^2\hat{\phi}}{\partial t^2} = 0 \tag{3.8}$$

where the coefficients, β_1, β_2, and β_3, are chosen to make equation (3.8) satisfy the linear Schrödinger equation (2.37). Substitution of equation (2.41) into equation (3.8) yields the equation for modulation of wave amplitudes $\bar{A}$:

$$2i\bar{\omega}(\frac{\partial\bar{A}}{\partial t} + \bar{C}_g\frac{\partial\bar{A}}{\partial x}) + \bar{C}\bar{C}_g\frac{\partial^2\bar{A}}{\partial x^2} + i\frac{\partial}{\partial\omega}(\bar{C}\bar{C}_g)(\frac{\partial^3\bar{A}}{\partial x^2\partial t} + 2i\bar{k}\frac{\partial^2\bar{A}}{\partial x\partial t}) + \beta_1\bar{A} + \beta_2\frac{\partial\bar{A}}{\partial t} + \beta_3\frac{\partial^2\bar{A}}{\partial t^2} = 0 \tag{3.9}$$

or

$$\frac{\partial\bar{A}}{\partial t} + \bar{C}_g\frac{\partial\bar{A}}{\partial x} - i\{\bar{\omega}'' + \frac{\bar{C}_g}{2\bar{\omega}}(2\bar{C}_g - \bar{C}) + \beta_3\frac{\bar{C}_g^2}{2\bar{\omega}}\}\frac{\partial^2\bar{A}}{\partial x^2} - i\frac{1}{2\bar{\omega}}(\beta_1\bar{A} + \beta_2\frac{\partial\bar{A}}{\partial t}) = 0 \tag{3.10}$$

where we use equation (2.40) and neglect the term smaller than $O(\Delta k)^2$. If equation (3.10) is matched to the linear Schrödinger equation (2.37), we can find the coefficients as

$$\beta_1 = 0 \tag{3.11}$$

$$\beta_2 = 0 \tag{3.12}$$

$$\begin{aligned}\beta_3 &= \alpha_3 - 1 \\ &= \frac{1}{\bar{C}_g^2}\{-\bar{\omega}\bar{\omega}'' + \bar{C}_g(\bar{C} - 2\bar{C}_g)\}\end{aligned} \tag{3.13}$$

So, we get another new time-dependent mild-slope equation

$$\begin{aligned}\frac{\partial}{\partial x}(\bar{C}\bar{C}_g\frac{\partial\hat{\phi}}{\partial x}) + \bar{k}^2\bar{C}\bar{C}_g\hat{\phi} + i\frac{\partial}{\partial x}\{\frac{\partial}{\partial\omega}(\bar{C}\bar{C}_g)\frac{\partial^2\hat{\phi}}{\partial x\partial t}\} \\ +i\frac{\partial}{\partial\omega}(\bar{k}^2\bar{C}\bar{C}_g)\frac{\partial\hat{\phi}}{\partial t} + \beta_3\frac{\partial^2\hat{\phi}}{\partial t^2} = 0\end{aligned} \tag{3.14}$$

The value of β_3 is equal to $\alpha_3 - 1$. The value of β_3 is -1 in very shallow water ($\bar{k}h \simeq 0$), and increases as depth increases, until it becomes 1.2 at a point of intermediate-depth water ($\bar{k}h \simeq 0.7\pi$), and decreases to 1 in deep water ($\bar{k}h \geq 2\pi$) asymptotically. At a point of intermediate depth ($\bar{k}h \simeq 0.3\pi$), β_3 becomes zero and so the suggested equation (3.14) happens to be the same as Kubo et al.'s equation (2.7) (see Figure 3.1). The value of β_3 can be seen in the difference of the coefficients of $\frac{\partial^2\bar{A}}{\partial x^2}$ between equations (2.37) and (2.43), and also in the coefficient of equation (2.50) for bichromatic waves.

For the first suggested equation (3.7), the geometric optics approximation is constructed by substituting the ansatz

$$\check{\phi}(x,t) = A(x,t)e^{i(\int kdx - \omega t)} \tag{3.15}$$

into equation (3.7), which yields

$$\begin{aligned}-(\omega-\bar{\omega})\{(1+\alpha_3)\omega - (1-\alpha_3)\bar{\omega}\}A + (k^2 - \bar{k}^2)\bar{C}\bar{C}_gA - \frac{\partial}{\partial x}(\bar{C}\bar{C}_g\frac{\partial A}{\partial x}) \\ +i\frac{1}{A}\nabla(A^2k\bar{C}\bar{C}_g) = 0\end{aligned} \tag{3.16}$$

Separation of real and imaginary parts of the resulting equation leads to an eikonal equation for the phase function

$$\frac{(\omega-\bar{\omega})\{(1+\alpha_3)\omega - (1-\alpha_3)\bar{\omega}\}}{\bar{C}\bar{C}_g} = k^2 - \bar{k}^2 - \frac{\frac{\partial}{\partial x}(\bar{C}\bar{C}_g\frac{\partial A}{\partial x})}{\bar{C}\bar{C}_gA} \tag{3.17}$$

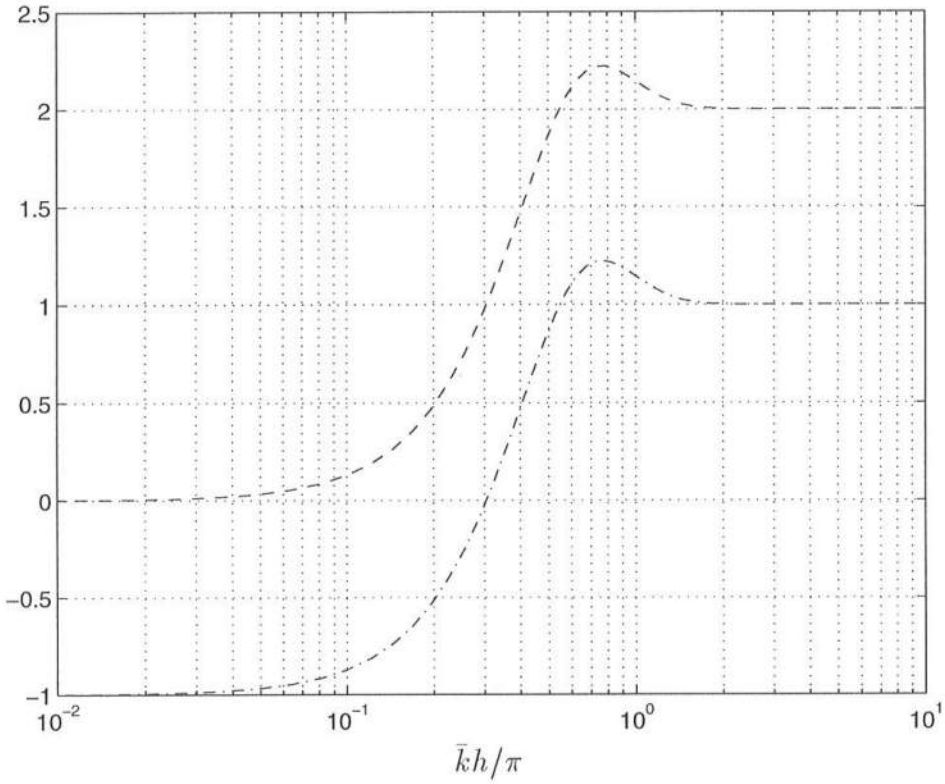

Figure 3.1: α_3: dashed line, β_3: dash-dotted line

and a transport equation for wave energy

$$\frac{\partial}{\partial x}(A^2 k \bar{C} \bar{C}_g) = 0 \tag{3.18}$$

The last term in equation (3.17) is the weak diffraction, which is small in the second order. Neglecting terms that are second order in equation (3.17) leads to the following dispersion relation

$$\frac{k}{\bar{k}} = \sqrt{1 + \frac{(\frac{\omega}{\bar{\omega}} - 1)\{(1+\alpha_3)\frac{\omega}{\bar{\omega}} + 1 - \alpha_3\}}{\bar{n}}} \tag{3.19}$$

For the second suggested equation (3.14), the geometric optics approximation is constructed by substituting the ansatz

$$\hat{\phi}(x,t) = \tilde{\phi} e^{i\bar{\omega}t} = A(x,t) e^{i(\int k dx - (\omega - \bar{\omega})t)} \tag{3.20}$$

into equation (3.14), which yields

$$
\begin{aligned}
&-\beta_3(\omega-\bar{\omega})^2 A+(\omega-\bar{\omega})\{\frac{\partial}{\partial\omega}(\bar{k}^2\bar{C}\bar{C}_g)-k^2\frac{\partial}{\partial\omega}(\bar{C}\bar{C}_g)\}A \\
&-(k^2-\bar{k}^2)\bar{C}\bar{C}_g A+\frac{\partial}{\partial x}(\bar{C}\bar{C}_g\frac{\partial A}{\partial x})+(\omega-\bar{\omega})\frac{\partial}{\partial x}\{\frac{\partial}{\partial\omega}(\bar{C}\bar{C}_g)\frac{\partial A}{\partial x}\} \\
&+i\frac{1}{A}\frac{\partial}{\partial x}[A^2 k\{\bar{C}\bar{C}_g+(\omega-\bar{\omega})\frac{\partial}{\partial\omega}(\bar{C}\bar{C}_g)\}]=0
\end{aligned}
\tag{3.21}
$$

Separation of the real and imaginary parts of the resulting equation leads to an eikonal equation for the phase function

$$
\begin{aligned}
&-\frac{\beta_3(\omega-\bar{\omega})^2}{\bar{C}\bar{C}_g}+\frac{\omega-\bar{\omega}}{\bar{C}\bar{C}_g}\{\frac{\partial}{\partial\omega}(\bar{k}^2\bar{C}\bar{C}_g)-k^2\frac{\partial}{\partial\omega}(\bar{C}\bar{C}_g)\} \\
&=k^2-\bar{k}^2-\frac{\frac{\partial}{\partial x}(\bar{C}\bar{C}_g\frac{\partial A}{\partial x})}{\bar{C}\bar{C}_g A}-(\omega-\bar{\omega})\frac{\frac{\partial}{\partial x}\{\frac{\partial}{\partial\omega}(\bar{C}\bar{C}_g)\frac{\partial A}{\partial x}\}}{\bar{C}\bar{C}_g A}
\end{aligned}
\tag{3.22}
$$

and a transport equation for wave energy

$$
\frac{\partial}{\partial x}[A^2 k\{\bar{C}\bar{C}_g+(\omega-\bar{\omega})\frac{\partial}{\partial\omega}(\bar{C}\bar{C}_g)\}]=0 \tag{3.23}
$$

The last two terms in equation (3.22) are the weak diffraction with an additional correcting term obtained by the Taylor series expansion. Neglecting terms that are second order in equation (3.22) leads to the following dispersion relation

$$
\frac{k}{\bar{k}}=\sqrt{1+\frac{(\frac{\omega}{\bar{\omega}}-1)\{2-\beta_3(\frac{\omega}{\bar{\omega}}-1)\}}{\bar{n}+(\frac{\omega}{\bar{\omega}}-1)\frac{\bar{k}^2}{\bar{\omega}}\frac{\partial}{\partial\omega}(\bar{C}\bar{C}_g)}} \tag{3.24}
$$

These dispersion relations (3.19) and (3.24) can be compared against the exact dispersion relation for linear waves (2.20). The percent errors in $k/\bar{k}$ for equations (3.19) and (3.24) are shown in Figures 3.2 and 3.3, respectively. Figures 3.4 - 3.6 show the following dispersion relations: for the exact solution, (2.20), for the linear Schrödinger equation, (2.35), for the first suggested equation, (3.19), and for the second suggested equation, (3.24), at deep water ($\bar{k}h=2\pi$), intermediate-depth water ($\bar{k}h=0.3\pi$), and shallow water ($\bar{k}h=0.05\pi$), respectively. Figures 3.2, 3.4 - 3.6 can be compared to Figures 2.3, 2.5 - 2.7. The dispersion relations

from the new model (3.7) are improved from those of Smith and Sprinks' model (2.3) in all water depths, particularly in deep water. Figures 3.3, 3.4 - 3.6 can be compared to Figures 2.4, 2.5 - 2.7. The dispersion relations from the new model (3.14) are improved from those of Kubo et al.'s model (2.7) in all water depths except in deep water with frequencies lower than $\bar{\omega}$. From Figures 2.25, 3.2 - 3.6, we see that the dispersion relations from both new models are not so improved as those from the linear Schrödinger equation. The dispersion relations from equation (3.7) are more accurate than those from equation (3.14) in deep water, and the dispersion relations from equation (3.7) are less accurate than those from equation (3.14) in intermediate-depth and shallow water; while the dispersion relations from Smith and Sprinks' model (2.3) are more accurate than those from Kubo et al.'s model (2.7) in shallow water and the dispersion relations from Smith and Sprinks' model (2.3) are less accurate than those from Kubo et al.'s model (2.7) in intermediate-depth and shallow water.

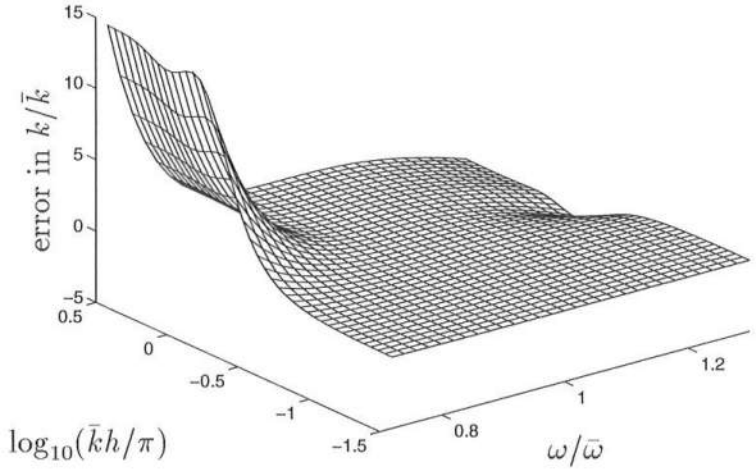

Figure 3.2: Percent errors in $k/\bar{k}$ for new model (3.7)

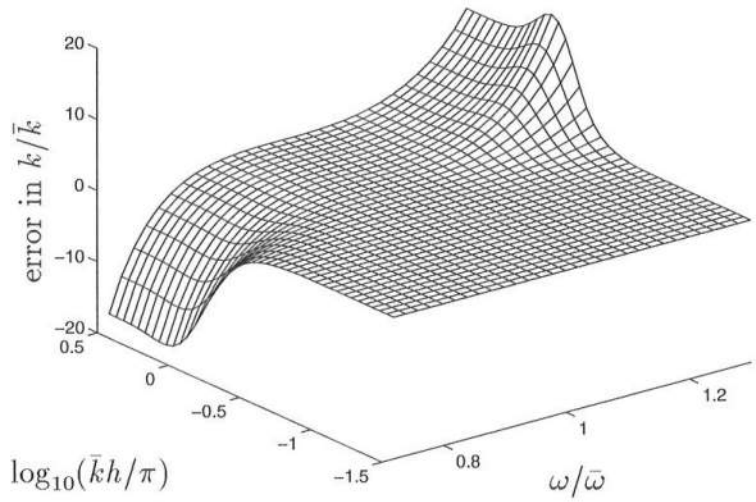

Figure 3.3: Percent errors in $k/\bar{k}$ for new model (3.14)

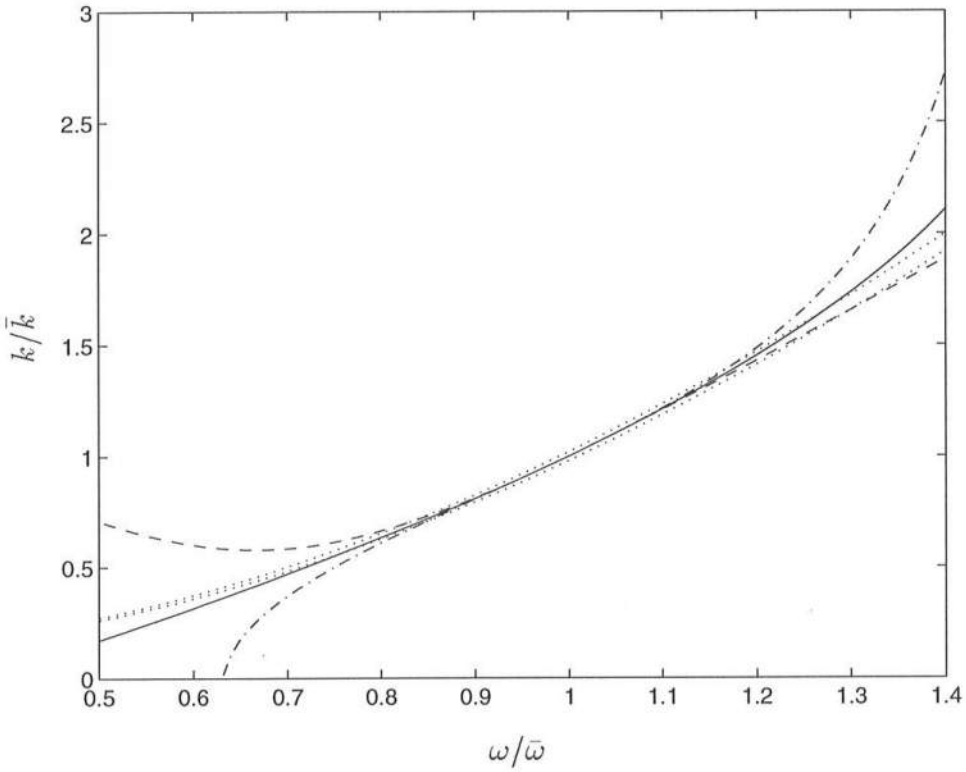

Figure 3.4: Dispersion relations for $\bar{k}h = 2\pi$ (dotted line: 2 percent confidence interval of exact solution, solid line: linear Schrödinger equation, dashed line: new model (3.7), dash-dotted line: new model (3.14))

The shoaling coefficients are not improved from the original equations because corrections are introduced in the time derivatives. Equation (3.18) is equal to (2.13) and equation (3.23) is equal to (2.18) one-dimensionally in the horizonal direction.

We analyze the new time-dependent mild-slope equations, (3.7) and (3.14), in terms of wave kinematics. For irregular waves, the particle velocity in the the x direction can be described by equation (2.25). When the time-dependent mild-slope equation is used in obtaining the particle velocity in the x direction, we get the particle velocity in the x direction by equation (2.26).

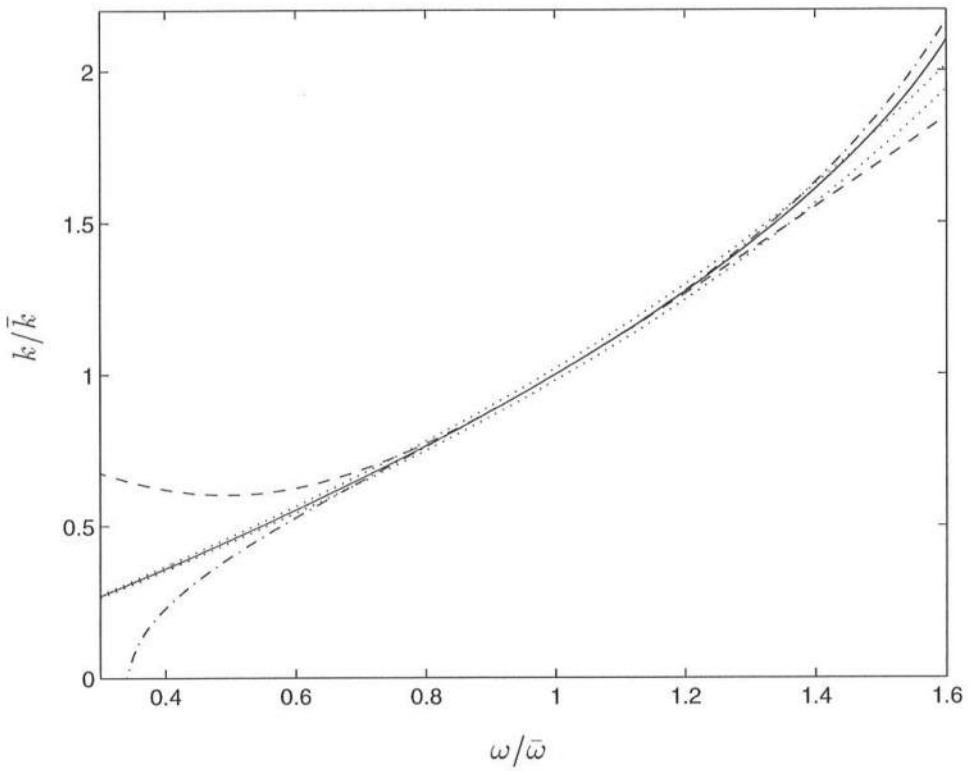

Figure 3.5: Dispersion relations for $\bar{k}h = 0.3\pi$ (dotted line: 2 percent confidence interval of exact solution, solid line: linear Schrödinger equation, dashed line: new model (3.7), dash-dotted line: new model (3.14))

We test the difference of the variance of the particle velocities for the case of experiments done by Mase and Kirby (1992). We use case 1 of the experiment where the breaking waves are of the plunging breaker type. We exclude the lower and upper 2 percent frequency spectra from the whole spectrum, so the frequency range is $f = 0.38 - 1.61\ Hz$. We subdivide the spectrum in 2, 4, 6, or 8 components with equal frequency bandwidths. We select the representative frequencies by a median or weighted average. For the weighted average case, we compute the representative frequencies by averaging the frequencies with the weight of the power spectrum.

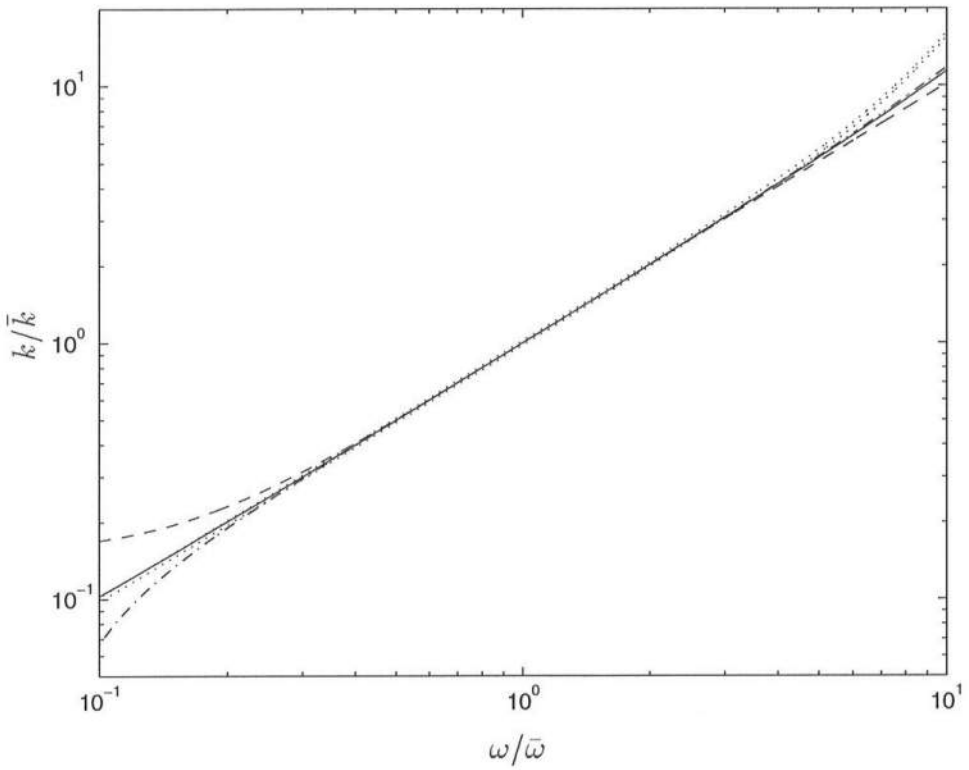

Figure 3.6: Dispersion relations for $\bar{k}h = 0.05\pi$ (dotted line: 2 percent confidence interval of exact solution, solid line: linear Schrödinger equation, dashed line: new model (3.7), dash-dotted line: new model (3.14))

We compute the variance of the particle velocities from equation (2.27) and (2.28) and then compute the percent error. Figure 2.19 shows the squared amplitude of the particle velocities. Figures 3.7 and 3.8 show the percent error of the squared amplitude of the particle velocities at $z = 0$ for the new model equations (3.14) and (3.7). Figure 3.9 shows the percent errors of the variance of particle velocities at $z = 0$ in all water depths for 2, 4, 6, or 8 frequency bands with equal bandwidths.

Figure 3.9 can be compared to Figure 2.22. The range of the percent

errors in variance of the particle velocities from the new models (3.7) and (3.14) are smaller than those from the original models (2.3) and (2.7) for all frequency bands, but the percent errors from the new models are not smaller than those from the original models in all water depths. The percent errors in variance of the particle velocities from equation (3.14) are smaller than those from equation (3.7) except when using 2 frequency bands. The percent errors in variance of the particle velocities at $z = -h$ in all water depths are shown in Figure 3.10. The comparison of Figures 3.10 and 2.23 shows that the errors from the new models are not smaller than those from the original models.

Overall, the second suggested equation (3.14) is more accurate than the first suggested equation (3.7). In the following section, we analyze the second suggested equation (3.14) in more detail with a numerical simulation.

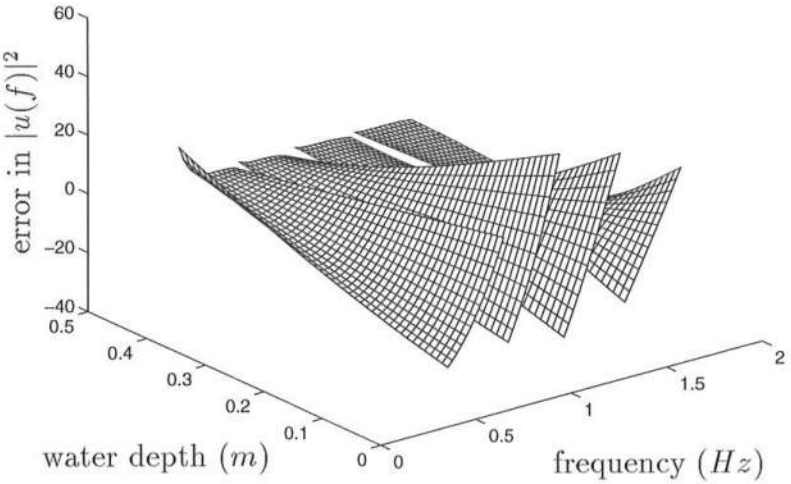

Figure 3.7: Percent errors in squared particle velocities at $z = 0$ (new model (3.7) with 4 frequency bands using weight-averaged frequencies)

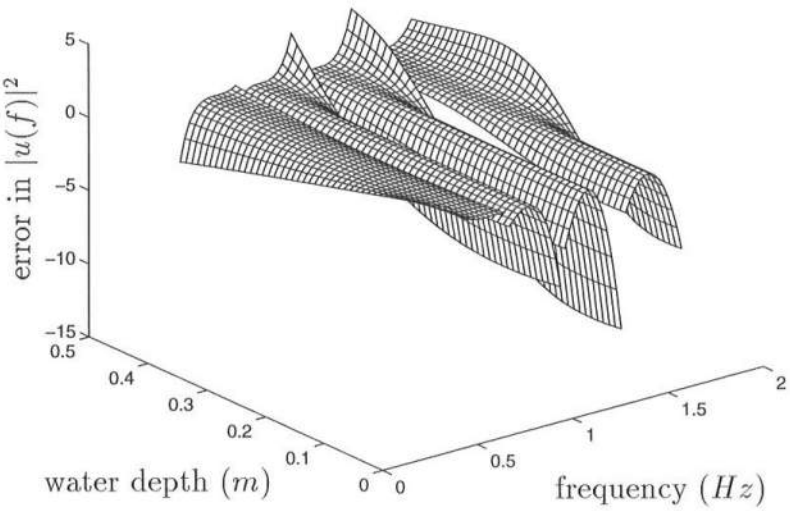

Figure 3.8: Percent errors in squared particle velocities at $z = 0$ (new model (3.14) with 4 frequency bands using weight-averaged frequencies)

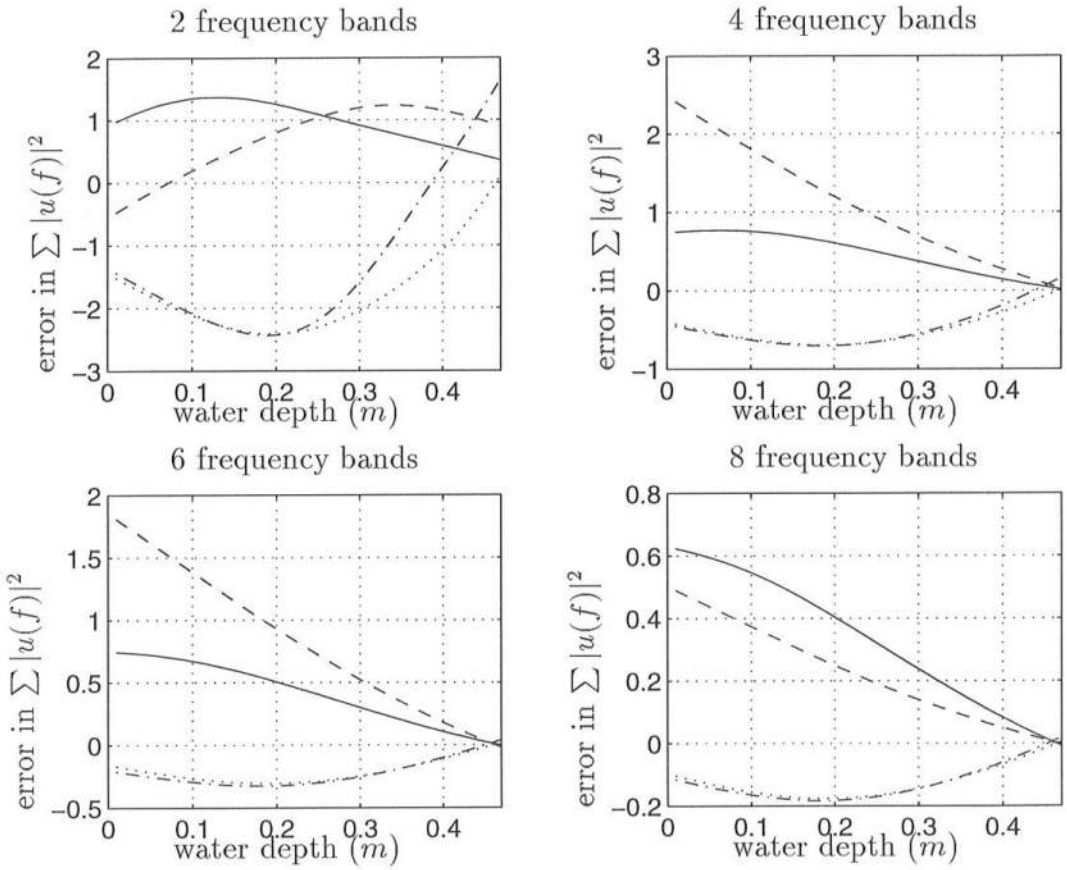

Figure 3.9: Percent errors in variance of particle velocities at $z = 0$ when frequency bandwidth is equal (solid line: new model (3.7) using weight-averaged frequencies, dashed line: new model (3.7) using centered frequencies, dash-dotted line: new model (3.14) using weight-averaged frequencies, dotted line: new model (3.14) using centered frequencies)

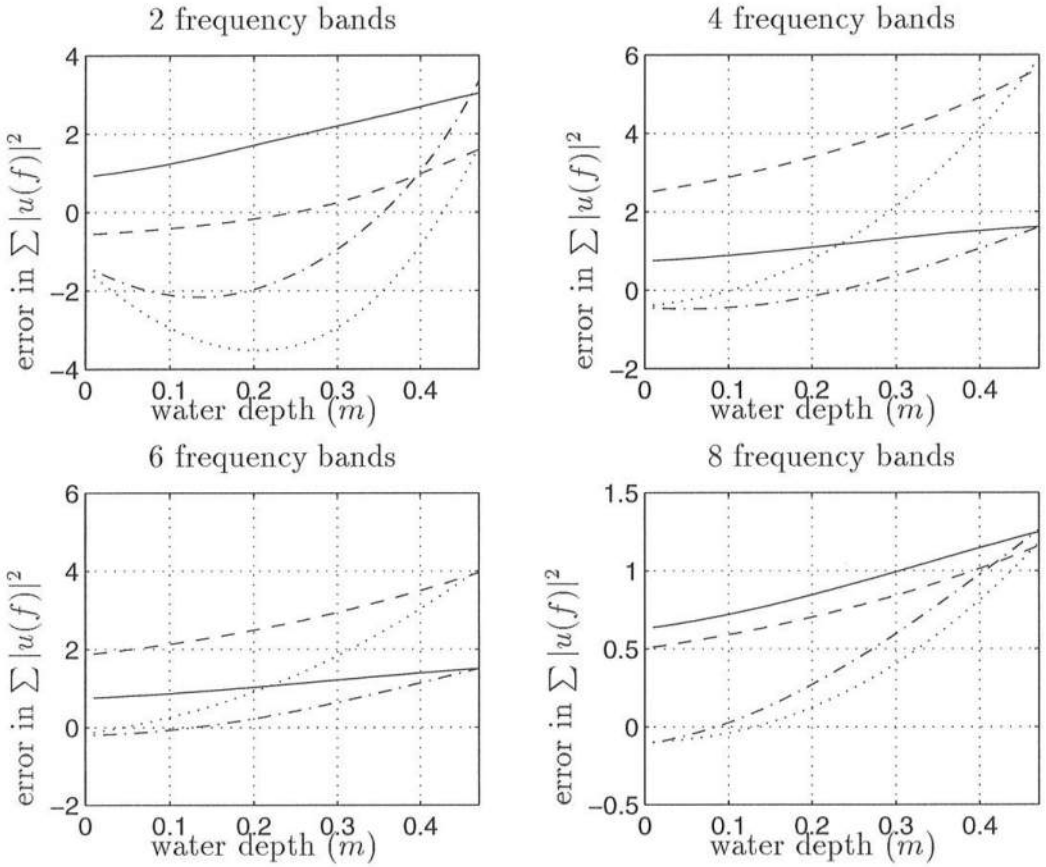

Figure 3.10: Percent errors in variance of particle velocities at $z = -h$ when frequency bandwidth is equal (solid line: new model (3.7) using weight-averaged frequencies, dashed line: new model (3.7) using centered frequencies, dash-dotted line: new model (3.14) using weight-averaged frequencies, dotted line: new model (3.14) using centered frequencies)

3.2 Finite Difference Methods

We discretize equation (3.14), centered in time and in space, as

$$\begin{aligned}
&\frac{1}{2(\Delta x)^2}\Big(((\bar{C}\bar{C}_g)_j + (\bar{C}\bar{C}_g)_{j+1})(\hat{\phi}^n_{j+1} - \hat{\phi}^n_j) - ((\bar{C}\bar{C}_g)_j + (\bar{C}\bar{C}_g)_{j-1})(\hat{\phi}^n_j - \hat{\phi}^n_{j-1})\Big) \\
&\qquad\qquad +(\bar{k}^2\bar{C}\bar{C}_g)_j\hat{\phi}^n_j \\
&+i\frac{1}{4(\Delta x)^2\Delta t}(\frac{\partial}{\partial\omega}(\bar{C}\bar{C}_g)_j + \frac{\partial}{\partial\omega}(\bar{C}\bar{C}_g)_{j+1})((\hat{\phi}^{n+1}_{j+1} - \hat{\phi}^{n+1}_j) - (\hat{\phi}^{n-1}_{j+1} - \hat{\phi}^{n-1}_j)) \\
&-i\frac{1}{4(\Delta x)^2\Delta t}(\frac{\partial}{\partial\omega}(\bar{C}\bar{C}_g)_j + \frac{\partial}{\partial\omega}(\bar{C}\bar{C}_g)_{j-1})((\hat{\phi}^{n+1}_j - \hat{\phi}^{n+1}_{j-1}) - (\hat{\phi}^{n-1}_j - \hat{\phi}^{n-1}_{j-1})) \\
&+i\frac{1}{2\Delta t}\frac{\partial}{\partial\omega}(\bar{k}^2\bar{C}\bar{C}_g)_j(\hat{\phi}^{n+1}_j - \hat{\phi}^{n-1}_j) + \beta_{3j}\frac{1}{(\Delta t)^2}(\hat{\phi}^{n+1}_j - 2\hat{\phi}^n_j + \hat{\phi}^{n-1}_j) = 0
\end{aligned} \tag{3.25}$$

where the subscript j and the superscript n represents space and time indices.

We analyze the discretized equation (3.25) by the von Neumann method. The von Neumann analysis is the most commonly used method of determining stability criteria, and can be used to establish necessary and sufficient conditions for the stability of linear initial value problems with constant coefficients (Fletcher, 1988). In the von Neumann method, the errors distributed along grid lines at one time level are expanded as a finite Fourier series. Then, the stability or instability of the computational algorithm is determined by considering whether separate Fourier components of the error distribution decay or amplify in progressing to the next time level. A solution of equation (3.25) with $\hat{\phi}^n_j$ replaced by errors ξ^n_j is sought in a separation-of-variables form as

$$\xi^n_j = (G)^n e^{i\theta j} \tag{3.26}$$

where the time dependence of this Fourier component of the error is contained in the complex coefficient $(G)^n$, and the superscript n implies G is raised to the

power n. Substitution of equation (3.26) into equation (3.25) with $\hat{\phi}_j^n$ replaced by errors ξ_j^n produces the following equation

$$\begin{aligned} G^2[i\Delta t\{-4\frac{\partial}{\partial\omega}(\bar{C}\bar{C}_g)\sin^2\frac{\theta}{2}+(\Delta x)^2\frac{\partial}{\partial\omega}(\bar{k}^2\bar{C}\bar{C}_g)\}+2(\Delta x)^2\beta_3] \\ +2G[(\Delta t)^2\{-4\bar{C}\bar{C}_g\sin^2\frac{\theta}{2}+(\Delta x)^2\bar{k}^2\bar{C}\bar{C}_g\}-2(\Delta x)^2\beta_3] \\ -i\Delta t\{-4\frac{\partial}{\partial\omega}(\bar{C}\bar{C}_g)\sin^2\frac{\theta}{2}+(\Delta x)^2\frac{\partial}{\partial\omega}(\bar{k}^2\bar{C}\bar{C}_g)\}+2(\Delta x)^2\beta_3=0 \end{aligned} \tag{3.27}$$

where all the variables $\bar{C}\bar{C}_g$, $\bar{k}^2\bar{C}\bar{C}_g$, $\frac{\partial}{\partial\omega}(\bar{C}\bar{C}_g)$, $\frac{\partial}{\partial\omega}(\bar{C}\bar{C}_g)$, and β_3 are at spatial point $j\Delta x$, and the subscript j is dropped for brevity. When the following condition is satisfied

$$\begin{aligned} [(\Delta t)^2\{-4\bar{C}\bar{C}_g\sin^2\frac{\theta}{2}+(\Delta x)^2\bar{k}^2\bar{C}\bar{C}_g\}]^2 \\ -[\Delta t\{-4\frac{\partial}{\partial\omega}(\bar{C}\bar{C}_g)\sin^2\frac{\theta}{2}+(\Delta x)^2\frac{\partial}{\partial\omega}(\bar{k}^2\bar{C}\bar{C}_g)\}]^2 \\ -2[(\Delta t)^2\{-4\bar{C}\bar{C}_g\sin^2\frac{\theta}{2}+(\Delta x)^2\bar{k}^2\bar{C}\bar{C}_g\}][2(\Delta x)^2\beta_3]<0, \end{aligned} \tag{3.28}$$

the absolute value of G is 1, that is, the solution is neutrally stable; otherwise, the solution is unstable. So, the discretized equation (3.25) is conditionally stable and the stability depends not only on parameters $\bar{C}\bar{C}_g$, $\bar{k}^2\bar{C}\bar{C}_g$, $\frac{\partial}{\partial\omega}(\bar{C}\bar{C}_g)$, $\frac{\partial}{\partial\omega}(\bar{C}\bar{C}_g)$, and β_3 but also on the grid size Δx and the time step Δt.

In order to dissipate wave energy at downwave boundaries, we presently use a wave damping layer at the downwave boundary as discussed in relation to equation (2.51). Using the von Neumann stability analysis for equation (3.25) with damping terms, we found a different type of the new time-dependent mild-slope equation. For $\beta_3 > 0$ ($\bar{k}h > 0.3\pi$), the new time-dependent mild-slope equation (3.14) can include the damping terms as:

$$\begin{aligned} \frac{\partial}{\partial x}(\bar{C}\bar{C}_g\frac{\partial\hat{\phi}}{\partial x})+\bar{k}^2\bar{C}\bar{C}_g(1+i\frac{D_s}{\bar{\omega}\bar{n}})\hat{\phi}+i\frac{\partial}{\partial x}(\frac{\partial}{\partial\omega}(\bar{C}\bar{C}_g)\frac{\partial^2\hat{\phi}}{\partial x\partial t}) \\ +i\frac{\partial}{\partial\omega}(\bar{k}^2\bar{C}\bar{C}_g)(1+i\frac{D_s}{\bar{\omega}\bar{n}})\frac{\partial\hat{\phi}}{\partial t}+\beta_3(1+i\frac{D_s}{\bar{\omega}\bar{n}})\frac{\partial^2\hat{\phi}}{\partial t^2}=0 \end{aligned} \tag{3.29}$$

For $\beta_3 < 0$ ($\bar{k}h \leq 0.3\pi$), the new time-dependent mild-slope equation (3.14) can include the damping terms as:

$$\frac{\partial}{\partial x}(\bar{C}\bar{C}_g\frac{\partial\hat{\phi}}{\partial x}) + (\bar{k}^2\bar{C}\bar{C}_g + i\bar{\omega}D_s)\hat{\phi} + i\frac{\partial}{\partial x}(\frac{\partial}{\partial\omega}(\bar{C}\bar{C}_g)\frac{\partial^2\hat{\phi}}{\partial x\partial t}) + i(\frac{\partial}{\partial\omega}(\bar{k}^2\bar{C}\bar{C}_g) + iD_s)\frac{\partial\hat{\phi}}{\partial t} + \beta_3\frac{\partial^2\hat{\phi}}{\partial t^2} = 0 \tag{3.30}$$

3.3 Test of a New Model for Bichromatic Waves

We analyze the new equation (3.14) for the case of bichromatic waves described by equation (2.44). Substitution of the velocity potential $\hat{\phi}$ for Kubo et al.'s equation (2.49) into the new equation (3.14) proves that the new time-dependent mild-slope equation (3.14) is accurate to $O(\Delta k)^2$.

First, we test the new model for deep water ($\bar{k}h = 2\pi$). The water depth is 1 m, the wave height is 0.15 m, the carrier wave period (T) is 0.80046 s, the carrier wavelength (L) is 1 m, and the total length of the computational domain is 20 m. We use equation (3.29) to absorb the incident wave energy. We determine that the time step (Δt) and grid size (Δx) are small enough to obtain convergent solutions. It is determined that $\Delta t = T/40$ s and $\Delta x = L/200$ m. Figure 3.11 shows the water surface elevations from $t = 50T$ to $t = 55T$ with a half wave period interval. The solid lines are exact solutions of equation (2.44), dashed lines are results from the new equation (3.14), and the dash-dotted lines are results from Kubo et al.'s equation (2.7). The new model (3.14) yields more accurate solutions than Kubo et al.'s model (2.7). Figure 3.12 shows the propagation of the wave phase and wave groups for the new model (3.14) from $t = 50T$ to $t = 55T$.

Second, we test the two models for intermediate-depth water ($\bar{k}h = 0.3\pi$). The water depth is 1 m, the wave height is 0.15 m, the carrier wave period (T) is 2.4085 s, the carrier wavelength (L) is 6.67 m, and the total length of the

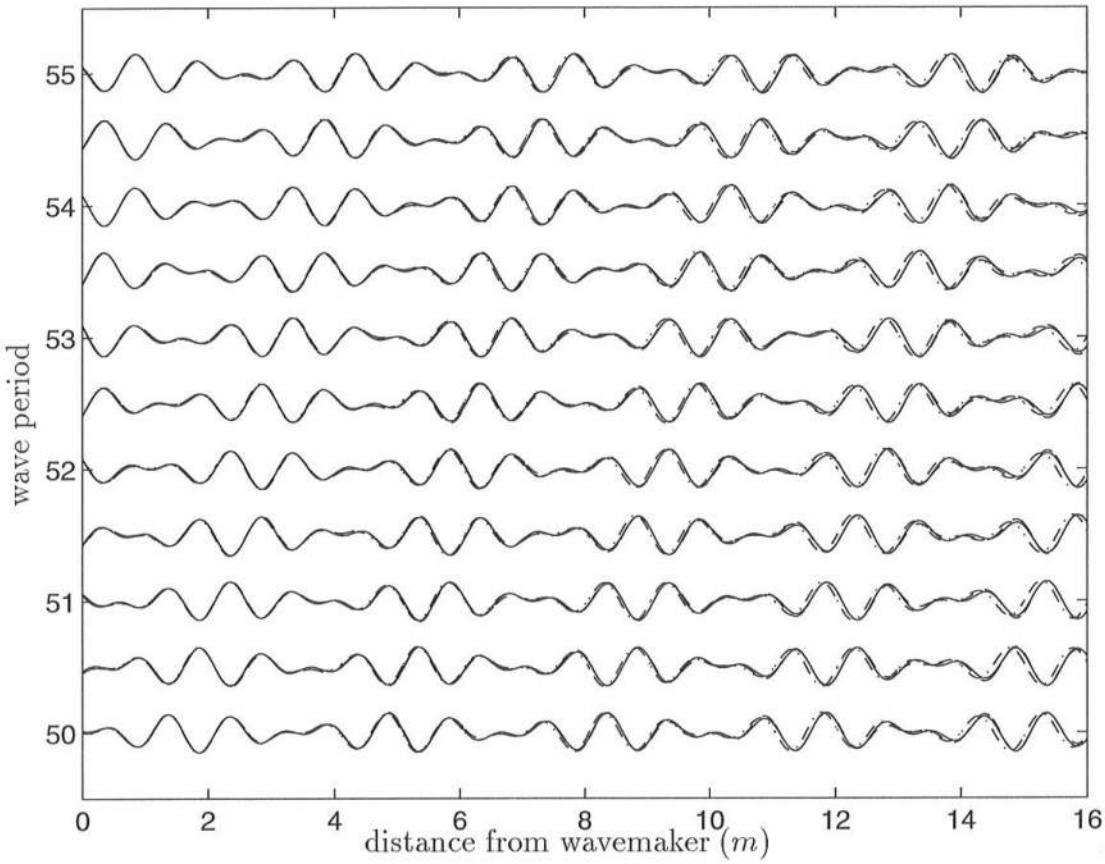

Figure 3.11: Water surface elevations for $\bar{k}h = 2\pi$, $\Delta k/\bar{k} = 0.15$ (solid line: exact solution, dashed line: new model (3.14), dash-dotted line: Kubo et al.'s model)

computational domain is 150 m. We use equation (3.30) to absorb the incident wave energy. It is determined that $\Delta t = T/80$ s and $\Delta x = L/66.67$ m. Figure 3.13 shows the water surface elevations from $t = 40T$ to $t = 45T$ with a half wave period. The solid lines are exact solutions of equation (2.44), dashed lines are results from the new equation (3.14), and the dash-dotted lines are results from Kubo et al.'s equation (2.7). Both the new model and Kubo et al.'s model yield very accurate solutions. Figure 3.14 shows the propagation of the wave phase and wave groups for the new model (3.14) from $t = 40T$ to $t = 50T$.

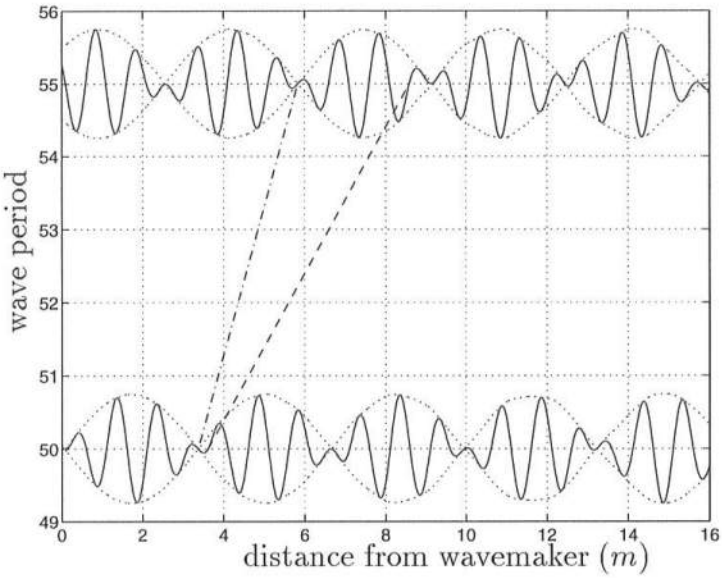

Figure 3.12: Propagation of wave phase and wave groups for $\bar{k}h = 2\pi$, $\Delta k/\bar{k} = 0.15$, new model (3.14) (dashed line: wave phase, dash-dotted line: wave groups)

Third, we test the two models for shallow water ($\bar{k}h = 0.05\pi$). The water depth is 1 m, the wave height is 0.15 m, the carrier wave period (T) is 12.8258 s, the carrier wavelength (L) is 40 m, and the total length of the computational domain is 800 m. We use equation (3.30) to absorb the incident wave energy. It is determined that $\Delta t = T/100$ s and $\Delta x = L/80$ m. Figure 3.15 shows the water surface elevations from $t = 30T$ to $t = 35T$ with a half wave period interval. The solid lines are exact solutions of equation (2.44), dashed lines are results from the new equation (3.14), and the dash-dotted lines are results from Radder and Dingemans' equations (2.5) and (2.6). Both the new model and Radder and Dingemans' model yield very accurate solutions. Figure 3.16 shows the propagation of the wave phase and wave groups for the new equation (3.14) from $t = 30T$ to $t = 40T$.

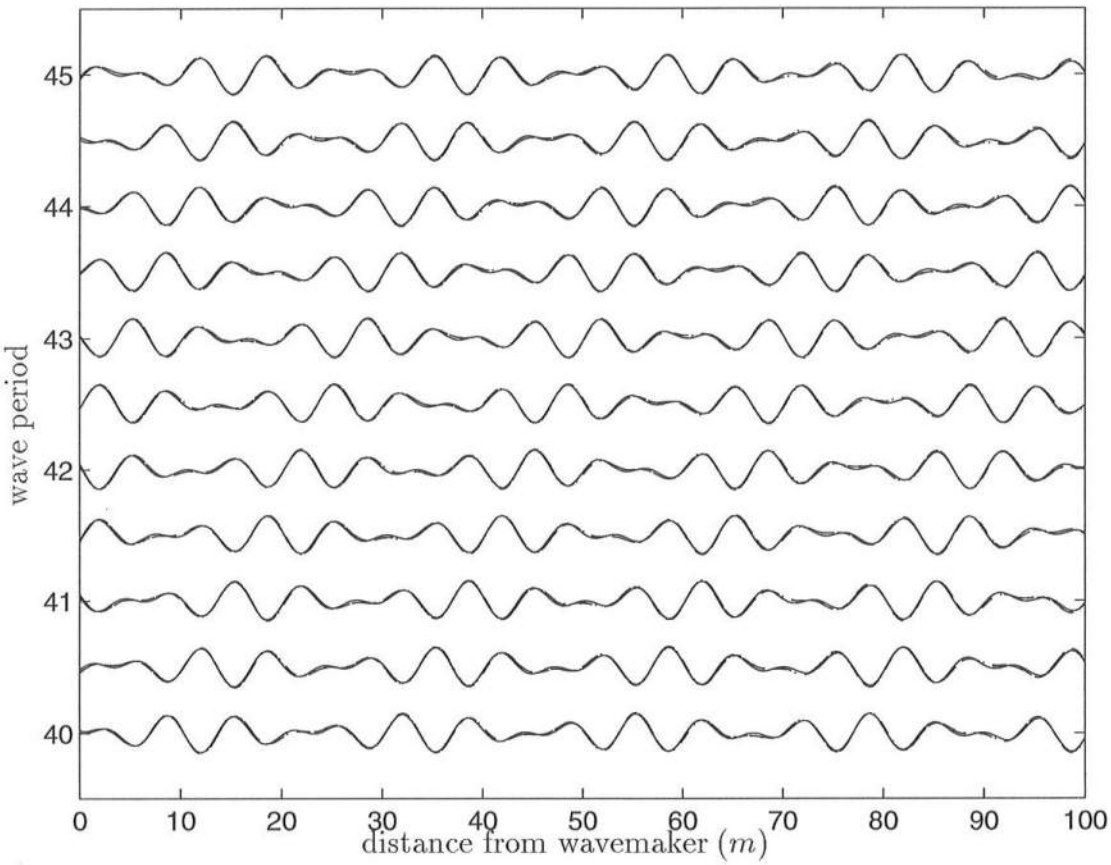

Figure 3.13: Water surface elevations for $\bar{k}h = 0.3\pi$, $\Delta k/\bar{k} = 0.15$ (solid line: exact solution, dashed line: new model (3.14), dash-dotted line: Kubo et al.'s model)

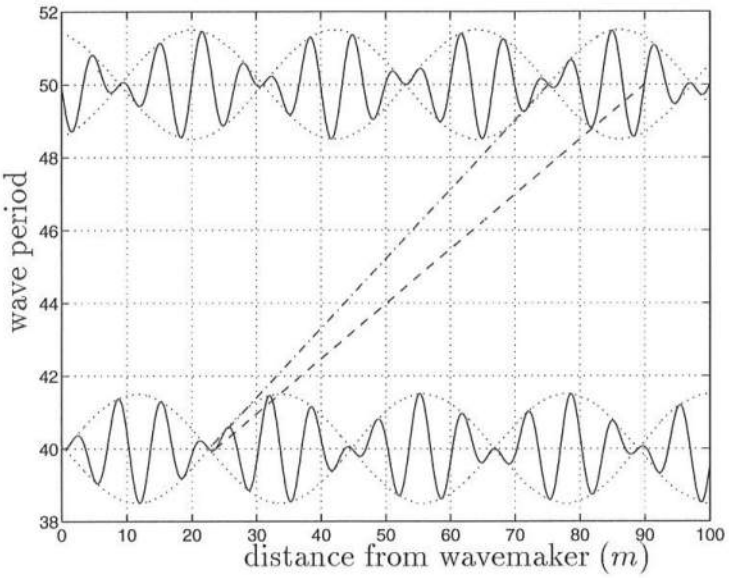

Figure 3.14: Propagation of wave phase and wave groups for $\bar{k}h = 0.3\pi$, $\Delta k/\bar{k} = 0.15$, new model (3.14) (dashed line: wave phase, dash-dotted line: wave groups)

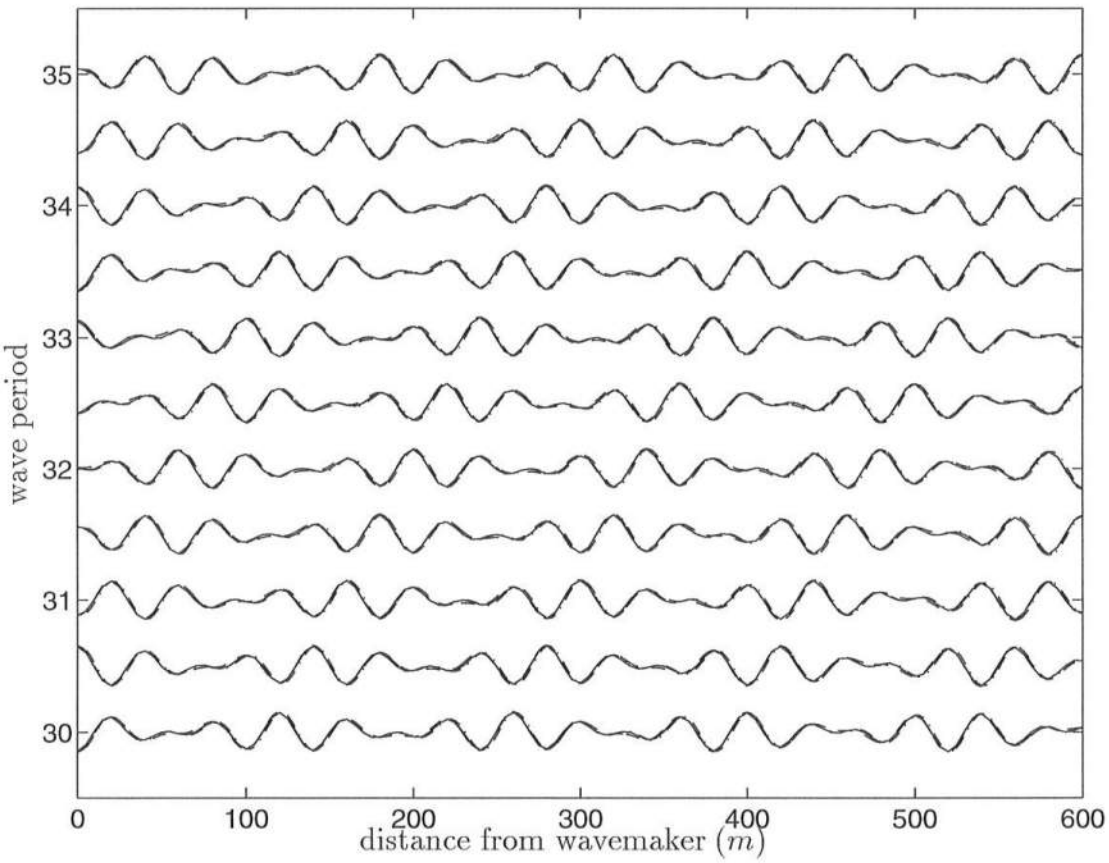

Figure 3.15: Water surface elevations for $\bar{k}h = 0.05\pi$, $\Delta k/\bar{k} = 0.15$ (solid line: exact solution, dashed line: new model (3.14), dash-dotted line: Radder and Dingemans' model)

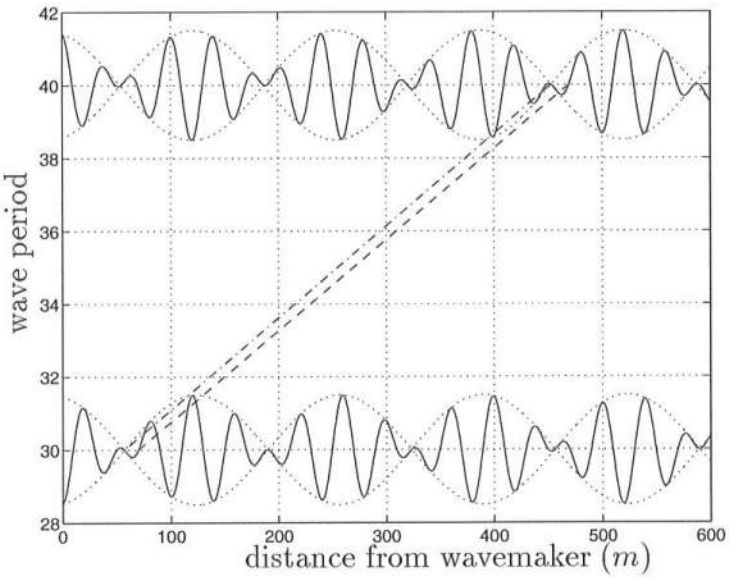

Figure 3.16: Propagation of wave phase and wave groups for $\bar{k}h = 0.05\pi$, $\Delta k/\bar{k} = 0.15$, new model (3.14) (dashed line: wave phase, dash-dotted line: wave groups)

Chapter 4

TIME-DEPENDENT MILD-SLOPE EQUATIONS FOR BREAKING WAVES

The time-dependent mild-slope equation is applicable from deep to shallow water. To extend the model into the surf zone, we need to include a model for breaking waves in the time-dependent mild-slope equation.

The energy dissipation rate with the breaking criterion given by equations (1.24) and (1.23), respectively, was used in Kubo et al.'s time-dependent mild-slope equation (1.14), resulting in

$$\nabla\cdot(\bar{C}\bar{C}_g\nabla\hat{\phi})+\bar{k}^2\bar{C}\bar{C}_g(1+if_{D_b})\hat{\phi}+i\nabla\cdot(\frac{\partial}{\partial\omega}(\bar{C}\bar{C}_g)\nabla\frac{\partial\hat{\phi}}{\partial t})+\frac{\partial}{\partial\omega}(\bar{k}^2\bar{C}\bar{C}_g)(1+if_{D_b})\frac{\partial\hat{\phi}}{\partial t}=0 \tag{4.1}$$

Equations (1.24) and (1.23) were derived semi-empirically from a uniformly sloping bottom, but were applied to a non-uniformly sloping bottom, assuming that the bottom at each point is locally uniform.

Dally et al. (1985) found, from Horikawa and Kuo's (1966) experimental data, that the wave height of the breaking wave attenuates until it reaches a stable wave height, which lies between 0.35 and 0.40 times the water depth. We use the idea of wave recovery in our model, in order to model the effects of wave breaking in waves propagating over bars or other isolated bathymetric features.

In the following section, we develop a time-dependent mild-slope equation model for breaking waves by constructing a model for the head loss based on a bore analogy, and including it in the time-dependent mild-slope equations. The breaking model would be applicable for a non-uniform bottom slope and would show the propagation of the breaking waves with a decay in wave height until stable condition is reached. We suggest a smoothing method in order to get stable model results. Without smoothing, we would get sufficient reflection due to the sudden increase of dissipation rates at the breaking point and also we would get numerical discontinuities in the solution due to the rise and decay of energy dissipation rates from wave breaking and shoaling, respectively.

4.1 Derivation of a Model for Breaking Waves

In a hydraulic jump, the head loss can be estimated from continuity, momentum, and energy equations for points on the water surface in a steady state:

$$h_L = \frac{(h_2 - h_1)^3}{4h_1 h_2} \tag{4.2}$$

where h_1 and h_2 are water depths before and after the hydraulic jump, respectively. Considering the geometry of a hydraulic jump, we write the upstream and downstream water depths h_1 and h_2 as $h_1 \simeq (h - |\eta|)$ and $h_2 \simeq (h + |\eta|)$ where h is the still water depth and $|\eta|$ is the wave amplitude (see Figure 4.1). The head loss caused by wave breaking can be estimated as

$$h_L \simeq \frac{\{(h + |\eta|) - (h - |\eta|)\}^3}{4(h + |\eta|)(h - |\eta|)} = 2|\eta| \frac{(\frac{|\eta|}{h})^2}{1 - (\frac{|\eta|}{h})^2} \tag{4.3}$$

If the head loss caused by wave breaking is included in the linear dynamic free surface boundary condition (2.6), we obtain the following equation

$$\frac{\partial \tilde{\phi}}{\partial t} = -g\eta - D_b \tilde{\phi} \tag{4.4}$$

where the energy dissipation rate D_b is related to the head loss by

$$D_b = \frac{gh_L}{|\tilde{\phi}|} = 2\gamma\bar{\omega}\frac{(\frac{|\eta|}{h})^2}{1-(\frac{|\eta|}{h})^2} \tag{4.5}$$

where we use the relation

$$\frac{|\eta|}{|\tilde{\phi}|} \simeq \frac{\bar{\omega}}{g} \tag{4.6}$$

and where γ is a calibration factor of order one. The energy dissipation rate is proportional to the carrier wave frequency and is also approximately proportional to the square of wave height to water depth ratio.

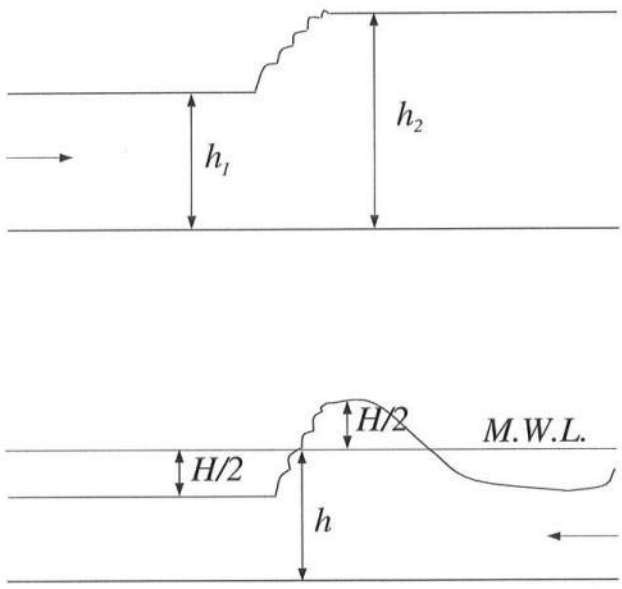

Figure 4.1: Geometric similarity between a hydraulic jump and a broken wave

So, equations (2.5) and (4.4) are a modified Radder and Dingemans' model for breaking waves. Similar to the damping coefficient D_s in sponge layer, the dissipation rate D_b for breaking waves can be included in other time-dependent

mild-slope equations. Smith and Sprinks' model can be modified by combining equations (2.5) and (4.4), yielding the following equation:

$$\frac{\partial^2\tilde{\phi}}{\partial t^2} + D_b\frac{\partial\tilde{\phi}}{\partial t} - \nabla\cdot(\bar{C}\bar{C}_g\nabla\tilde{\phi}) + (\bar{\omega}^2 - \bar{k}^2\bar{C}\bar{C}_g)\tilde{\phi} = 0 \tag{4.7}$$

where we use the relation

$$\frac{\partial\eta}{\partial t} = -\frac{1}{g}(\frac{\partial^2\tilde{\phi}}{\partial t^2} + D_b\frac{\partial\tilde{\phi}}{\partial t}) \tag{4.8}$$

For monochromatic waves, we get a modified Berkhoff's model:

$$\nabla\cdot(CC_g\nabla\hat{\phi}) + (k^2CC_g + i\omega D_b)\hat{\phi} = 0 \tag{4.9}$$

or

$$\nabla\cdot(CC_g\nabla\hat{\phi}) + k^2CC_g(1 + i\frac{D_b}{\omega n})\hat{\phi} = 0 \tag{4.10}$$

Kubo et al.'s equation (2.7) can include the energy dissipation rate as

$$\begin{aligned}\nabla\cdot(\bar{C}\bar{C}_g\nabla\hat{\phi}) + \bar{k}^2\bar{C}\bar{C}_g(1 + i\frac{D_b}{\bar{\omega}\bar{n}})\hat{\phi}\\ +i\nabla\cdot(\frac{\partial}{\partial\omega}(\bar{C}\bar{C}_g)\nabla\frac{\partial\hat{\phi}}{\partial t}) + i\frac{\partial}{\partial\omega}(\bar{k}^2\bar{C}\bar{C}_g)(1 + i\frac{D_b}{\bar{\omega}\bar{n}})\frac{\partial\hat{\phi}}{\partial t} = 0\end{aligned} \tag{4.11}$$

The new time-dependent mild-slope equation (3.14) can include the energy dissipation rate as

$$\begin{aligned}\frac{\partial}{\partial x}(\bar{C}\bar{C}_g\frac{\partial\hat{\phi}}{\partial x}) + (\bar{k}^2\bar{C}\bar{C}_g + i\bar{\omega}D_b)\hat{\phi} + i\frac{\partial}{\partial x}(\frac{\partial}{\partial\omega}(\bar{C}\bar{C}_g)\frac{\partial^2\hat{\phi}}{\partial x\partial t})\\ +i(\frac{\partial}{\partial\omega}(\bar{k}^2\bar{C}\bar{C}_g) + iD_b)\frac{\partial\hat{\phi}}{\partial t} + (\beta_3 + i\frac{1}{4})\frac{\partial^2\tilde{\phi}}{\partial t^2} = 0\end{aligned} \tag{4.12}$$

In Appendix A, we develop parabolic approximations of mild-slope equations for both monochromatic and random waves.

McCowan (1894) suggested the breaking criterion for a solitary wave in shallow water as

$$(\frac{H}{h})_b = 0.78 \tag{4.13}$$

and Miche (1944) suggested the breaking criterion for progressive waves in any depth of water as

$$(H/L)_b = 0.142 \tanh(kh) \tag{4.14}$$

which yields the limiting value as $(H/h)_b \simeq 0.88$ in shallow water. Battjes and Janssen (1978) suggested a modified version of equation (4.14) as

$$H_b = 0.88 k^{-1} \tanh(\delta kh/0.88) \tag{4.15}$$

where they use the linear dispersion relation for wavenumber k, and δ is a slightly adjustable coefficient in order to allow the effects of beach slope and to include the transformation of random waves. Weggel (1972) suggested an empirical breaking criterion as

$$(\frac{H}{h})_b = b(s) - a(s)\frac{H_b}{T^2} \tag{4.16}$$

where $a(s)$ and $b(s)$ are functions of the beach slope s given by

$$a(s) = 1.36(1 - e^{-19s}) \quad (sec^2/ft) \tag{4.17}$$

$$\frac{1}{b(s)} = 0.64(1 + e^{-19.5s}) \tag{4.18}$$

We specify the breaking criterion in terms of the wave height to water depth ratio, $(H/h)_b$. We do not fix the values of $(H/h)_b$ for different wave conditions but adjust the values to fit the experimental data. If there are no experimental data, we can use the breaking criteria suggested either by Battjes and Janssen (equation (4.15)) or by Weggel (equation (4.16)).

The recovery criterion is determined in terms of wave height to water depth ratio, $(H/h)_r$, which was found to be 0.35 to 0.4 in the experimental data from Horikawa and Kuo (1965). We adjust the values of the recovery criterion to fit the experimental data. If there are no experimental data, we fix the value of the recovery criterion as 0.35.

The energy dissipation rate depends on whether the wave is locally breaking or non-breaking. Even if the wave height to water depth ratio is locally below the breaking criterion, wave breaking still continues if the wave is already broken and the wave height to water depth ratio is above the recovery criterion. The breaking waves can be traced by finding the phase velocities in x and y directions as

$$\begin{aligned} C_x &= \frac{\bar{\omega}}{\bar{k}\cos\theta} \\ C_y &= \frac{\bar{\omega}}{\bar{k}\sin\theta} \end{aligned} \tag{4.19}$$

The wave propagation direction can be found by the angle θ counterclockwise from the x axis which is given by

$$\theta = \begin{cases} +\arctan(\frac{\frac{\partial\eta}{\partial y}}{\frac{\partial\eta}{\partial x}}); & \text{propagating in positive } x \text{ direction} \\ \\ -\arctan(\frac{\frac{\partial\eta}{\partial y}}{\frac{\partial\eta}{\partial x}}); & \text{propagating in negative } x \text{ direction} \end{cases} \tag{4.20}$$

At time $t = n\Delta t$, the breaking wave located at $(x, y) = (i\Delta x, j\Delta y)$ propagates with wave speed $\bar{\omega}/\bar{k}$ and the wave direction θ, so at the next time $t = (n+1)\Delta t$ the wave would be located at $(x, y) = (i\Delta x + \frac{\bar{\omega}}{\bar{k}\cos\theta}\Delta t, j\Delta y + \frac{\bar{\omega}}{\bar{k}\sin\theta}\Delta t)$.

For random breaking waves, we separate the whole frequency spectrum into several components with narrow bandwidths. At each time, we compute the water surface elevations of each component. We add all the water surface elevations of each component to get the total wave height. If it is found that the wave height to water depth ratio is above the breaking criterion at some point, we assume that wave breaking occurs at that point, and the energy dissipation rates D_b are computed by using the peak frequency ω_p. The propagation directions and the velocities of the breaking waves are computed at each frequency component to trace the breaking waves. If the wave height to water depth ratio drops below the recovery criterion, the wave breaking stops and no energy dissipation would occur.

4.2 Smoothing Energy Dissipation Rate

The sudden increase of the energy dissipation rate at the breaking point causes considerable reflections outside the surf zone. There are numerical discontinuities in the solution because of two opposing factors: the decrease of the energy dissipation rate due to wave breaking and the increase of the energy dissipation rate due to shoaling. As depth decreases, the wave height increases, and the wave height to water depth ratio increases by the shoaling effect. Therefore, the energy dissipation rate defined by equation (4.5) increases as depth decreases. So, we need to smooth the energy dissipation rate by averaging several adjacent point values with different weights to get a stable solution.

We use a smoothing method of 3-point averaging (Shapiro, 1970). Let $Z = Z(x)$, $-\infty < x < \infty$, and $Z_i = Z(x_i)$ for discrete values of $x_i = i\Delta x$ where i is an integer. We define a simple smoothing element:

$$\bar{Z}_i = (1 - S)Z_i + S(Z_{i-1} + Z_{i+1})/2 = Z_i + \frac{S}{2}(Z_{i-1} + Z_{i+1} - 2Z_i) \qquad (4.21)$$

where S is a smoothing element. It is found that the response function, the ratio of the smoothed to unsmoothed amplitude, is

$$R(k) = 1 - 2S \sin^2 k\Delta x/2 \qquad (4.22)$$

With $S = 1/2$, the waves of length $L = 2\Delta x$ are completely eliminated, and all features longer than $2\Delta x$ are damped except infinitely long features. Successive application of n smoothing operators of the form of equation (4.21), with smoothing elements $S = 1/2$, results in a ratio of smoothed amplitude to unsmoothed amplitude given by

$$R(k)^n = (1 - 2S \sin^2 k\Delta x/2)^n \qquad (4.23)$$

We test the smoothing method, equation (4.23), for a case with a delta function with a magnitude of one. The results before and after smoothing with n

= 5,10, and 15 are shown in Figure 4.2 (a), from which we find that the original delta function decreases and spreads out with area being conserved as the value of n increases. The response functions, the spectral densities, are shown in Figure 4.2 (b) from which we find that more damping happens and that the damping extends toward waves of lower frequencies as the value of n increases.

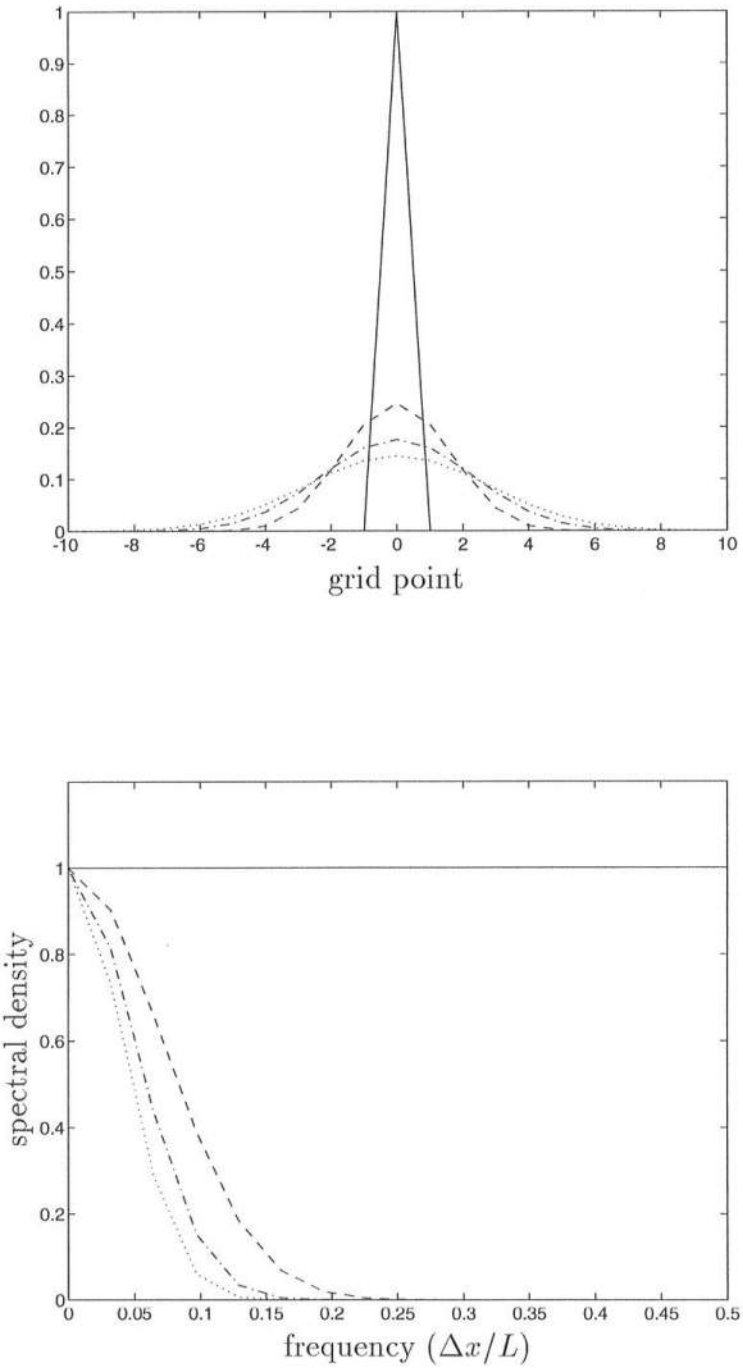

Figure 4.2: One-dimensional simple smoothing (solid line: $n = 0$, dashed line: $n = 5$, dash-dotted line: $n = 10$, dotted line: n =15) (a) results, (b) spectral densities

We test the smoothing for a case with supporting experimental data. Horikawa and Kuo (1965) conducted experiments for breaking waves shoaling over a 1/65 sloping bottom. Here we test for a case with a wave period of 1.6 s, and wave height to water depth ratio in deep water 0.065. The modified Radder and Dingemans' model (2.5) and (5.12) are used to get solutions. Equation (5.12) is a modified equation to include the energy dissipation rates caused by wave breaking and at sponge layer. The grid size is $\Delta x = 0.2\ m$ and time step is $\Delta t = 0.02$ s which give a convergent solution. Breaking criterion is $(H/h)_b = 0.78$ and the factor of wave breaking is $\gamma = 0.4$. Figure 4.3 shows the wave heights at $t = 60T$ after smoothing with different values of $n = 0, 5, 10$, and 15. This shows that once smoothing is done, the effect of the wave height decay does not change and that a larger number of successive smoothings are required to get stable solutions. We select the number of succesive smoothings $n = 15$ to smooth the dissipation rate for the one-dimensional case of wave breaking. The number of successive smoothings $n = 15$ uses 31 point values for smoothing a value. The weights of the point values w for $n = 15$ when applied at point i are given as

$$
\begin{aligned}
w_i &= 0.144464 \\
w_{i\pm1} &= 0.135435 \\
w_{i\pm2} &= 0.111535 \\
w_{i\pm3} &= 8.05531 \times 10^{-2} \\
w_{i\pm4} &= 5.08756 \times 10^{-2} \\
w_{i\pm5} &= 2.79816 \times 10^{-2} \\
w_{i\pm6} &= 1.33246 \times 10^{-2} \\
w_{i\pm7} &= 5.45096 \times 10^{-3} \\
w_{i\pm8} &= 1.89599 \times 10^{-3} \\
w_{i\pm9} &= 5.52996 \times 10^{-4}
\end{aligned}
$$

$$
\begin{aligned}
w_{i\pm10} &= 1.32719 \times 10^{-4} \\
w_{i\pm11} &= 2.55229 \times 10^{-5} \\
w_{i\pm12} &= 3.78117 \times 10^{-6} \\
w_{i\pm13} &= 4.05125 \times 10^{-7} \\
w_{i\pm14} &= 2.79397 \times 10^{-8} \\
w_{i\pm15} &= 9.31323 \times 10^{-10}
\end{aligned} \tag{4.24}
$$

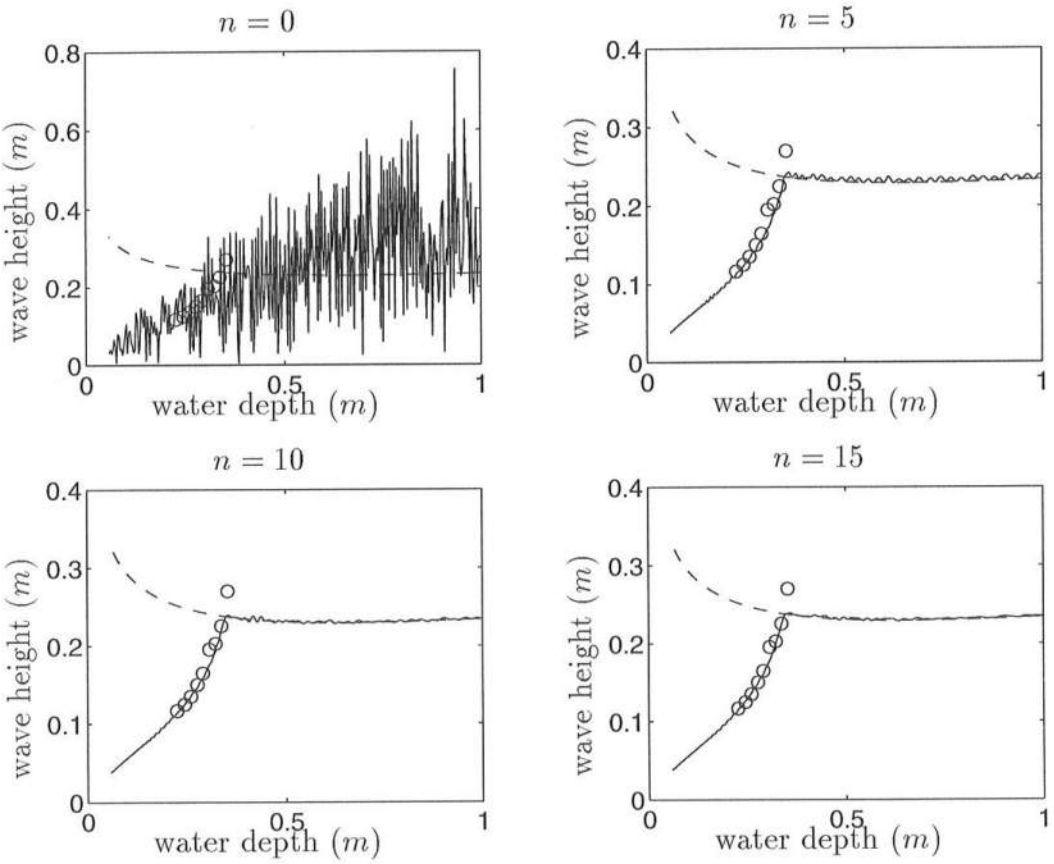

Figure 4.3: Wave heights with different numbers of successive applications $n = 0, 5, 10$, and 15 (○: measured data, solid line: computed results, dashed line: results from shoaling coefficient)

The smoothing, equation (4.21), can be applied in two dimensions as

$$\begin{aligned}\overline{Z_{i,j}}^{i,j} &= \overline{(\overline{Z}^{i}_{i,j})}^{j} \\ &= Z_{i,j} + \frac{S}{4}(Z_{i-1,j} + Z_{i+1,j} + Z_{i,j-1} + Z_{i,j+1} - 4Z_{i,j}) \\ &\quad + \frac{S^2}{4}(Z_{i-1,j+1} + Z_{i+1,j+1} + Z_{i+1,j-1} + Z_{i-1,j-1} - 4Z_{i,j}) \qquad (4.25)\end{aligned}$$

The ratio of the smoothed to unsmoothed amplitudes $R(k,h)$ corresponding to the 9-point operator, equation (4.25), is

$$R(k,h) = (1 - 2S\sin^2 k\Delta x/2)(1 - 2S\sin^2 h\Delta y/2) \qquad (4.26)$$

Since each of the two smoothers on the right of equation (4.26) is of the same form as equation (4.21), all the development applicable to one-dimensional smoothing is independently applicable to each of the smoothing operators in equation (4.26). Successive application of n smoothing operators of the form of equation (4.26) with smoothing elements $S = 1/2$ results in a ratio of smoothed amplitude to unsmoothed amplitude given by

$$R(k,h)^n = \{(1 - 2S\sin^2 k\Delta x/2)(1 - 2S\sin^2 h\Delta y/2)\}^n \qquad (4.27)$$

We test the smoothing method, equation (4.27), for a case with a delta function with a magnitude of one. The results after smoothing with $n = 0, 1, 2,$ and 3 are shown in Figure 4.4, from which we find that the original delta function decreases and spreads out with equal area as n increases. The response functions for results along a straight line passing through the center point are shown in Figure 4.5, from which we find that as n increases more damping happens and the damping extends toward waves of lower frequencies. It is found that the damping effect for two-dimensional smoothing is much higher than for one-dimensional smoothing. We select the number of successive smoothings, $n = 2$, for smoothing the dissipation rate for two-dimensional breaking waves. The case with $n = 2$ uses

25 point values to smooth a value. The response at the point of two-dimensional smoothing is 0.140, which can be compared to the reponse at the point of one-dimensional smoothing which is 0.144. In Figure 4.5, the response function drops at $\Delta x/L = 0$ because the considered point values are only along a straight line passing the point of smoothing; other point values are not considered, so the total area decreases. The weights of the point values w for $n = 2$ when applied at point (i, j) are given as

$$\begin{aligned}
w_{i,j} &= 0.140625 \\
w_{i\pm1,j} &= 0.937500 \times 10^{-1} \\
w_{i,j\pm1} &= 0.937500 \times 10^{-1} \\
w_{i\pm1,j\pm1} &= 0.625000 \times 10^{-1} \\
w_{i\pm2,j} &= 0.234375 \times 10^{-1} \\
w_{i,j\pm2} &= 0.234375 \times 10^{-1} \\
w_{i\pm1,j\pm2} &= 0.156250 \times 10^{-1} \\
w_{i\pm2,j\pm1} &= 0.156250 \times 10^{-1} \\
w_{i\pm2,j\pm2} &= 0.390625 \times 10^{-2}
\end{aligned} \tag{4.28}$$

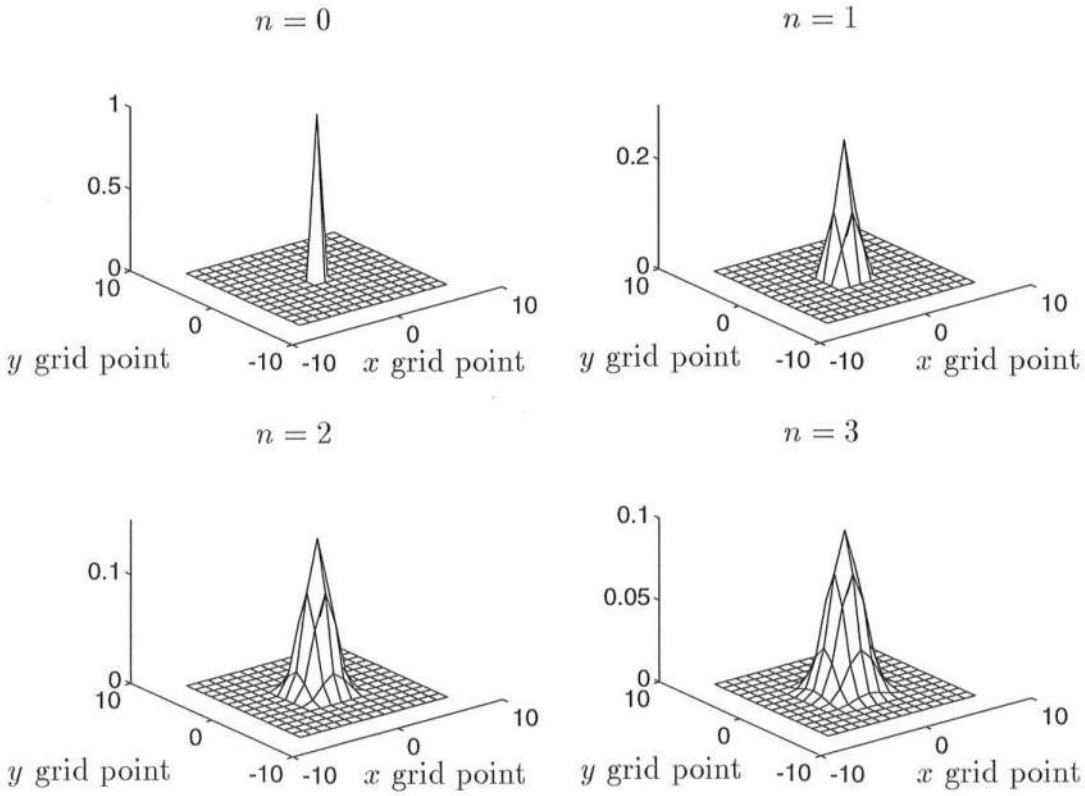

Figure 4.4: Results after two-dimensional simple smoothing with $n = 0, 1, 2,$ and 3

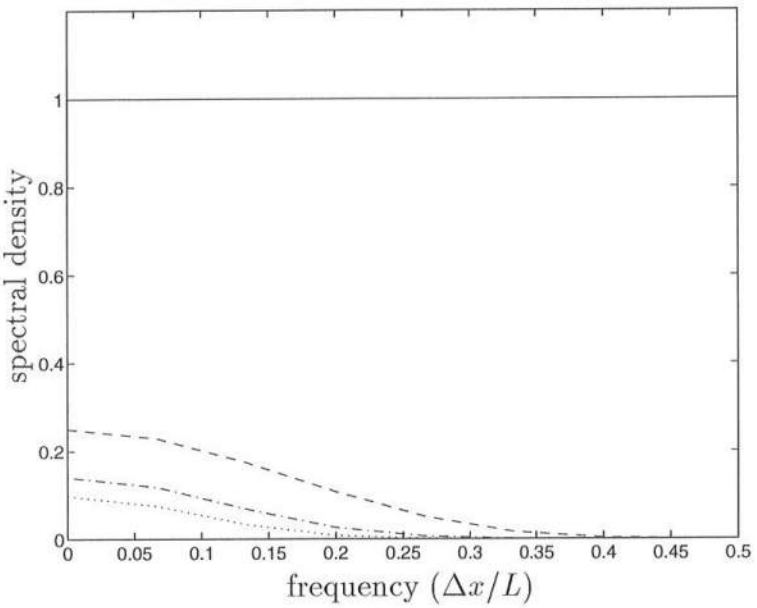

Figure 4.5: Spectral densities after two-dimensional simple smoothing with $n = 0, 1, 2$, and 3 (solid line: $n = 0$, dashed line: $n = 1$, dash-dotted line: $n = 2$, dotted line: $n = 3$)

Chapter 5

APPLICATIONS TO SEVERAL CASES

We use the Radder and Dingemans' model to verify the wide applicability of the time-dependent mild-slope equations from deep to shallow water, for one-dimensional and two-dimensional, monochromatic and random, non-breaking and breaking waves. In section 1, we specify boundary conditions and mention the dicretization method to be used for applications in section 2 and section 3. In section 2, we use the Radder and Dingemans' model applied to non-breaking waves for Berkhoff et al.'s shoal experiment (two-dimensional monochromatic waves) and Vincent and Briggs' shoal experiment (two-dimensional monochromatic and random waves). In section 3, we use a modified Radder and Dingemans' model applied to breaking waves for the Horikawa and Kuo's horizontal and sloping bottom experiment (one-dimensional monochromatic waves), the Mase and Kirby's sloping beach experiment (one-dimensional random waves), and the Vincent and Briggs' shoal experiment (two-dimensional monochromatic and random waves).

5.1 Specification of Boundary Conditions and Discretization

At the wavemaker boundary $x = 0$ and the free surface $z = 0$, we specify the particle velocities u in the x direction. The specified particle velocities are complex valued to compute the wave heights easily by taking the absolute value of the complex valued water surface elevations η.

For random wave trains, if we know the Fourier transform of the original real valued signal $\zeta(t)$, then we may construct the Fourier transform of the causal signal $\eta(t)$. A causal function is a complex function which is entirely known if its real or imaginary parts are known. The spectral densities of complex valued η can be computed by the spectral densities of real valued ζ and are given by

$$F_\eta = \begin{cases} 2F_\zeta; & \omega > 0 \\ F_\zeta; & \omega = 0 \\ 0; & \omega < 0 \end{cases} \tag{5.1}$$

Mase and Kirby (1992) conducted experiments for one-dimensional random waves of Pierson-Moskowitz spectrum shoaling over a 1/20 sloping beach. We generate complex valued particle velocities u for case 1, which yields plunging breakers in the surf zone, by subdividing the whole spectrum into 6 frequency components with equal bandwidths and inverse Fourier transforming each frequency component. Figure 5.1 shows generated particle velocities u at the wavemaker boundary at each frequency component. Here the solid line represents real part of u and dashed line represents imaginary part of u.

For a two-dimensional random wave train, the water surface elevation may be written as

$$\eta(x,y,t) = \sum_{l=1}^{L} \sum_{m=1}^{M} \frac{a_{lm}}{2} e^{i\{k_l \cos\theta_m x + k_l \sin\theta_m y - 2\pi f_l t + \psi_{lm}\}} + c.c. \tag{5.2}$$

where a_{lm} is wave amplitude, f_l is wave frequency, θ_m is wave direction, ψ_{lm} is random phase independent of frequency and direction, and *c.c.* represents the complex conjugate. Instead of using a discrete set of wave angles, we use here a discretization of the longshore wavenumber spectrum. The longshore wavenumber λ_m is defined as

$$\lambda_m = k_l \sin\theta_m \tag{5.3}$$

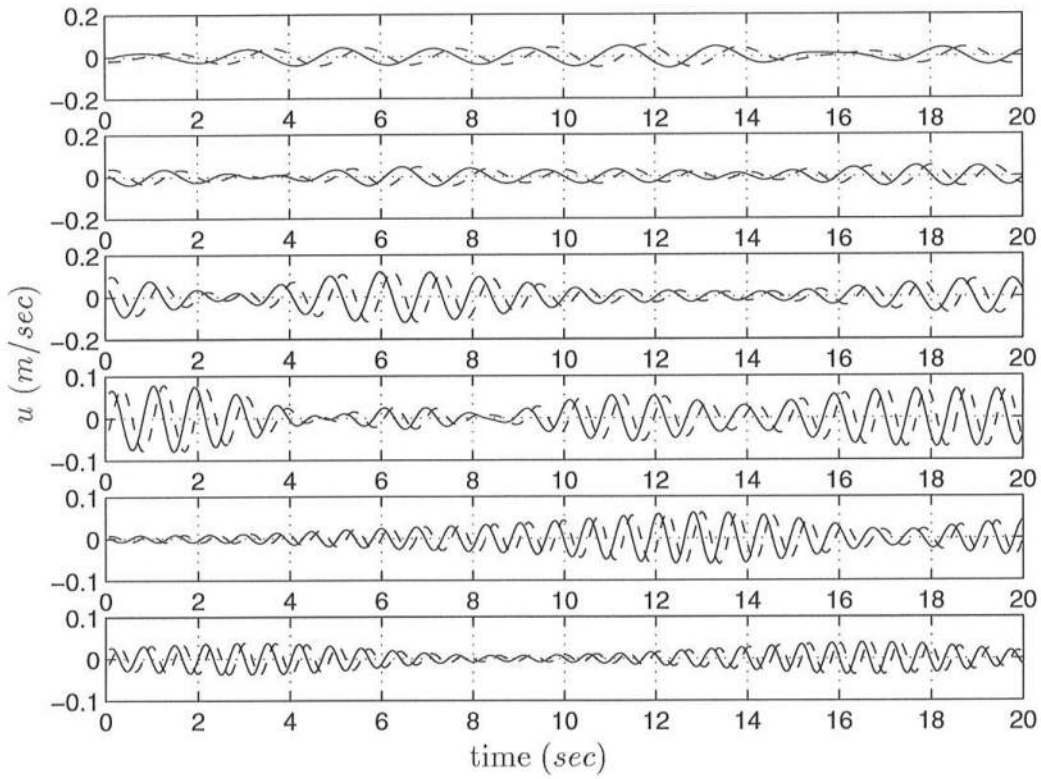

Figure 5.1: Generated particle velocities $u(t)$ at wavemaker boundary $z = 0, x = 0$ for Mase and Kirby's (1992) case 1 with 6 frequency components (solid line: real part, dashed line: imaginary part) (a) first frequency component, (b) second frequency component, (c) third frequency component, (d) fourth frequency component, (e) fifth frequency component, (d) sixth frequency component

which determines the wave direction θ_m at each frequency. At the upwave boundary ($x = 0$), the water surface elevation is given by

$$\eta(y,t) = \sum_{l=1}^{L} \sum_{m=1}^{M} \frac{a_{lm}}{2} e^{i\{\lambda_m y - 2\pi f_l t + \psi_{lm}\}} + c.c. \tag{5.4}$$

For the given frequency f_l and longshore wavenumber λ_m, we get the amplitude of the water surface elevation

$$a_{lm} = \sqrt{2S_l(f)\Delta f \frac{S_m(\lambda)}{2\pi}\Delta\lambda} \tag{5.5}$$

where $S_l(f)$ is the spectral density dependent on the frequency f and $S_m(\lambda)$ is the directional spreading function dependent on the longshore wavenumber λ. We can get $S_m(\lambda)$ from $D_m(\theta)$ (which is the spreading function dependent on the direction θ) by the condition

$$\int_{-\frac{\pi}{2}}^{\frac{\pi}{2}} D(\theta)d\theta = \int_{-k}^{k} \frac{S(\lambda)}{2\pi}d\lambda = 1, \tag{5.6}$$

and so,

$$\frac{S(\lambda)}{2\pi} = D(\theta)\frac{d\theta}{d\lambda} = \frac{D(\theta)}{k\cos\theta} \tag{5.7}$$

The particle velocity in the x direction at $x, z = 0$ can be obtained from the velocity potential and is given by

$$u = \sum_{l=1}^{L}\sum_{m=1}^{M} \frac{A_{lm}}{2} e^{i\{\lambda_m y - 2\pi f_l t + \psi_{lm}\}} + c.c. \tag{5.8}$$

where the amplitude A_{lm} is given by

$$A_{lm} = a_{lm}\frac{g\sqrt{k_l^2 - \lambda_m^2}}{2\pi f_l} \tag{5.9}$$

When the spectral density $S(f)$ and the directional spreading function $D(\theta)$ are given, we can get the amplitude of the particle velocity A_{lm}. Using a 2-dimensional inverse FFT from the frequency and longshore wavenumber domain to the time and y space domain, we can generate the velocity u.

Vincent and Briggs conducted experiments for two-dimensional random waves using TMA spectrum and directional spreading function as input conditions. Here, we consider the case N5 which produces breaking waves of narrow-band spreading. We cut off 2 percent lower and upper frequency components and subdivide the remaining spectrum into 3 components with equal bandwidths. We compute the spectral densities of the particle velocity A_{lm} from given TMA spectrum $S(f)$ and directional function $D(\theta)$ and we generate particle velocities by inverse Fourier transforming the spectral densities. Figure 5.2 shows the generated particle velocities at $(x, y) = (0\ ft,\ 45\ ft)$.

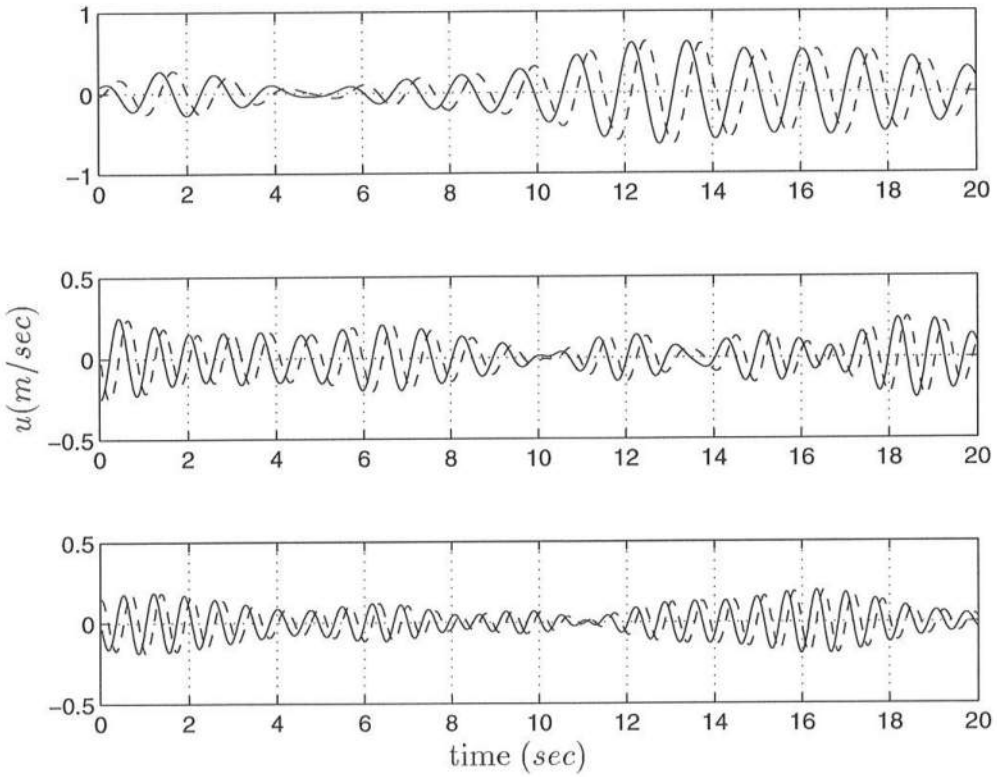

Figure 5.2: Generated particle velocities $u(t)$ at wavemaker boundary $z = 0, x = 0, y = 45\ ft$ for Vincent and Briggs' (1989) case N5 with 3 frequency components (solid line: real part, dashed line: imaginary part) (a) first frequency component, (b) second frequency component, (c) third frequency component

We specify reflective boundary conditions at side walls for two-dimensional problems as

$$\frac{\partial \tilde{\phi}}{\partial y} = 0$$

$$\frac{\partial \eta}{\partial y} = 0 \tag{5.10}$$

In order to dissipate wave energy at downwave boundaries, we use a wave damping layer at the downwave boundary. Equation (2.6) is modified to, for

non-breaking waves,

$$\frac{\partial \tilde{\phi}}{\partial t} = -g\eta - D_s\tilde{\phi} = G(\tilde{\phi}, \eta) \tag{5.11}$$

and, for breaking waves,

$$\frac{\partial \tilde{\phi}}{\partial t} = -g\eta - (D_b + D_s)\tilde{\phi} = G(\tilde{\phi}, \eta) \tag{5.12}$$

where D_s is the energy dissipation rate in the sponge layer described by equation (2.52) and D_b is the energy dissipation rate for breaking waves described by equation (4.5).

A fourth order Adams-Bashforth-Moulton predictor-corrector method is used to discretize (2.5) and (5.11) (non-breaking waves) or (2.5) and (5.12) (breaking waves) in time. In order to discretize terms with spatial differentiation we use the fourth order discretization:

$$\left[\frac{\partial f}{\partial x}\right]_i = \begin{cases} \frac{1}{12\Delta x}(-3f_{i-1} - 10f_i + 18f_{i+1} - 6f_{i+2} + f_{i+3}), & i\text{=}2 \\ \frac{1}{12\Delta x}(f_{i-2} - 8f_{i-1} + 8f_{i+1} - f_{i+2}), & i\text{=}3,4,\cdots,\text{I-3,I-2} \\ \frac{1}{12\Delta x}(-3f_{i+1} - 10f_i + 18f_{i-1} - 6f_{i-2} + f_{i-3}), & i\text{=I-1} \end{cases}$$

$$\left[\frac{\partial f}{\partial y}\right]_j = \begin{cases} \frac{1}{12\Delta y}(-3f_{j-1} - 10f_j + 18f_{j+1} - 6f_{j+2} + f_{j+3}), & j\text{=}2 \\ \frac{1}{12\Delta y}(f_{j-2} - 8f_{j-1} + 8f_{j+1} - f_{j+2}), & j\text{=}3,4,\cdots,\text{J-3,J-2} \\ \frac{1}{12\Delta y}(-3f_{j+1} - 10f_j + 18f_{j-1} - 6f_{j-2} + f_{j-3}), & j\text{=J-1} \end{cases}$$

$$\left[\frac{\partial^2 f}{\partial x^2}\right]_i = \begin{cases} \frac{1}{12(\Delta x)^2}(11f_{i-1} - 20f_i + 6f_{i+1} + 4f_{i+2} - f_{i+3}), & i\text{=}2 \\ \frac{1}{12(\Delta x)^2}(-f_{i-2} + 16f_{i-1} - 30f_i + 16f_{i+1} - f_{i+2}), & i\text{=}3,4,\cdots,\text{I-3,I-2} \\ \frac{1}{12(\Delta x)^2}(11f_{i+1} - 20f_i + 6f_{i-1} + 4f_{i-2} - f_{i-3}), & i\text{=I-1} \end{cases}$$

$$\left[\frac{\partial^2 f}{\partial y^2}\right]_j = \begin{cases} \frac{1}{12(\Delta y)^2}(11f_{j-1} - 20f_j + 6f_{j+1} + 4f_{j+2} - f_{j+3}), & j\text{=}2 \\ \frac{1}{12(\Delta y)^2}(-f_{j-2} + 16f_{j-1} - 30f_j + 16f_{j+1} - f_{j+2}), & j\text{=}3,4,\cdots,\text{J-3,J-2} \\ \frac{1}{12(\Delta y)^2}(11f_{j+1} - 20f_j + 6f_{j-1} + 4f_{j-2} - f_{j-3}), & j\text{=J-1} \end{cases}$$

In the Adams-Bashforth predictor step, we have

$$\begin{aligned} \eta^{n+1} &= \eta^n + \frac{\Delta t}{24}\{55F^n - 59F^{n-1} + 37F^{n-2} - 9F^{n-3}\} \\ \tilde{\phi}^{n+1} &= \tilde{\phi}^n + \frac{\Delta t}{24}\{55G^n - 59G^{n-1} + 37G^{n-2} - 9G^{n-3}\} \end{aligned} \tag{5.13}$$

and in the Adams-Moulton corrector step, we have

$$\begin{aligned} \eta^{n+1} &= \eta^n + \frac{\Delta t}{24}\{9F^{n+1} + 19F^n - 5F^{n-1} + F^{n-2}\} \\ \tilde{\phi}^{n+1} &= \tilde{\phi}^n + \frac{\Delta t}{24}\{9G^{n+1} + 19G^n - 5G^{n-1} + G^{n-2}\} \end{aligned} \tag{5.14}$$

where the superscript n denotes the time step. If the errors between predicted and corrected values are small enough, we proceed to the next time step; otherwise, we repeat correcting until we get small errors.

5.2 Applications for Non-Breaking Waves

5.2.1 Berkhoff, Booij and Radder Shoal Experiment (Two-dimensional Monochromatic Waves)

As an example of the application of the models in two dimensions, we study the focusing of waves by a shoal, using the geometry and experimental parameters given in Berkhoff et al. (1982).

The experimental topography consists of an elliptic shoal resting on a plane sloping bottom with a slope of 1/50. The plane slope rises from a region of constant depth $h = 0.45\ m$, and the entire slope is turned at an angle of 20° to a straight wave paddle. Bottom contours are shown in Figure 5.3 along with the chosen computational domain. The offshore boundary of the computational

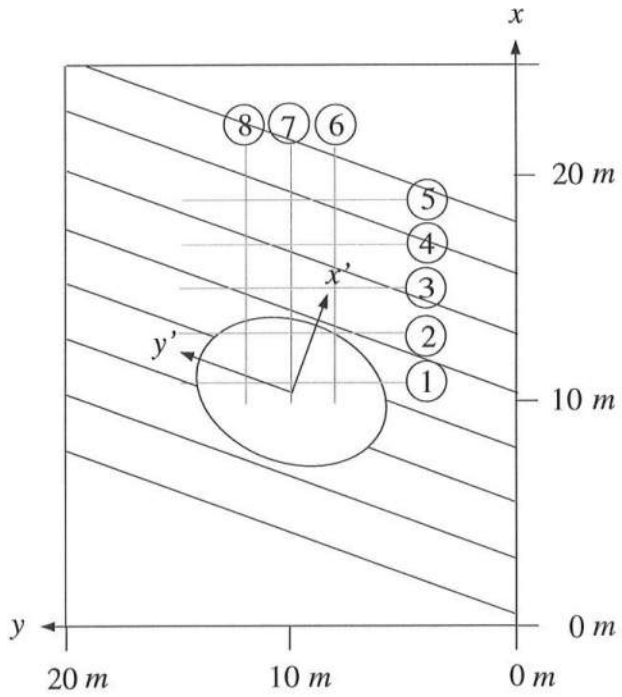

Figure 5.3: Experimental setup by Berkhoff et al. (1982)

domain is chosen so that water depth is constant along $x = 0$. We establish slope-oriented coordinates (x', y') which are related to the computational coordinates (x, y) according to:

$$\begin{aligned} x' &= (x - 10.5)\cos 20° - (y - 10)\sin 20° \\ y' &= (x - 10.5)\sin 10° + (y - 10)\cos 20° \end{aligned} \tag{5.15}$$

The origin $(x', y') = (0, 0)$ corresponds to the center of the shoal. The slope is described in meters by

$$h = \begin{cases} 0.45; & x' < -5.82 \\ 0.45 - 0.02(5.82 + x'); & x' \geq -5.82 \end{cases} \tag{5.16}$$

The boundary of the elliptic shoal is given by

$$(\frac{x'}{3})^2 + (\frac{y'}{4})^2 = 1 \tag{5.17}$$

and the depth in the shoal region is modified in meters according to

$$h = h_{slope} - 0.5\sqrt{1 - (x'/3.75)^2 - (y'/5)^2} + 0.3 \tag{5.18}$$

resulting in a depth at the center of the shoal $h(x' = 0, y' = 0) = 0.1332\ m$.

The initial condition for the wave corresponds to the uniform wave train generated at the wave paddle with an amplitude $a_0 = 0.032\ m$ and a wave period $T = 1\ s$. The incident waves are dissipated by a breaking process on a gravel beach at the shallow end. At sections 1 through 8 there are arrays of resistance type wave gages spaced 0.5 m apart which record time series of water surface elevations.

It is known from parabolic model computations (Kirby and Dalrymple, 1984) that the waves in this example are significantly affected by wave nonlinearity. Following the appendix in Kirby and Dalrymple (1984), we provide a heuristic extension to the mild-slope equation that is appropriate only for progressive Stokes waves. The resulting modification to equation (2.5) is given by

$$\frac{\partial \eta}{\partial t} = -\nabla \cdot (\frac{\bar{C}\bar{C}_g}{g}\nabla\tilde{\phi}) + \frac{(\bar{\omega}^2 - \bar{k}^2\bar{C}\bar{C}_g + \bar{\omega}\bar{C}_g K'|\eta|^2)}{g}\tilde{\phi} \tag{5.19}$$

where

$$K' = \frac{\bar{k}^3\bar{C}}{\bar{C}_g}\frac{\cosh 4\bar{k}h + 8 - 2\tanh^2 \bar{k}h}{8\sinh^4 \bar{k}h} \tag{5.20}$$

We apply both the linear (equations (2.5) and (5.11)) and nonlinear (equations (5.19) and (5.11)) model equations to the shoal described by Berkhoff et al. (1982). The data on wave amplitude was obtained over the entire vicinity of a refractive focus. The Ursell parameter remains of a reasonably small size over

the entire domain of interest, thus indicating that Stokes theory should be a valid representation of the experiment. The grid sizes are $\Delta x = \Delta y = 0.25\ m$ and $\Delta t = 1/40\ s$. We run the models until $t = 80\ s$.

Referring to Figures 5.4 and 5.5, where model results are compared to measured data along transects 1 through 8, we see that the linear model tends to overpredict maximum amplitudes in the vicinity of focused waves, where wave steepness may become large and nonlinear effects become important. In these regions the nonlinear models give better results. The nonlinear model results appear to contain some spurious amplitude modulations. These are not a manifestation of instability, and the effect may be suppressed by a suitable lagging of the nonlinear term in the numerical scheme.

When Figures 5.4 and 5.5 are compared to Figure 4 of Kirby and Dalrymple (1984) which shows both linear and nonlinear model results from parabolic approximations, the normalized wave heights are almost the same with minor differences. At section 3, the results from the nonlinear model shown in Figure 5.4 are more accurate than those from the nonlinear model shown in Figure 4 of Kirby and Dalrymple. At section 6, the results from the nonlinear model shown in Figure 4 of Kirby and Dalrymple are more accurate than those from the nonlinear model shown in Figure 5.5.

When Figures 5.4 and 5.5 are compared to Figure 4 of Panchang et al. (1991) which shows both linear and nonlinear solutions of Berkhoff's model by iteration, the nomalized wave heights are almost the same with minor differences. The similarity of our model to Panchang et al.'s model is stronger than the similarity of our model to Kirby and Dalrymple's model.

When Figures 5.4 and 5.5 are compared to Figure 7 of Dalrymple et al.

(1989) which shows both linear and nonlinear solutions for very wide-angle diffraction, the normalized wave heights are almost the same with minor differences. At section 6, the results from the nonlinear model shown in Figure 7 of Kirby and Dalrymple are more accurate than those from the nonlinear model shown in Figure 5.5.

5.2.2 Vincent and Briggs Shoal Experiment (Two-dimensional Monochromatic and Random Waves)

A further study of monochromatic and random wave propagation over a shoal has been performed by Vincent and Briggs (1989). These tests are used here as a validation of the present numerical scheme as a model for irregular wave propagation.

The tests were conducted in a 35 m (114 ft) wide by 29 m (96 ft) long directional spectral wave basin. The center of the shoal was located at coordinates $x = 6.10\ m\ (20\ ft)$, $y = 13.72\ m\ (45\ ft)$. The water surface elevations were measured using an array of 9 parallel-wire resistance-type sensors which were spaced 76 cm (2.5 ft) apart. The boundary of the shoal is defined in meters by

$$(\frac{x'}{3.0480})^2 + (\frac{y'}{3.9624})^2 = 1 \tag{5.21}$$

where x' and y' are localized coordinates centered on the shoal denoting minor and major axes, respectively. The water depth at any point in the shoal cross-section in meters is given by

$$h = 0.4572 - 0.7620\sqrt{1 - (x'/3.8100)^2 - (y'/4.9530)^2} \tag{5.22}$$

resulting in the water depth at the center of the shoal 15.24 cm.

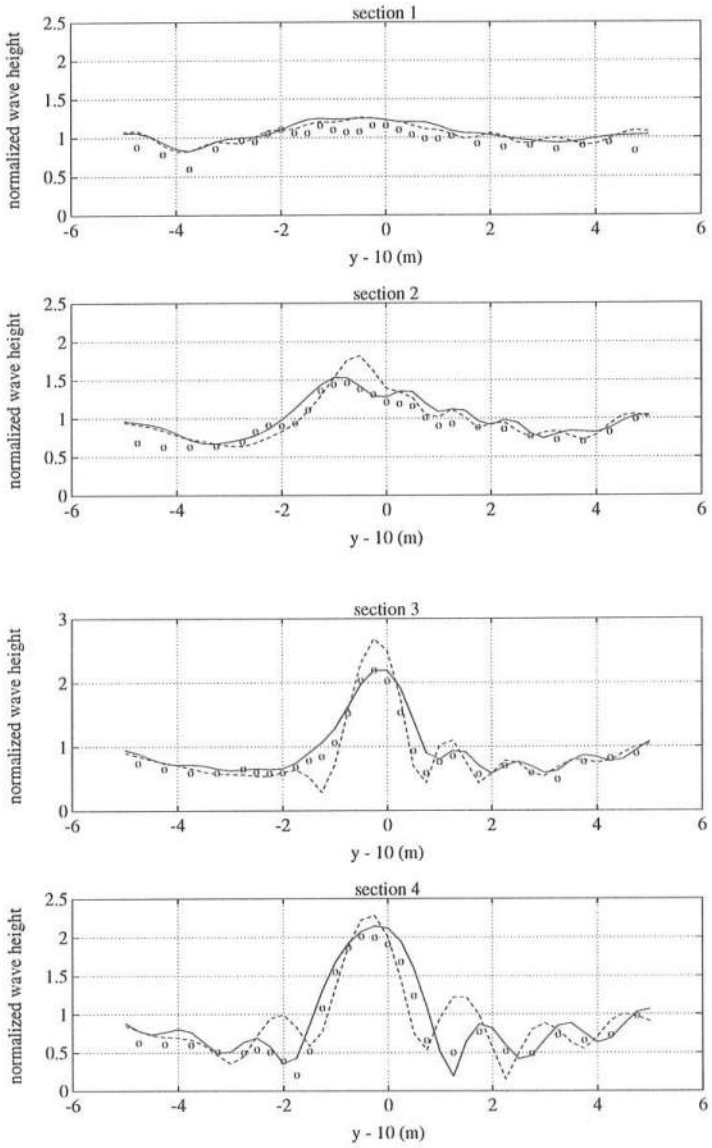

Figure 5.4: Comparison among linear model (dashed lines), nonlinear model (solid lines), and experimental data of Berkhoff et al. (1982) (section 1 - section4)

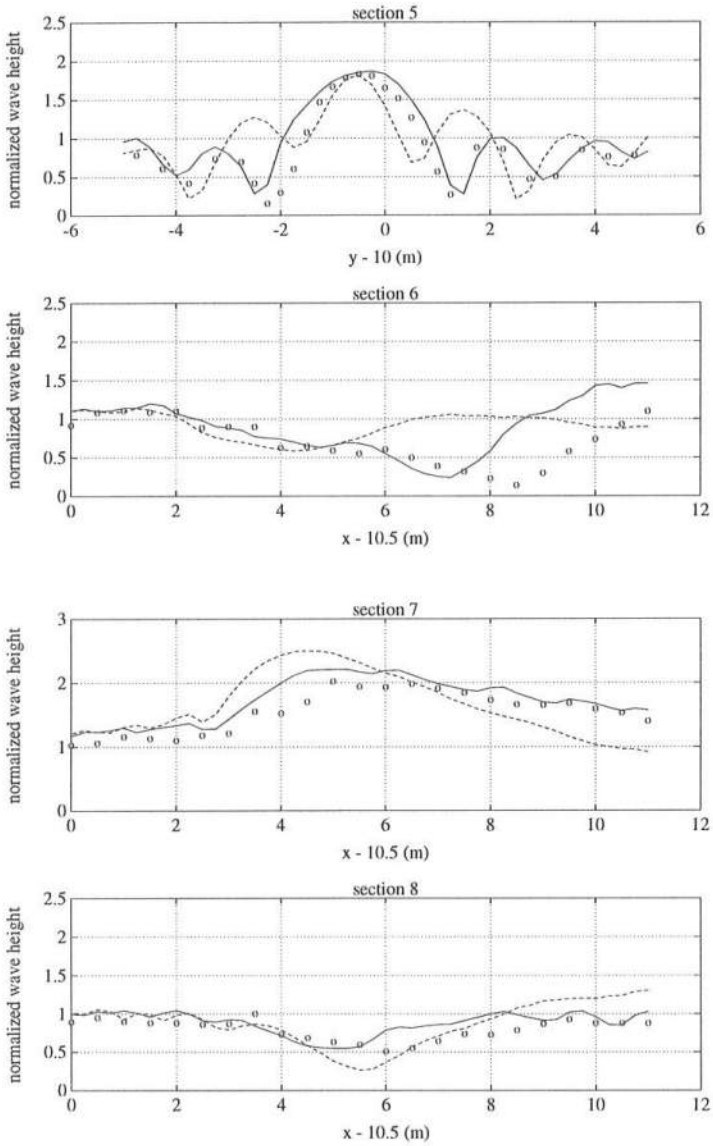

Figure 5.5: Comparison among linear model (dashed lines), nonlinear model (solid lines), and experimental data of Berkhoff et al. (1982) (section 5 - section8)

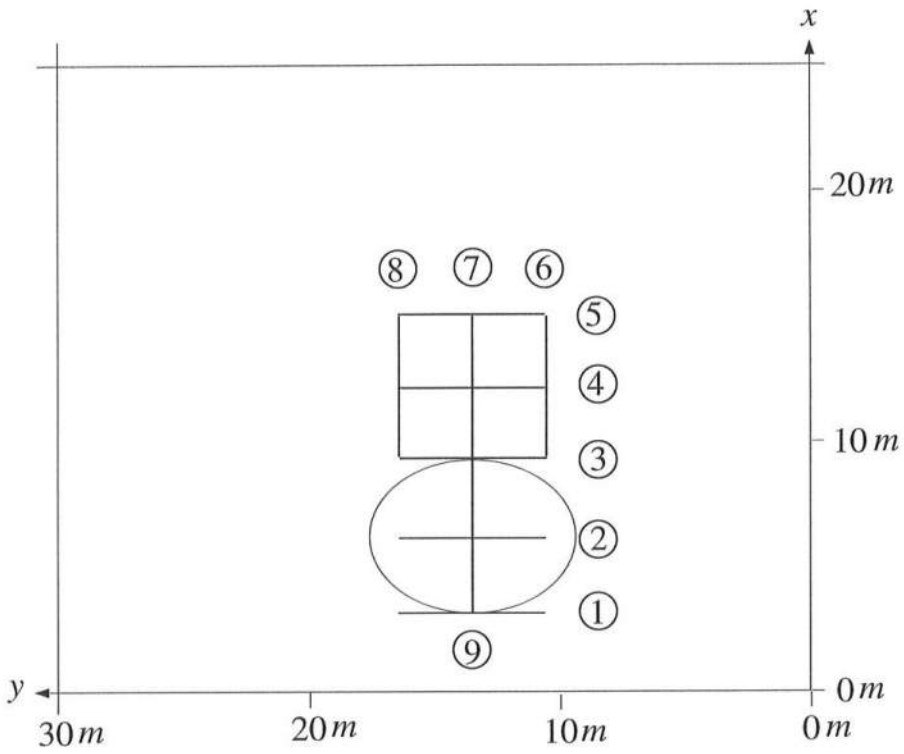

Figure 5.6: Experimental setup by Vincent and Briggs (1989)

Vincent and Briggs (1989) present a number of cases with a combination of monochromatic, narrow-banded or broad-banded frequency spectra and unidirectional, narrow-banded or broad-banded directional spreads. Here, we show results for three typical cases: a monochromatic unidirectional sea (M2), a sea with narrow frequency and narrow directional spreading (N4), and a sea with narrow frequency and broad directional spreading (B4). All three cases involve non-breaking waves. Wave period (M2) and peak period (N4, B4) are 1.30 s. Wave height (M2) and rms wave height (N4, B4) are 2.54 cm. Phillip's α is taken to be 0.00047.

Since the model equation (2.3) is not valid for an arbitrarily large range

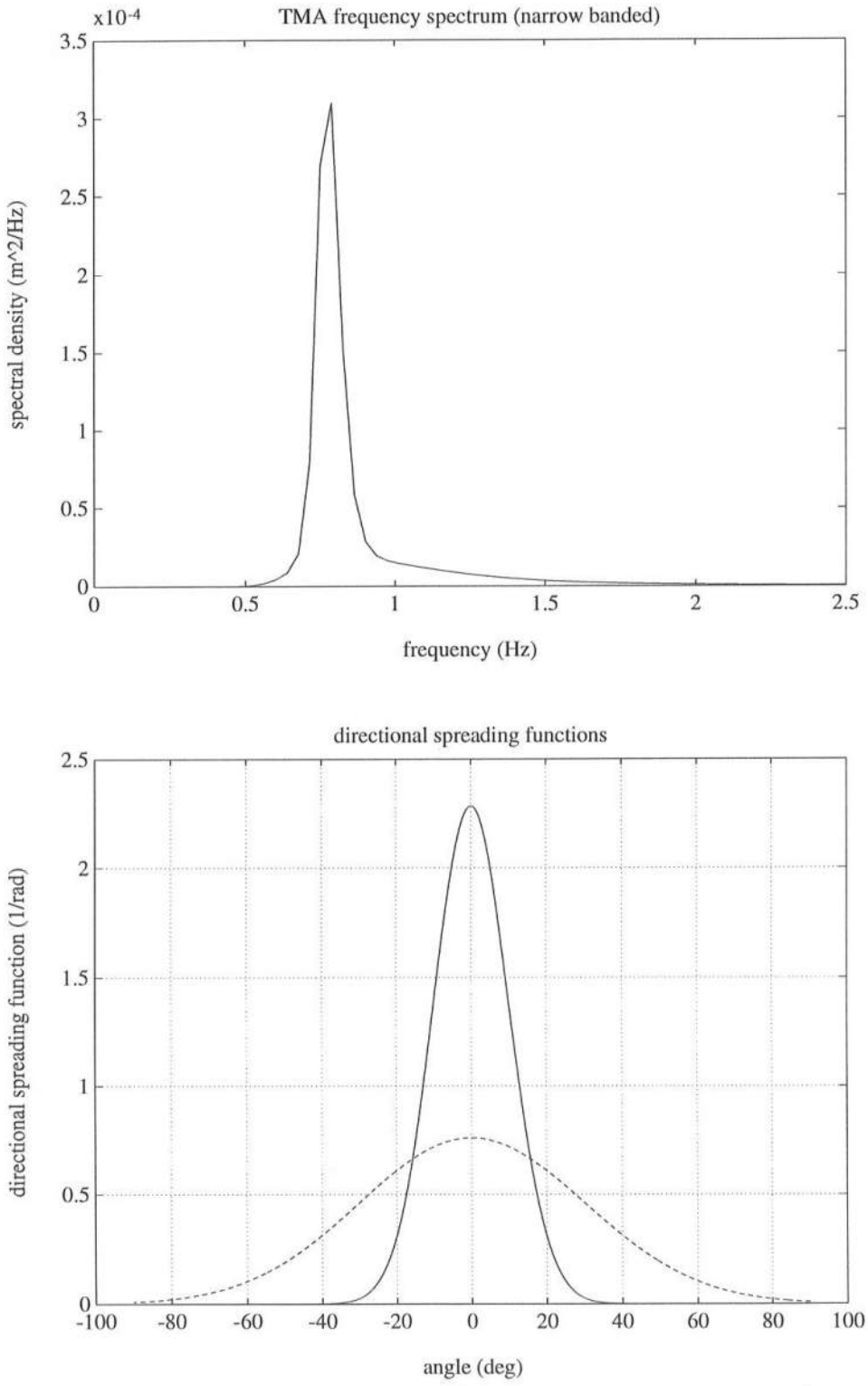

Figure 5.7: TMA frequency spectra (narrow frequency band) and directional spreading functions (solid lines : $\sigma_0 = 10°$, dashed lines : $\sigma_0 = 30°$)

Table 5.1: Test conditions considered for Vincent and Briggs' (1989) shoal experiment (non-breaking waves)

Case ID	Type	period (s)	height (cm)	α	γ	σ_m
M2	mono	1.30	2.54	—	—	—
N4	random	1.30	2.54	0.00047	20	10
B4	random	1.30	2.54	0.00047	20	30

of frequencies, we proceed by separating the whole spectrum into several bands. In each frequency band, we then construct a wavemaker or offshore boundary condition using the spectral information falling within that band. The time-dependent mild slope equation is then solved for the narrow-banded irregular sea lying within each frequency band. The final solution is obtained by adding the different bands.

Following Vincent and Briggs (1989), we use the TMA spectrum as the target frequency spectrum and a wrapped normal function as the directional spreading function. The TMA spectrum is given by

$$S(f) = \alpha g^2 (2\pi)^{-4} f^{-5} \exp\{-1.25(\frac{f_p}{f})^4 + (\ln\gamma)\exp[-\frac{(f-f_p)^2}{2\sigma^2 f_p^2}]\}\phi(f,h) \quad (5.23)$$

$S(f)$ depends on the parameters α (Phillip's constant), f_p (peak frequency) γ (peak enhancement factor) and σ (shape parameter). The factor $\phi(f,h)$ incorporates the effect of the depth h and may be approximated by

$$\phi = \begin{cases} 0.5\omega_h^2, & \omega_h < 1 \\ 1 - 0.5(2-\omega_h)^2, & 1 \le \omega_h \le 2 \\ 1, & \omega_h > 2 \end{cases} \quad (5.24)$$

where $\omega_h = 2\pi f(h/g)^{1/2}$. The parameter γ is assigned values of 2 (broad frequency) and 20 (narrow frequency). For the cases studied here, γ was assigned a value of 20. The directional spreading function $D(\theta)$ is obtained by assigning the

values of either 10° (narrow spreading) or 30° (broad spreading) to the spreading parameter σ_0:

$$D(\theta) = \frac{1}{2\pi} + \frac{1}{\pi}\sum_{n=1}^{N} \exp[-\frac{(n\sigma_0)^2}{2}] \cos n(\theta - \theta_0) \tag{5.25}$$

where θ_0 = mean wave direction (= 0°) and N = number of terms in the series (= 20).

We separate the whole frequency spectrum into three components with equal bandwidths of 0.267 Hz (see Figure 5.7). The three components of the frequency spectra cover 95 percent of the total spectral density in the range of f = 0.533 - 1.333 Hz, and, using the grid spacings chosen below, the ratio of minimum wavelength to spatial grid size is 4.54. We use a weighted average of the frequencies in each frequency band to determine the representative frequency used to compute the model coefficients for each band. The grid size is $\Delta x = \Delta y =$ 0.1905 m and time step is $\Delta t = 1.3/80$ s. We compute until $t = 260$ s. Variances of water surface elevation are computed between $t = 65$ s and $t = 260$ s.

In Figures 5.8 – 5.10, the water surface elevations in the whole spatial domain at $t = 260$ s are shown for cases M2, N4, and B4. The figure for case M2 shows that the waves are long-crested and symmetric along the line crossing the center of the shoal parrallel to x axis. After the waves pass the shoal they become short-crested because of refractive focusing. When we compare the cases with directional spreading (N4 and B4) we clearly see that the wave field with broad directional spreading (B4) is more short-crested than the wave field with narrow directional spreading (N4).

In Figure 5.11, the computed normalized wave heights along section 4 are

compared with measured data for cases M2, N4, and B4. For case M2, the normalized wave height near the centerline is greater than 2, which shows the considerable effects of refractive focusing over the shoal. For case N4, the computed results show underestimation near the centerline and overestimation away from the centerline. For case B4, the computed results show overestimation all along the section. The model results and data indicate that increasing directional spreading leads to much less spatial wave height variation induced by localized topographic irregularities. This result is seen in all spectral wave studies, and is a manifestation of the fact that the local minimums and maximums in the diffraction pattern for each spectral component overlap and experience mostly destructive interference.

Roughly, all three cases show that the model yields reasonably accurate results compared with the measured data. It is found that for directionally broad spreading case (B4) the refractive focusing effects are not noticeable behind the shoal.

When the computed normalized wave heights for case M2 shown in Figure 5.11 are compared with those from Panchang et al. (1990) who use the parabolic approximation of Radder (1979), our model results are more accurate than those from Panchang et al. When the computed normalized wave heights for case N4 shown in Figure 5.11 are compared with those from Suh and Dalrymple (1993) who use a very-wide angle model of the Berkhoff's equation, the accuracy is almost the same. Our model underestimated around the center while Suh and Dalrymple's model overestimated around the center. When the computed normalized wave heights for case B4 shown in Figure 5.11 are compared with those from Suh and Dalrymple (1993), the accuracy is almost the same. Both models overestimated almost everywhere along section 4.

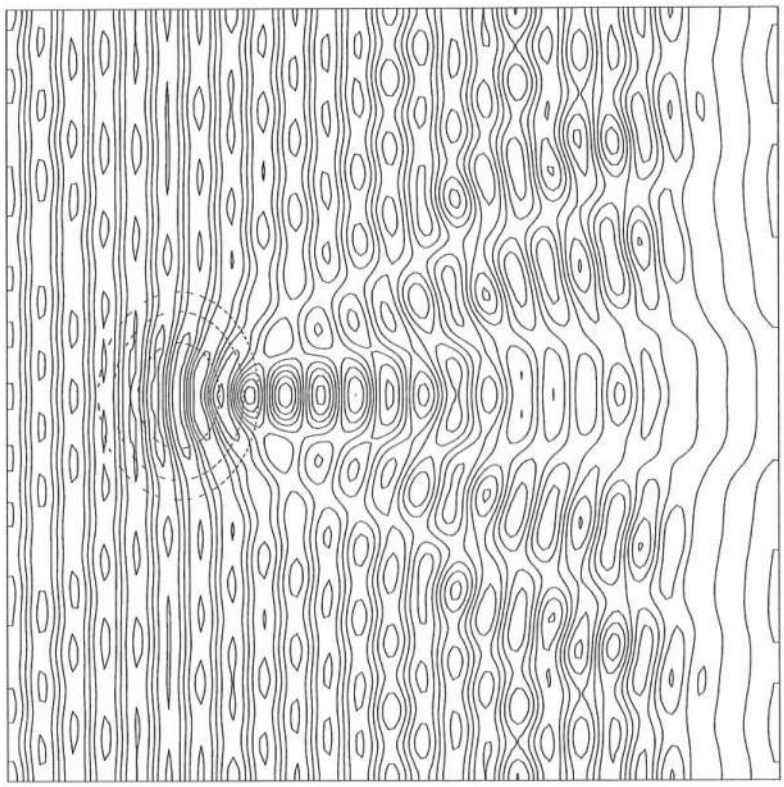

Figure 5.8: Water surface elevations at t = 260 s (case M2)

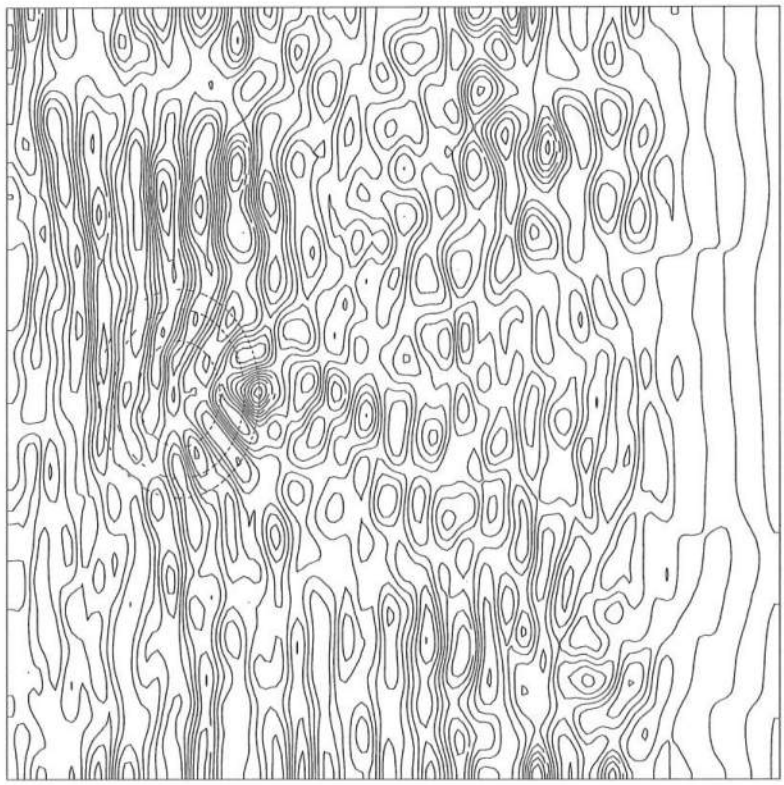

Figure 5.9: Water surface elevations at t = 260 s (case N4)

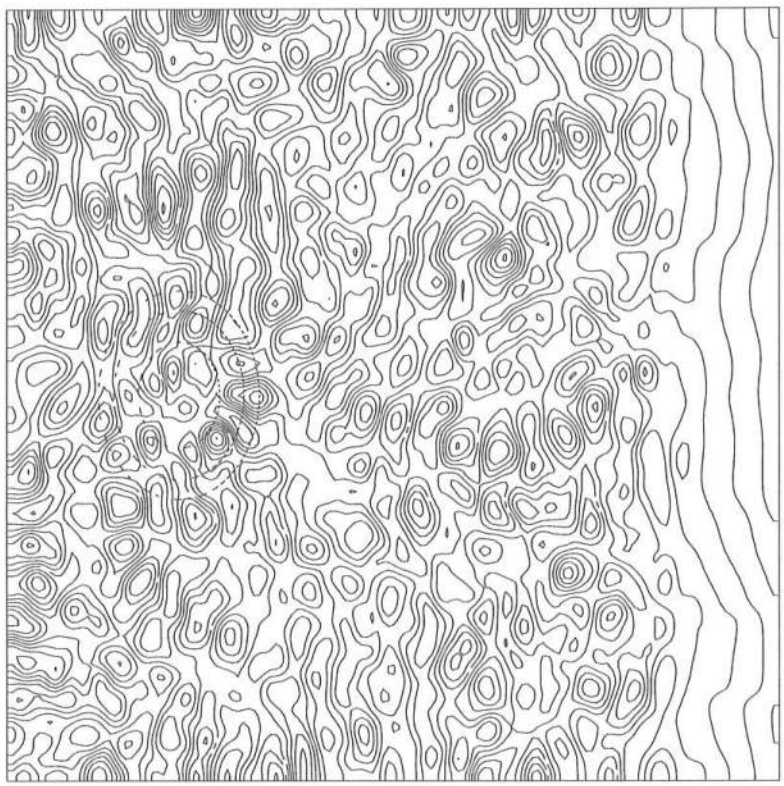

Figure 5.10: Water surface elevations at t = 260 s (case B4)

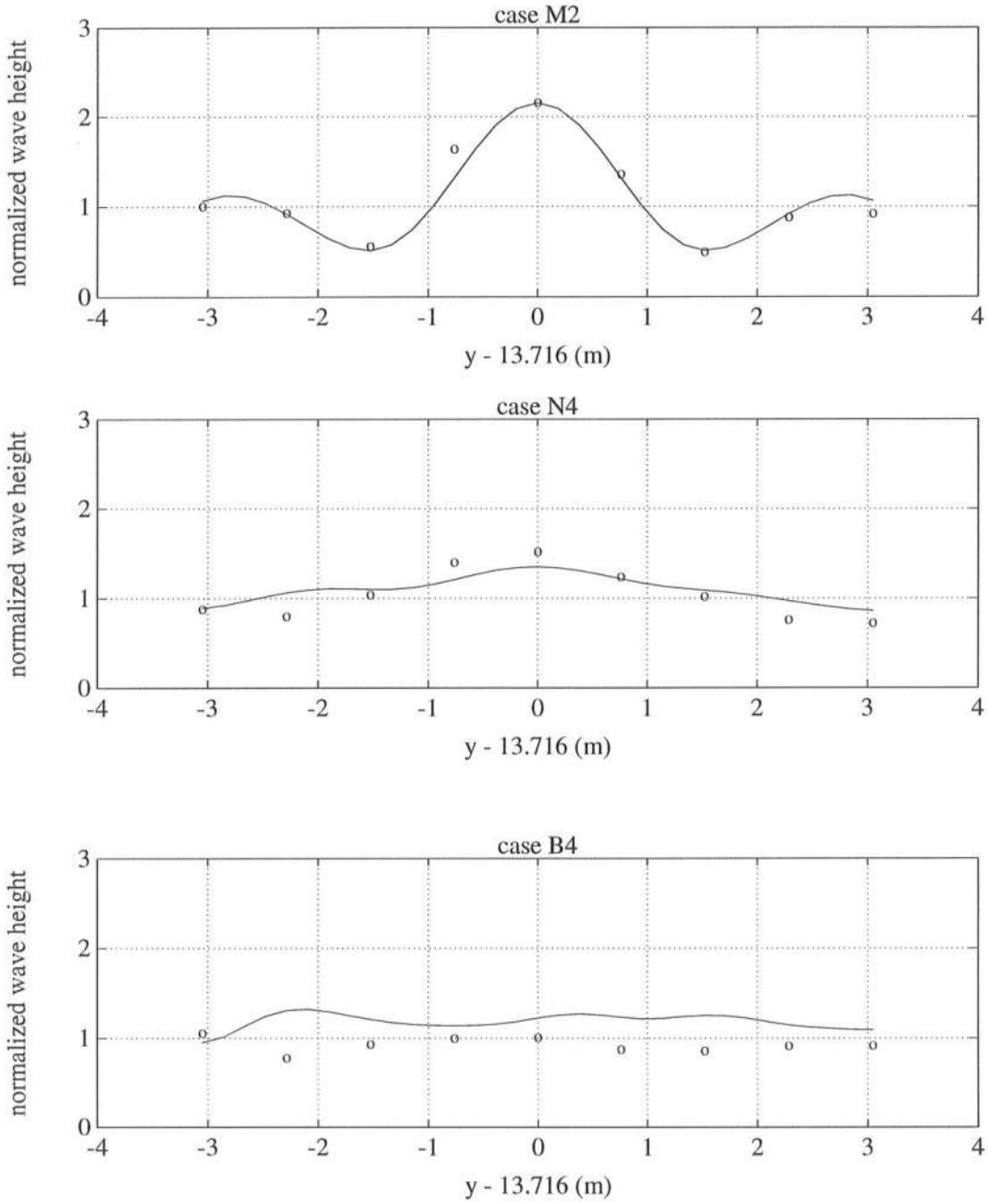

Figure 5.11: Measured and predicted normalized wave heights on section 4 for cases M2, N4, and B4 (o: measured wave height, solid line: predicted wave height)

5.3 Applications for Breaking Waves

5.3.1 Horikawa and Kuo Horizontal and Sloping Bottom Experiment (One-Dimensional Monochromatic Waves)

Horikawa and Kuo (1966) conducted two experiments inside the surf zone. The first experiment was done with a horizontal bottom to determine the reformed wave height after the stop of breaking. The resulting data was used by Dally et al. (1985) to determine the recovery criterion $(H/h)_r$ in which the breaking stops. The incident waves broke on a 1/5 sloping bottom and then propagated to the elevated horizontal bottom. The second experiment was done for a sloping bottom to reveal the influence of bottom slope on the wave transformation inside the surf zone.

For the first case, we consider the experiments conducted with a horizontal bottom of water depth $h_c = 15\ cm$, a wave period $T = 1.0\ s$, and a ratio of wave height to wavelength in deep water $H_0/L_0 = 0.065 - 0.100$. The grid size is $\Delta x = 0.2\ m$ and time step is $\Delta t = T/80\ s$. The computational domain is 1 m before the breaking point to 1 m after the breaking point. The values of the breaking criteria $(H/h)_b$ are found to be in the range of 0.63 to 0.89 with an increasing trend with the increasing value of H_0/L_0, while the value of $(H/h)_r$ is found to be in the range of 0.35 to 0.41 with no particular trends (see Figure 5.12 (a)). The optimum value of the factor of energy dissipation rate γ was chosen to be in the range of 0.4 to 0.9 with an increasing trend with the increasing value of H_0/L_0 (see Figure 5.12 (b)). Figure 5.13 (a) shows the comparison of the wave height attenuations with different values of γ (0.8, 0.9, 1.0) against the experimental data for the case with $H_0/L_0 = 0.100$, $(H/h)_b = 0.89$, $(H/h)_r = 0.37$. Figure 5.13 (b) shows the energy dissipation rates normalized by wave frequency for the case with $H_0/L_0 = 0.100$, $(H/h)_b = 0.89$, $(H/h)_r = 0.37$, $\gamma = 0.9$.

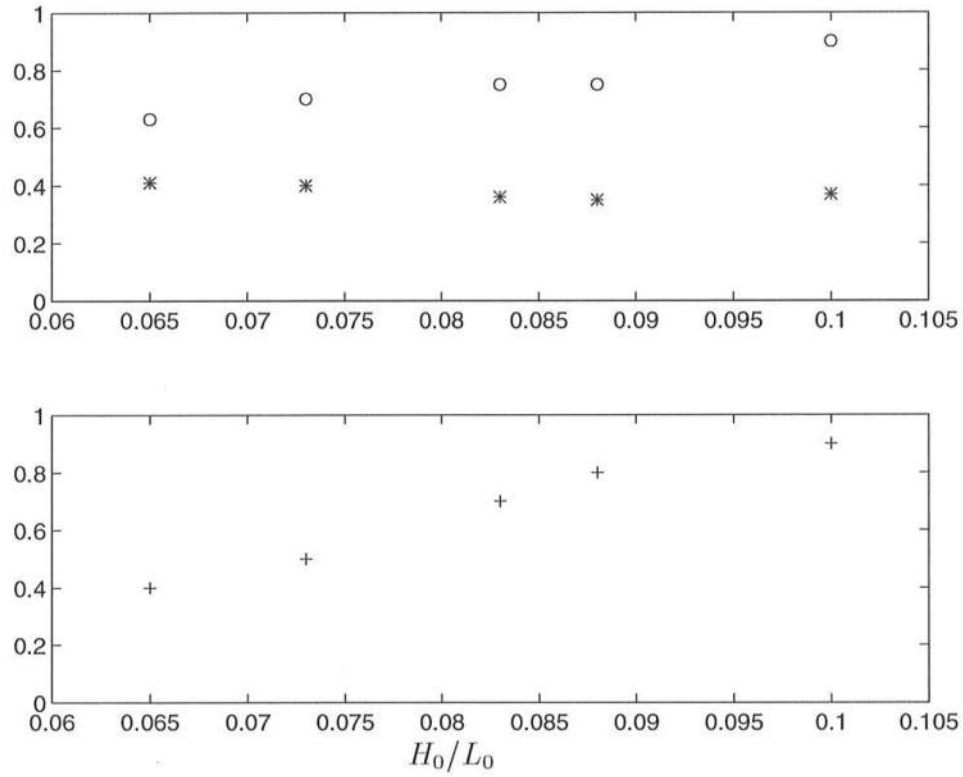

Figure 5.12: Wave breaking parameters for Horikawa and Kuo's (1965) horizontal bottom with $T = 1\ s$, $h_c = 15\ cm$ (a) $\circ$: $(H/h)_b$, $*$: $(H/h)_r$, (b) $+$: γ

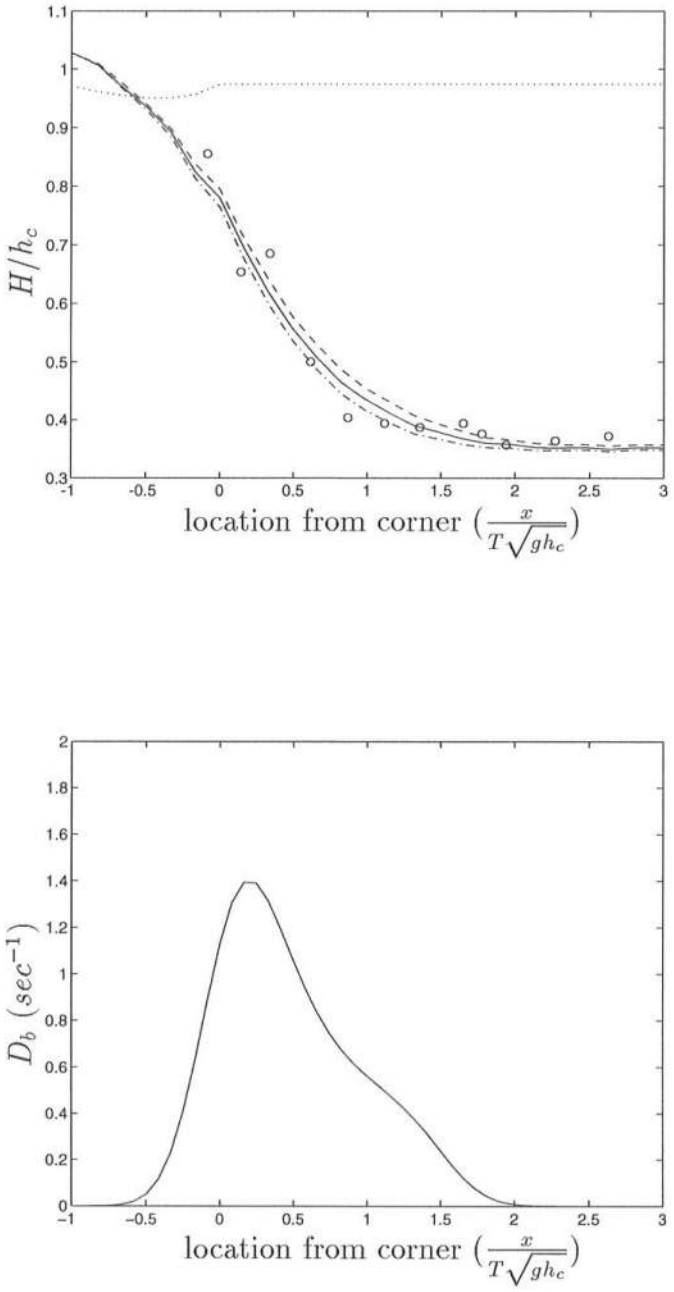

Figure 5.13: (a) Attenuation of wave height with different values of γ for $H_0/L_0 = 0.100$, $(H/h)_b = 0.89$, $(H/h)_r = 0.37$ (dashed line: $\gamma = 0.8$, solid line: $\gamma = 0.9$, dash-dotted line: $\gamma = 1.0$, dotted line: shoaling coefficient), (b) energy dissipation rates (D_b) for $H_0/L_0 = 0.100$, $(H/h)_b = 0.89$, $(H/h)_r = 0.37$, $\gamma = 0.9$

For the second case, we consider the experiments conducted with bottom slope $s = 1/65$, a wave period $T = 1.6\ s$, and a ratio of wave height to wavelength in deep water $H_0/L_0 = 0.065$. The grid size is $\Delta x = 0.2\ m$ and time step is $\Delta t = T/60\ s$. The computational domain is from $h = 1\ m$ to $h = 0.01\ m$. The value of $(H/h)_b$ is found to be in the range of 0.78 to 1.01 with a decreasing trend with the increasing value of H_0/L_0 (see Figure 5.14 (a)). The value of $(H/h)_r$ is fixed to be 0.35. The optimum value of γ was chosen to be in the range of 0.4 to 0.8 with a decreasing trend with the increasing value of H_0/L_0 (see Figure 5.14 (b)). Figure 5.15 (a) shows the comparison of the wave height attenuations with different values of γ (0.3, 0.4, 0.5) against the experimental data for the case with $H_0/L_0 = 0.065$, $(H/h)_b = 0.78$, and $(H/h)_r = 0.35$. It is noticable that even though different values of γ cause different effects of wave height attenuation, the wave heights converge to zero value at points near the shore. Figure 5.15 (b) shows the energy dissipation rates D_b for the case with $H_0/L_0 = 0.065$, $(H/h)_b = 0.78$, $(H/h)_r = 0.35$, and $\gamma = 0.4$. At the wave breaking point, the model underpredicted wave height due to nonlinear effects which are dominant at the breaking point, while the model used is linear. The energy dissipation rate decreased until the water depth of about 0.6 times the water depth at the breaking point and then it increased exponentially to the zero depth. This phenomenon was also found in terms of H/h in Horikawa and Kuo's experiments (1966).

It is noticable that the value of γ increases with the increasing value of $(H/h)_b$. The relation between $(H/h)_b$ and γ, for the horizontal bottom, is described as

$$\gamma = 1.913(H/h)_b - 0.767 \tag{5.26}$$

with regression coefficient 0.91 and, for the 1/65 sloping bottom, is described as

$$\gamma = 1.693(H/h)_b - 0.990 \tag{5.27}$$

with regression coefficient 0.92. The relations are shown in Figure 5.16.

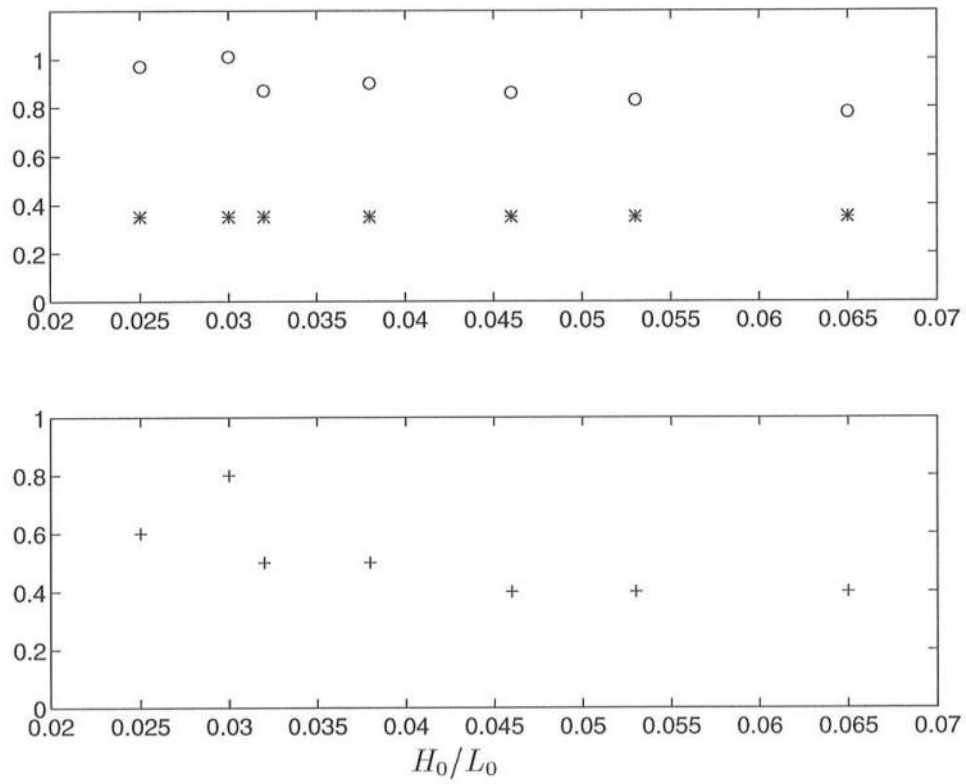

Figure 5.14: Wave breaking parameters for 1/65 sloping bottom and $T = 1.6\ s$ (a) $\circ$: $(H/h)_b$, $*$: $(H/h)_r$, (b) γ

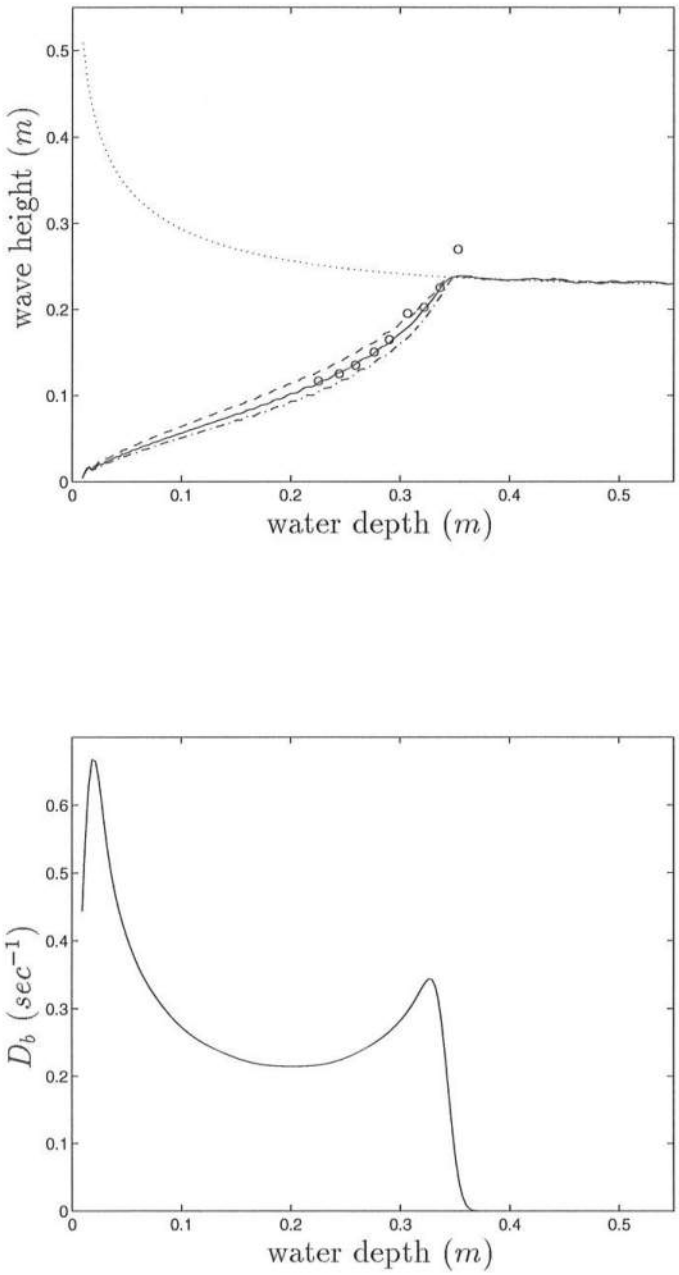

Figure 5.15: (a) Attenuation of wave height with different values of γ for $H_0/L_0 = 0.065$, $(H/h)_b = 0.78$, $(H/h)_r = 0.35$ (dashed line: $\gamma = 0.3$, solid line: $\gamma = 0.4$, dash-dotted line: $\gamma = 0.5$, dotted line: shoaling coefficient), (b) energy dissipation rates (D_b) for $H_0/L_0 = 0.065$, $(H/h)_b = 0.78$, $(H/h)_r = 0.35$, $\gamma = 0.4$.

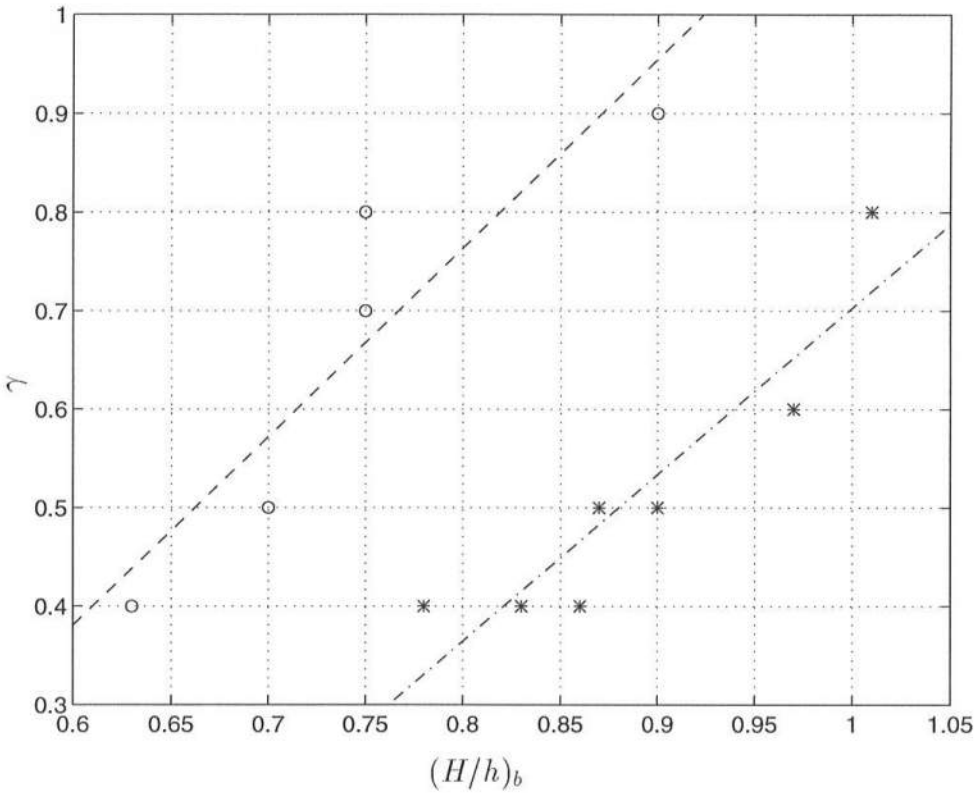

Figure 5.16: Relation between $(H/h)_b$ and γ ($\circ$: horizontal bottom, dashed line: regression line for horizontal bottom, $*$: 1/65 sloping bottom, dash-dotted line: regression line for 1/65 sloping bottom)

5.3.2 Mase and Kirby Plane Beach Experiment (One-dimensional Random Waves)

Mase and Kirby (1992) conducted experiments on one-dimensional random waves shoaling over a plane beach of slope 1/20 (see Figure 5.17). The random waves were simulated with a Pierson-Moskowitz spectrum with peak frequency (f_p) of 0.6 Hz and 1.0 Hz, referred to as case 1 and case 2, respectively. The dominant wave breaking type seen in case 1 was plunging, while in case 2 spilling

breakers were dominant. Water surface elevations were measured by capacitance-type wave gauges at the water depth of 47 cm, 35 cm, 30 cm, 25 cm, 20 cm, 17.5 cm, 15 cm, 12.5 cm, 10 cm, 7.5 cm, 5 cm, and 2.5 cm over the slope.

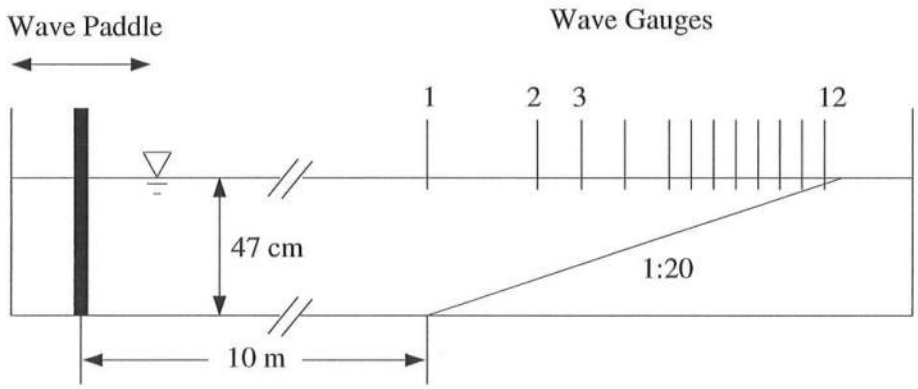

Figure 5.17: Experimental setup by Mase and Kirby (1992) (Wei and Kirby, 1993)

We consider case 1 here. The sampling interval is 0.04 s and total number of sampling values used is 16384. We subdivide the whole time series into four segments each of which has 4096 data points and we take the average of the four power spectra of the corresponding time series. The averaged power spectrum is shown in Figure 2.11. The incoming energy with extremely low frequencies cannot be absorbed in the sponge layer, while the values of η and $\tilde{\phi}$ with extremely high frequencies cannot be resolved numerically in space and in time. So, the spectrum including 2 percent of the lowest and highest frequencies is excluded in order to get reasonable solutions. The remaining 96 percent of the spectrum is in the range

of $f = 0.378$ - $1.605\ Hz$. The remaining 96 percent of the sepctral density of water surface elevations recorded at depth of 47 cm was separated into six components with equal bandwidths. We use a weighted average of the frequencies in each frequency component to determine the representative frequency used to compute the model coefficients for each component. We select the parameters for wave breaking as $(H/h)_b = 0.8$, $(H/h)_r = 0.35$, and $\gamma = 2$. The grid size is $\Delta x = 0.04$ m and time step is $\Delta t = 0.0025\ s$. The computational domain begins horizontally 1 m before the corner and continues horizontally 9 m after the corner. The water depth 9 m after the corner is 2 cm. The sponge layer is put after that point. From the chosen grid spacings, the minimum ratio of wavelength to spatial grid size is 6.6. Variances of water surface elevation are computed between $t = 25.255\ s$ and $t = 160\ s$.

We compare two cases: 1) a case with 4 frequency bands and 2) a case with 6 frequency bands, to see how the normalized wave heights are different. The normalized wave heights computed between $t = 25.255\ s$ and $160\ s$ are shown in Figure 5.18 where the computed wave heights outside the surf zone are not close to the measured wave heights for the case with 4 frequency bands, while the computed wave heights for the case with 6 frequency bands are very close to the measured wave heights. This shows computation with narrower frequency bands yields a smaller error.

Figures 5.19 and 5.20 show the water surface elevations η and energy dissipation rates $D_b + D_s$ from $t = 16\ s$ to $t = 160\ s$ at 16 s interval.

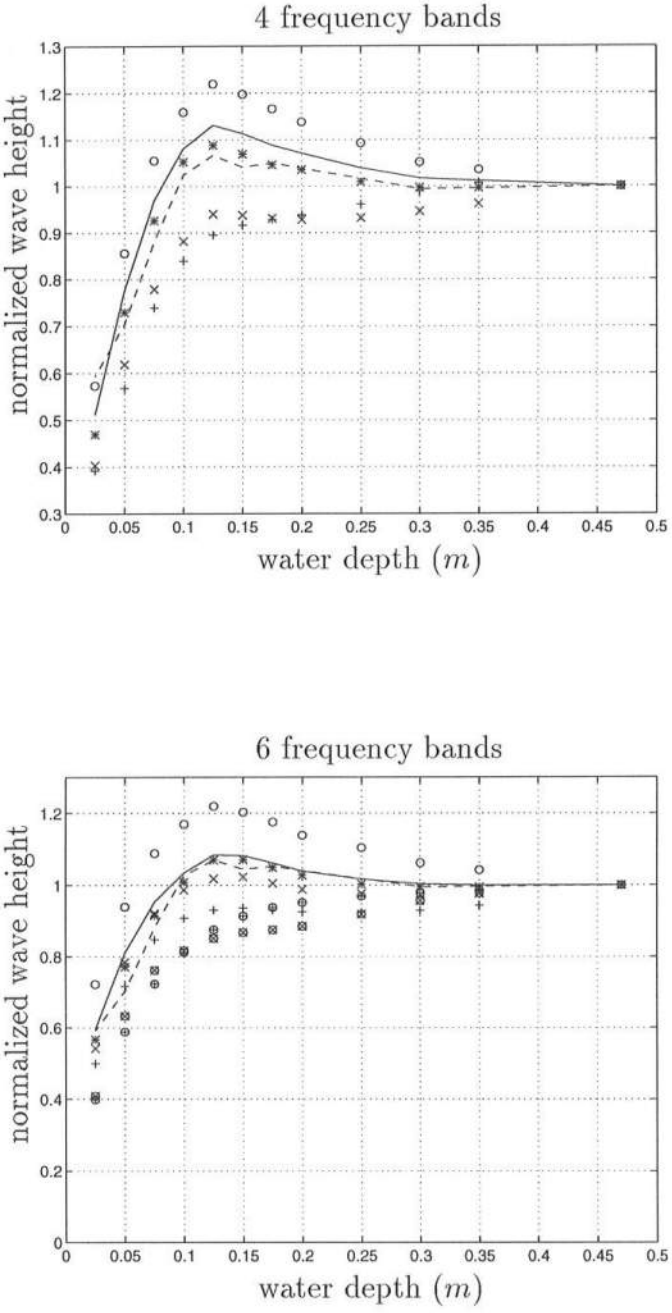

Figure 5.18: Normalized wave heights (dashed line: measured data, solid line: whole frequency component, ○: first frequency component, ∗: second frequency component, ×: third frequency component, +: fourth frequency component, ○ and ×: fifth frequency component, ○ and +: sixth component)

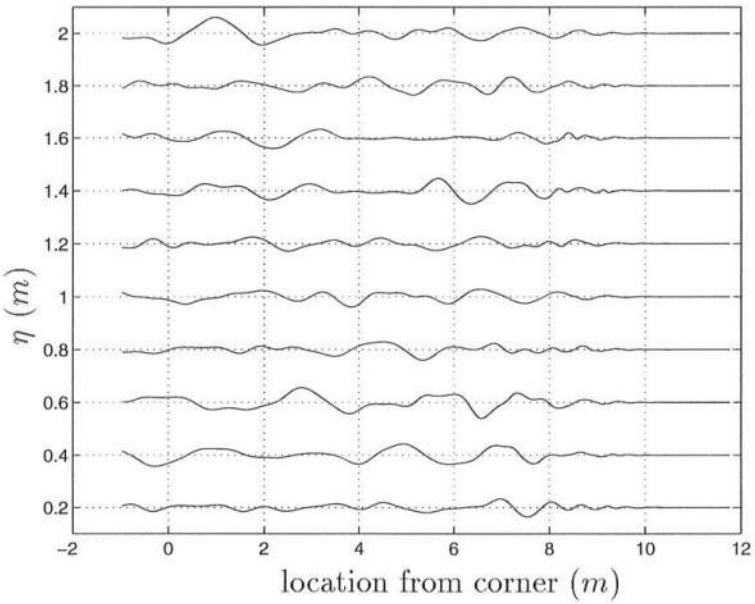

Figure 5.19: Water surface elevations from $t = 16$ s to $t = 160$ s at 16 s interval for case 1 with 6 frequency bands

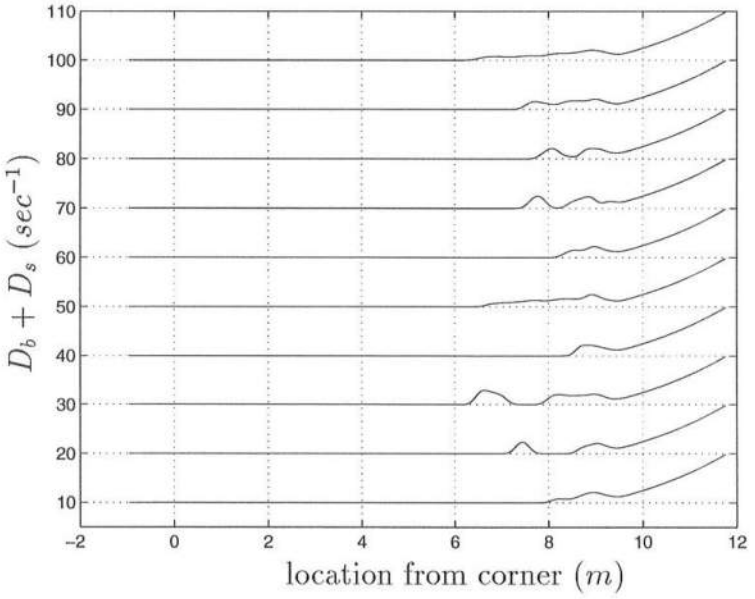

Figure 5.20: Energy dissipation rates $(D_b + D_s)$ from $t = 16$ s to $t = 160$ s at 16 s interval for case 1 with 6 frequency bands

5.3.3 Vincent and Briggs Shoal Experiment (Two-Dimensional Monochromatic and Random Waves)

Vincent and Briggs (1989) also presented a number of experiments for breaking waves with a combination of monochromatic, narrow-banded, or broad-banded frequency spectra and unidirectional, narrow-banded, or broad-banded directional spreads. Here we test three typical cases: a monochromatic unidirectional sea (M3), a sea with narrow directional spreading (N5), and a sea with broad directional spreading (B5). The input conditions to generate waves are shown in Table 5.2.

Table 5.2: Test conditions considered for Vincent and Briggs' (1989) shoal experiment (breaking waves)

Case ID	Type	period (s)	height (cm)	α	γ	σ_m
M3	mono	1.30	13.50	—	—	—
N5	random	1.30	19.00	0.02620	20	10
B5	random	1.30	19.00	0.08650	2	30

For a monochromatic unidirectional wave (M3), input wave height is $H = 13.50\ cm$, and a wave period is $T = 1.3\ s$. We select the parameters for wave breaking as $(H/h)_b = 0.8$, $(H/h)_r = 0.35$, $\gamma = 1$. The grid sizes are $\Delta x = \Delta y = 0.1905\ m$, and time step is $\Delta t = T/80\ s$. The average wave heights are computed between $t = 17.7125\ s$ and $t = 39\ s$.

Figure 5.21 shows the water surface elevations and wave phase velocities at $t = 39\ s$. Figure 5.22 shows the energy dissipation rates caused by wave breaking which extends from the shoal to section 4 with narrow width.

Figures 5.23 and 5.24 show water surface elevations η and enegy dissipation rates D_b from $t = 3.9\ s$ to $t = 39\ s$ at $3.9\ s$ interval along the center line parallel

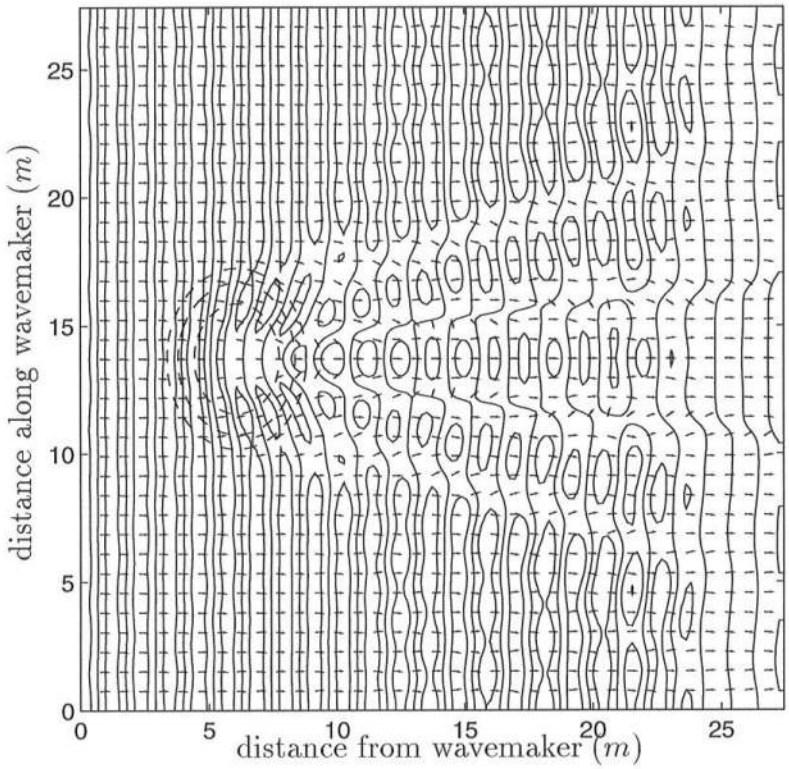

Figure 5.21: Water surface elevations at $t = 39\ s$ for case M3 with $(H/h)_b = 0.8$, $(H/h)_r = 0.35$ and $\gamma = 1$ (solid line: contour of water surface elevations, dashed line: contour of bottom topography, arrow: wave vector)

to x axis. We see the propagation of breaking waves from Figure 5.24.

Figure 5.25 shows that the computed normalized wave heights are not close to the measured data because nonlinearity is dominant near the shoal and the wavelength and phase velocity increase resulting in defocusing of waves behind the shoal. The linear model used shows the refractive focusing of waves behind the shoal. This higher phase velocity and wave defocusing was also found by Chawla (1994).

For cases N5 and B5, we exclude 2 percent lower and upper frequency

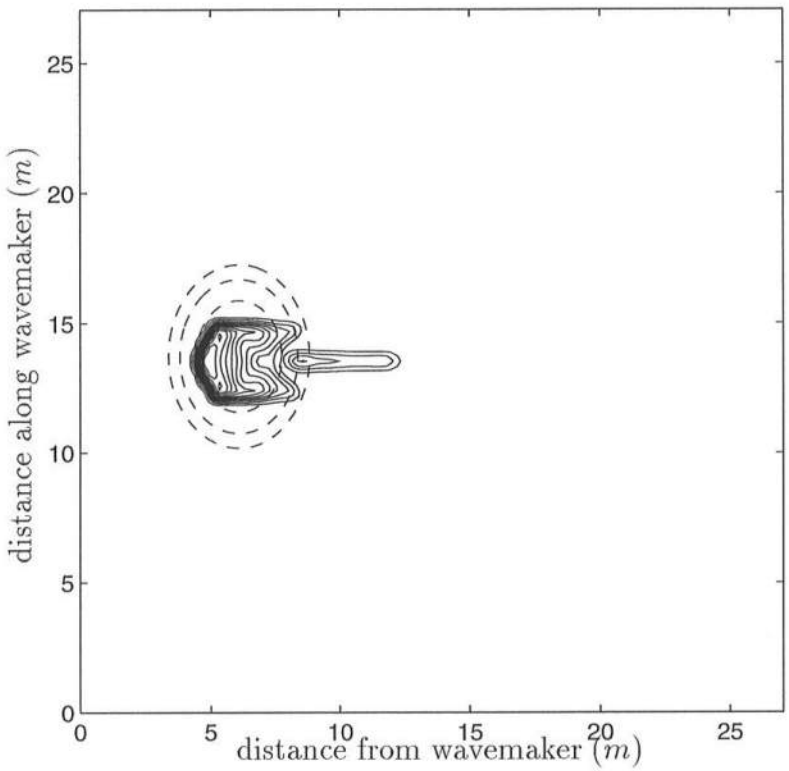

Figure 5.22: Energy dissipation rates (D_b) at $t = 39\ s$ for case M3 with $(H/h)_b = 0.8$, $(H/h)_r = 0.35$ and $\gamma = 1$ (solid line: contour of energy dissipation rates, dashed line: contour of bottom topography)

components from the whole spectrum to get stable solutions. So, the frequency ranges used are $f = 0.67$ - $1.70\ Hz$ (case N5) and $f = 0.62$ - $2.26\ Hz$ (case B5). We subdivide the spectrum into 3 components with equal bandwidths, and we use weight-averaged frequencies as representative frequencies in computing the coefficients $\bar{\omega}$, $\bar{k}$, $\bar{C}$ and $\bar{C}_g$. The grid sizes are $\Delta x = \Delta y = 0.1905\ m$, and time step is $\Delta t = T/80\ s$ where the peak wave period is $T = 1.3\ s$. We compute until $t = 130\ s$ and compute the variance of water surface elevations between $t = 34.125\ s$ and $t = 130\ s$. The water surface elevations at $t = 130\ s$ for case N5 are shown in in Figure 5.26 where the solid line represents water surface elevation and the

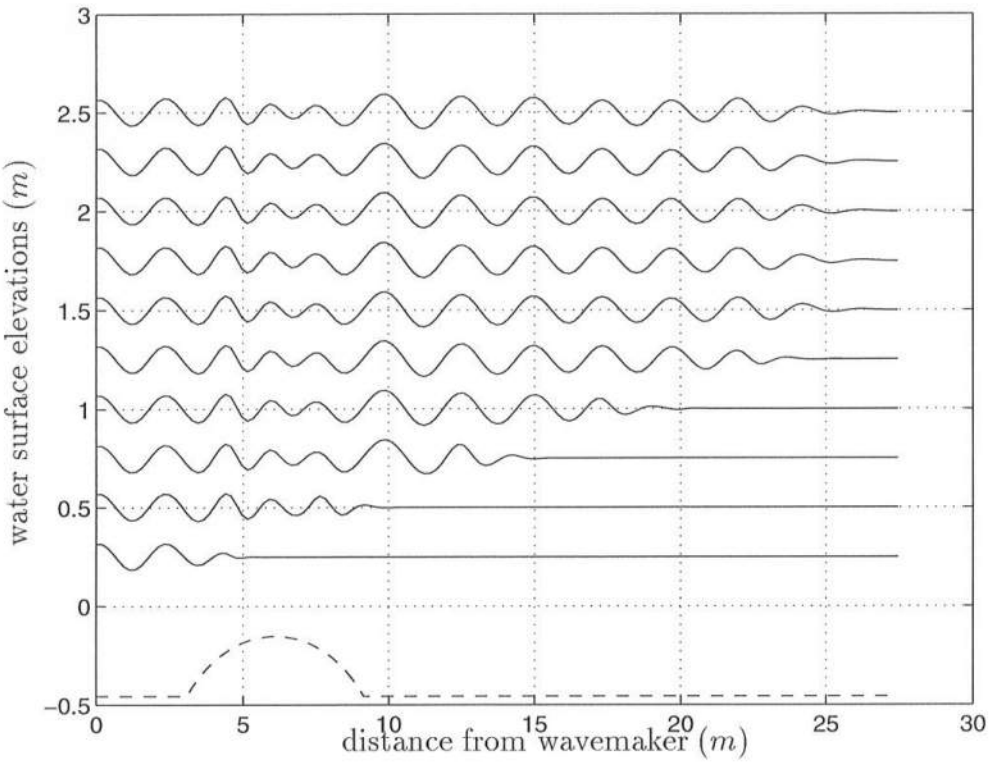

Figure 5.23: Water surface elevations from $t = 3.9$ s to $t = 39$ s at 3.9 s intervals along the center line parallel to x axis for case M3 with $(H/h)_b = 0.8$, $(H/h)_r = 0.35$ and $\gamma = 1$

dashed line represents bottom topography. The waves shown in Figure 5.26 are long-crested because the particle velocities u at wavemaker boundary $x = 0$ are generated from the condition of narrow directional spreading. Figure 5.27 shows energy dissipation rates at $t = 130$ s for case N5. Wave breaking occurs not only around the shoal but also at the wavemaker and the side walls.

Figure 5.28 shows the comparison of the computed and measured normalized wave heights along section 4 for case N5. The measured data show wave breaking occurs everywhere along the section, which can be seen also from the computed data. Around the center line, normalized wave heights are smaller than

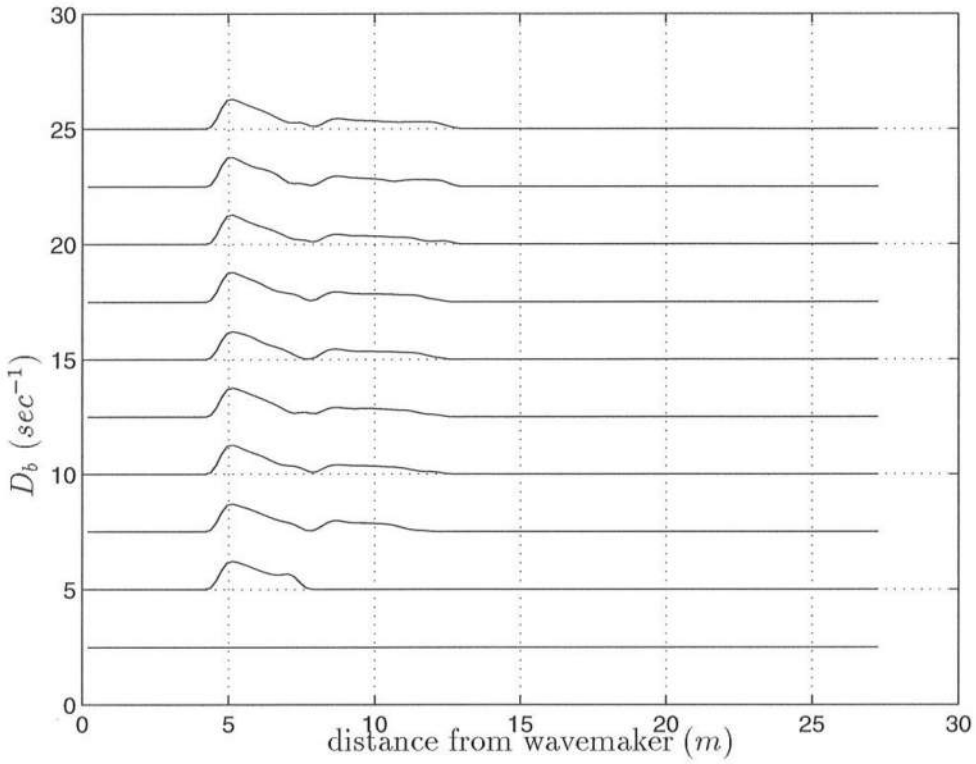

Figure 5.24: Energy dissipation rates (D_b) from $t = 3.9\ s$ to $t = 39\ s$ at $3.9\ s$ intervals along the center line parallel to x axis for case M3 with $(H/h)_b = 0.8$, $(H/h)_r = 0.35$ and $\gamma = 1$

those away from the center line, but the computed results show a little focusing of waves.

The water surface elevations at $t = 130\ s$ for case B5 are shown in Figure 5.29. The waves shown in Figure 5.29 are short-crested because the particle velocities u at the wavemaker boundary $x = 0$ are generated from the condition of broad directional spreading. The energy dissipation rates at $t = 130\ s$ for case B5 are shown in Figure 5.30 where wave breaking occurs not only around the shoal but also at the wavemaker and the side walls.

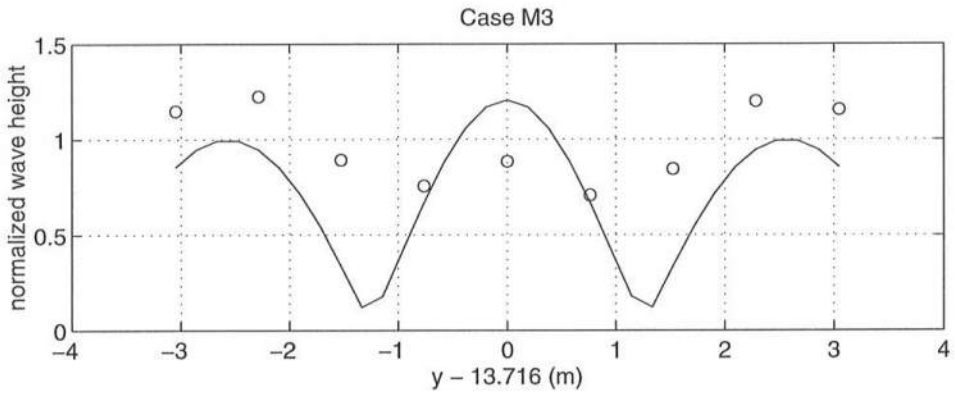

Figure 5.25: Measured and computed normalized wave heights along section 4 for case M3 (o: measured data, solid line: computed results).

Figure 5.31 shows the comparison of the computed and measured normalized wave heights along section 4 for case B5. Measured wave heights around the center for case B5 are smaller than those for case N5 which means wave breaking occurs more around the center for case B5 than for case N5. The computed wave heights show that wave breaking happens everywhere along section 4 with almost equal frequency.

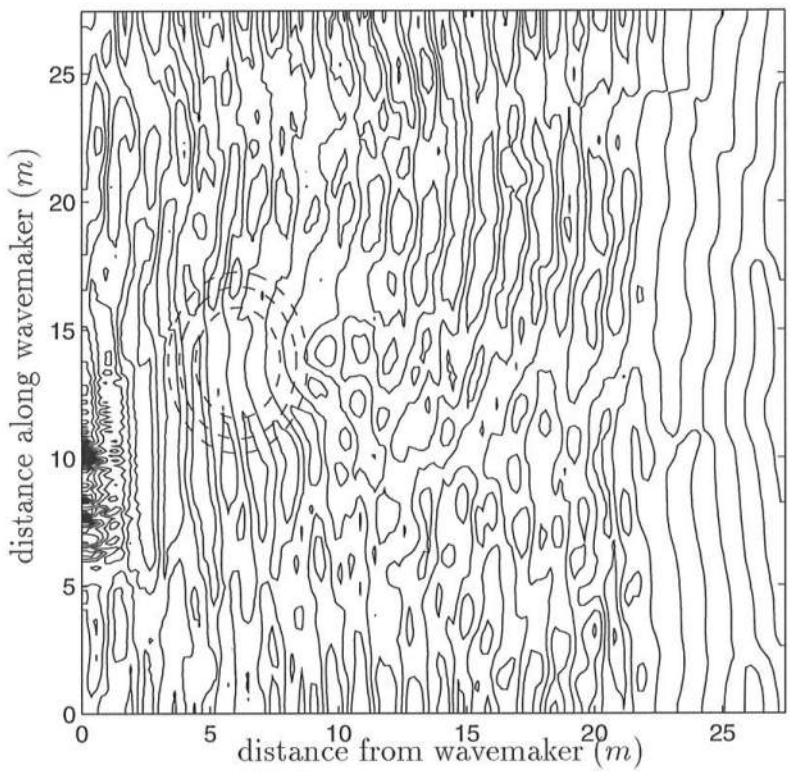

Figure 5.26: Water surface elevations at $t = 130\ s$ for case N5 (solid line: contour of water surface elevations, dashed line: contour of bottom topography)

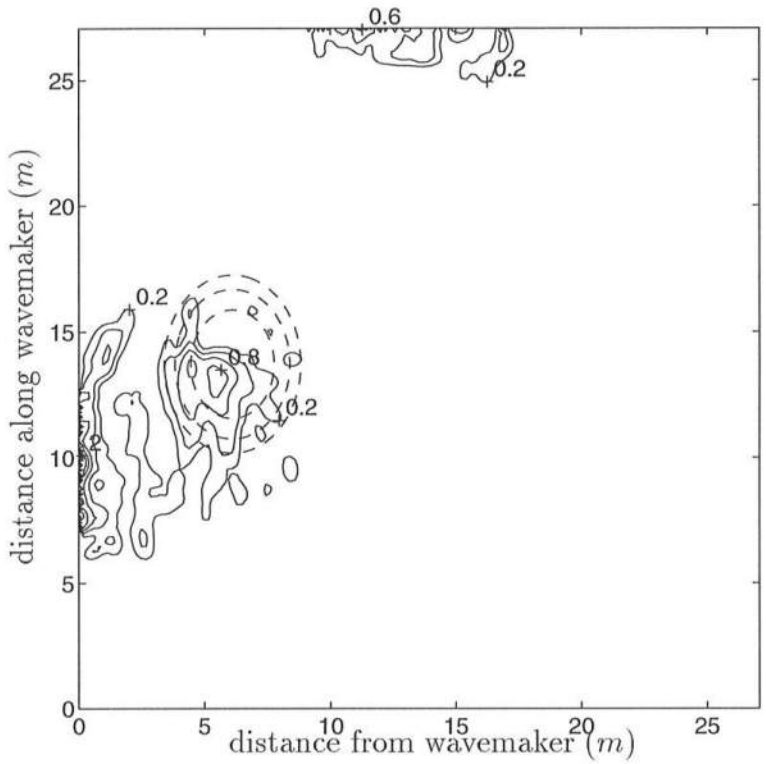

Figure 5.27: Energy dissipation rates (D_b) at $t = 130\ s$ for case N5 (solid line: contour of energy dissipation rates, dashed line: contour of bottom topography)

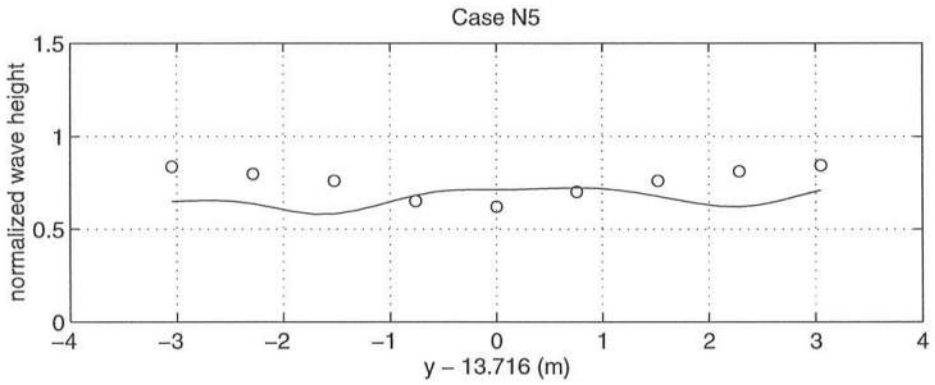

Figure 5.28: Normalized wave heights along section 4 for case N5 (o: measured data, solid line: computed results)

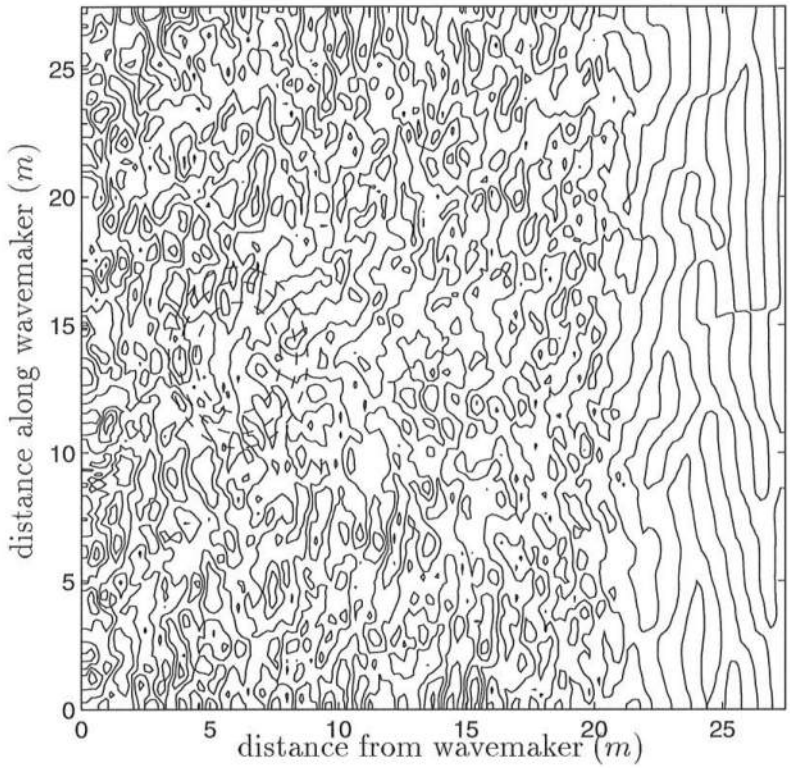

Figure 5.29: Water surface elevations at $t = 130\ s$ for case B5 (solid line: contour of water surface elevations, dashed line: contour of bottom topography)

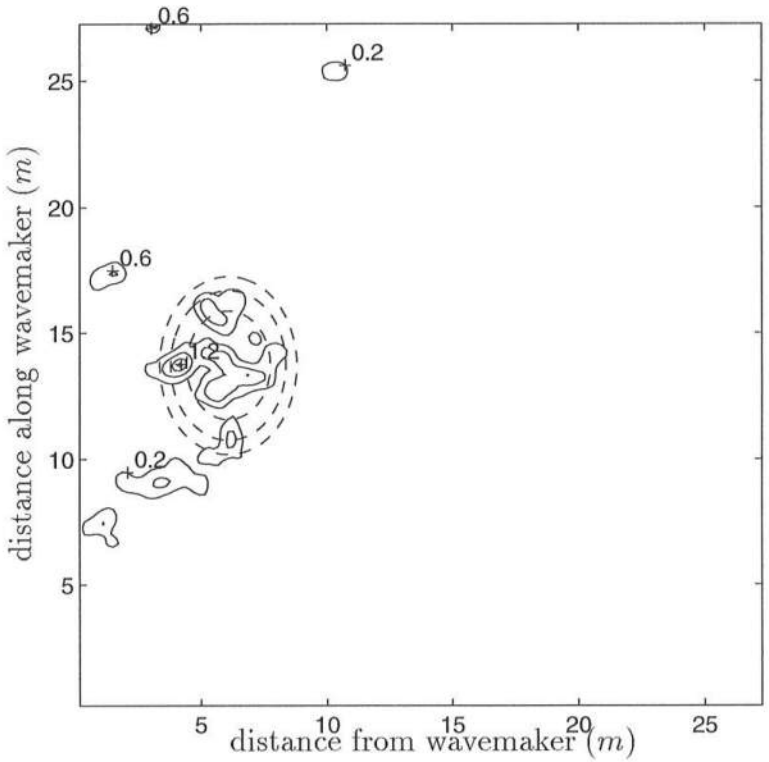

Figure 5.30: Energy dissipation rates (D_b) at $t = 130\ s$ for case B5 (solid line: contour of energy dissipation rates, dashed line: contour of bottom topography)

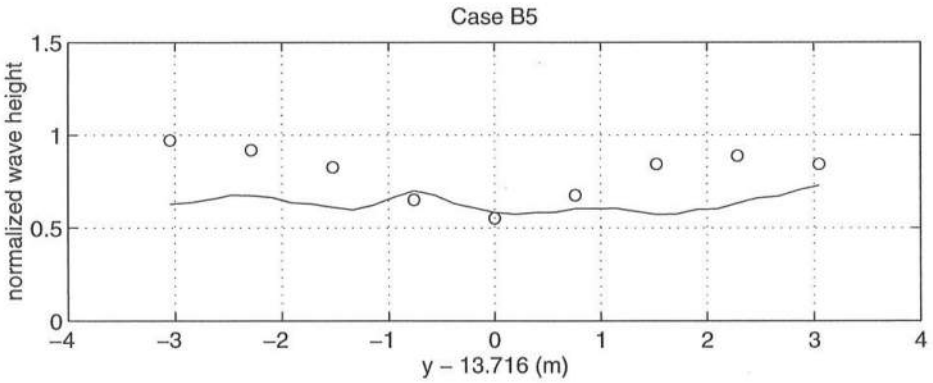

Figure 5.31: Normalized wave heights along section 4 for case B5 (o: measured data, solid line: computed results)

Chapter 6

CONCLUSIONS

We analyze existing time-dependent mild-slope equations which were developed by Smith and Sprinks (1975) (or, equivalently, Radder and Dingemans (1985)) and Kubo et al. (1992) in terms of dispersion relation, energy transport, and wave kinematics. One-dimensionally in the horizontal direction, we compare the modulation of wave amplitudes for the time-dependent mild-slope equations against the linear Schrödinger equation which is accurate to $O(\Delta k)^2$. We test the Radder and Dingemans' model and Kubo et al.'s model numerically for bichromatic waves in deep, intermediate-depth, and shallow waters. It is found that Smith and Sprinks' model is more accurate in shallower water ($\bar{k}h \leq 0.2\pi$) and satisfies the linear Schrödinger equation in very shallow water ($\bar{k}h \simeq 0$) and that Kubo et al.' model is more accurate in deeper water ($\bar{k}h > 0.2\pi$) and satisfies the linear Schrödinger equation at a point of intermediate water depth ($\bar{k}h \simeq 0.3\pi$). The numerical comparisons for bichromatic waves confirm the analytical comparisons.

We develop two new time-dependent mild-slope equations both of which satisfy the linear Schrödinger equation by adding correcting terms to the existing time-dependent mild-slope equations. We test a new model numerically for bichromatic waves at deep, intermediate-depth, and shallow waters in order to show the new model's better accuracy than the existing models.

We develop a model to obtain energy dissipation rates caused by wave breaking using a bore analogy, and include it in time-dependent mild-slope equations. Three breaking parameters would be specified to get solutions: the factor of the energy dissipation rate γ, the breaking criterion $(H/h)_b$, and the wave recovery criterion $(H/h)_r$. A method of succesive 3-point averaging is used in computation in order to get stable solutions.

We apply non-breaking and breaking versions of Radder and Dingemans' model for several cases including one-dimensional and two-dimensional, monochromatic and random, and non-breaking and breaking waves. The energy dissipation rates γ are in the range of 0.4 to 0.9 from applications of the model to Horikawa and Kuo's experiments which are all for monochromatic waves. From applications of the model to Mase and Kirby's experiment which is for random waves with plunging breaker, the value of γ is 2. The wave breaking criteria $(H/h)_b$ are in the range of 0.63 to 1.01 for Horikawa and Kuo's experiment. The value of wave recovery criterion is in the range of 0.35 to 0.41. The relation between γ and $(H/h)_b$ is found to be linearly proportional with a positive slope.

The chosen model underpredicts wave heights at the breaking point because nonlinearity is dominant at the breaking point and the model used is linear. For random breaking waves, the value of γ is found to be much higher compared to the value of γ for monochromatic waves. Nonlinear wave-wave interactions are dominant in the surf zone which cannot be considered in the linear model.

For further study, we suggest the following research topics:

First, we can develop a two-dimensional new time-dependent mild-slope equation which is accurate to $O(\Delta k)^2$. When we compare the existing time-dependent mild-slope equations to the linear Schrödinger equation one-dimensionally

in the horizontal direction, we get the time-dependent mild-slope equations. We can extend this approach to two dimensions in the horizontal direction.

Second, if currents are included in the wave problem, we can develop a new time-dependent mild-slope wave equation with currents. The wave-current interaction problems for Smith and Sprinks' model are studied by Booij (1981) and Kirby (1984).

Third, we can apply the time-dependent mild-slope equation for many cases of breaking waves which have measured data in order to give guidance in determining the parameters for wave breaking $(H/h)_b$ and γ.

REFERENCES

Battjes, J. A. and Janssen, J. P. F. M., 1978, "Energy loss and set-up due to breaking of random waves," *Proceedings of the 16th Coastal Engineering Conference*, Hamburg, 569-587.

Berkhoff, J. C. W., 1972, "Computation of combined refraction-diffraction," *Proceedings of the 13th Coastal Engineering Conference*, Vancouver, 471-490.

Berkhoff, J. C. W., Booij, N., and Radder, A. C., 1982, "Verification of numerical wave propagation models for simple harmonic linear waves," *Coastal Engineering*, 6, 255-279.

Booij, N., 1981, "Gravity waves on water with non-uniform depth and current," Report No. 81-1, Dept. of Civil Engineering, Delft University of Technology, Delft.

Bouws, E. and Battjes, J. A., 1982, "A Monte Carlo approach to the computation of refraction of water waves," *J. of Geophysical Research*, 87, No. C8, 5718-5722.

Chawla, A., 1994 "Phase speed analysis of breaking and shoaling waves," Term Paper for Advanced Water Wave Mechanics.

Dally, W. R. and Dean, R. G., 1986, "Transformation of random breaking waves on surf beat," *Proceedings of the 20th International Conference on Coastal Engineering*, Taipei, 109-123.

Dally, W. R., Dean, R. G., and Dalrymple, R. A., 1985, "Wave height variation across beaches of arbitrary profile," *J. of Geophysical Research*, 90, 11917-11927.

Dalrymple, R. A. and Kirby, J. T., 1988, "Models for very wide-angle water waves and wave diffraction," *J. of Fluid Mechanics*, 192, 33-50.

Dalrymple, R. A. Suh, K. D., Kirby, J. T., and Chae, J. W., 1989, "Models for very wide-angle water waves and wave diffraction Part 2. Irregular bathymetry," *J. of Fluid Mechanics*, 201, 299-322.

Fletcher, C. A. J., 1988, *Computational Techniques for Fluid Dynamics Volume 1*, 85-88.

Galvin, C. J., 1968, "Breaker type classification on three laboratory beaches," *J. of Geophysical Research*, 73, 3651-3659.

Horikawa, K., and Kuo, C. T., 1966, "A study on wave transformation inside surf zone," *Proceedings of the 10th Coastal Engineering Conference*, Tokyo, 217-233.

Iversen, H. W., 1951, "Laboratory study of breakers," *Gravity Waves, U.S. Bureau of Standards Circular* No. 521, 9-32.

Keller, J. B., 1958, "Surface waves on water of non-uniform depth," *J. of Fluid Mechanics*, 4, 607-614.

Kirby, J. T., 1984, "A note on linear surface wave-current interaction over slowly varying topography," *J. of Geophysical Research*, 89, 745-747.

Kirby, J. T., 1986, "Higher order approximation in the parabolic equation method for water waves," *J. of Geophysical Research*, 91, 933-952.

Kirby, J. T. and Dalrymple, R. A., 1983, "A parabolic equation for the combined refraction-diffraction of Stokes waves by mildly varying topography," *J. of Fluid Mechanics*, 136, 453-466.

Kirby, J. T. and Dalrymple, R. A., 1984, "Verification of a parabolic equation for propagation of weakly-nonlinear waves," *Coastal Engineering*, 8, 219-232.

Kirby, J. T. and Dalrymple, R. A., 1986, "Modelling waves in surfzones and around islands," *J. of Waterway, Port, Coastal, and Ocean Engineering*, 112, 1986.

Kirby, J. T. and Lee, C., 1993, "Short waves in a rotating, shallow tank with bathymetry: a model equation in the mild-slope approximation," *SIAM J. on Applied Mathematics*, 53, 1381-1400.

Kirby, J. T., Lee, C., and Rasmussen, C., 1992, "Time-dependent solutions of the mild-slope wave equation," *Proceedings of the 23rd International Conference on Coastal Engineering*, Venice, 391-404.

Kubo, Y., Kotake, Y., Isobe, M., and Watanabe, A., 1992, "Time-dependent mild slope equation for random waves," *Proceedings of the 23rd International Conference on Coastal Engineering*, Venice, 419-431.

Isobe, M., 1987, "A parabolic equation model for transformation of irregular waves due to refraction, diffraction and breaking," *Coastal Engineering in Japan*, 30, 38-48.

Lamb, H., 1932, *Hydrodynamics*, Dover Publications, 6th edition, New York.

Larsen, J., 1978, "A harbour theory for wind-generated waves based on ray methods," *J. of Fluid Mechanics*, 87, 143-158.

Leontovich, M. and Fock, V. A., 1944, "A method of solution of problems of electromagnetic wave propagation along the Earth's surface," *Izvestiia Akademiia Nauka, USSR* 8: 16-22.

Liu, P. L.-F. and Mei, C. C., 1976, "Water motion on a beach in the presence of a breakwater 1. Waves," *J. of Geophysical Research*, 81, 3079-3084.

Ludwig, D., 1966, "Uniform asymptotic expansions at a caustic," *Communications on Pure and Applied Mathematics*, 19, 215-250.

Mase H. and Kirby, J. T., 1992, "Hybrid frequency-domain KdV equation for random wave transformation," *Proceedings of the 23rd International Conference on Coastal Engineering*, Venice, 474-487.

McCowan, J., 1891, "On the solitary wave," *The London, Edinburgh and Dublin Philosophical Magazine and Journal of Science*, 32, 45-58.

Mei, C. C., 1989, *The Applied Dynamics of Ocean Surface Waves*, World Scientific, New Jersey, 47-50.

Miche, R., 1944, "Mouvements ondulatoirs des mers en profondeur constante on decroissant," *Annals des Ponts et Chaussees* (translation by Lincoln and Chevron, University of California at Berkeley, Wave Research Laboratory, Series 3, Issue 363, June, 1954).

Michell, J. H., 1893, "On the highest waves in water," *The London, Edinburgh and Dublin Philosophical Magazine and Journal of Science*, 36, 430-437.

Munk, W. H. and Arthur, R. S., 1952, "Wave intensity along a refracted ray," *Gravity Waves, U.S. Bureau of Standards Circular* No. 521, 95-108.

O'Brien, M. P, 1942, "A summary of the theory of oscillatory waves," *U.S. Army Beach Erosion Board Technical Reports* No. 2.

Panchang, V. G., Pearce, B. R., Wei, G., and Cushman-Roisin, B, 1991, "Solution of the mild-slope wave problem by iteration," *Applied Ocean Research*, 13, 187-199.

Panchang, V. G., Wei, G., Pearce, B. R., and Briggs, M. J., 1990, "Numerical simulation of irregular wave propagation over shoal," *J. of Waterway, Port, Coastal, and Ocean Engineering*, 116, 324-340.

Patrick, D. A. and Wiegel, R. L., 1955, "Amphibian tractors in the surf," *Proceedings of the 1st Conference on Ships and Waves*, Council on Wave Research and American Society of Naval Architects and Marine Engineers, 397-422.

Penney, W. G. and Price, A. T., 1952, "The diffraction theory of sea waves and the shelter afforded by breakwaters," *Philosophical Transactions of Royal Society of London A*, 244, 236-253.

Radder, A. C., 1979, "On the parabolic equation method for water-wave propagation," *J. of Fluid Mechanics*, 95, 159-176.

Radder, A. C. and Dingemans, M. W., 1985, "Canonical equations for almost periodic, weakly nonlinear gravity waves," *Wave Motion*, 7, 473-485.

Shapiro, R., 1970, "Smoothing, filtering, and boundary effects," *Review of Geophysics and Space Physics*, 8, 359-387.

Smith, R. and Sprinks, T., 1975, "Scattering of surface waves by a conical island," *J. of Fluid Mechanics*, 72, 373-384.

Sommerfeld, A., 1896, "Mathematische theorie der diffraction," *Math. Annalen. Bd.*, 47, 317-374.

Southgate, H. N., 1985, "A harbor ray model of wave refraction-diffraction," *J. of Waterway, Port, Coastal, and Ocean Engineering*, 111, 29-44.

Suh, K. D. and Dalrymple, R. A., 1993, "Application of angular spectrum model to simulation of irregular wave propagation," *J. of Waterway, Port, Coastal, and Ocean Engineering*, 119, 505-520.

Suh, K. D., Dalrymple, R. A., and Kirby, J. T., 1990, "An angular spectrum model for propagation of Stokes waves," *J. of Fluid Mechanics*, 22, 205-232.

Svendsen, I. A., 1984, "Wave heights and set-up in a surf zone," *Coastal Engineering*, 8, 303-329.

Sverdrup, H. U. and Munk, W. H., 1947, "Wind, sea, and swell theory of relationships in forecasting," *U.S. Dept. of the Navy Hydrographic Office Publication* No. 601.

Thomas, L. H., 1949, "Elliptic problems in linear difference equations over a network," *Watson Sci. Comput. Lab. Rept.*, Columbia University.

Thornton, E. B. and Guza, R. T., 1983, "Transformation of wave height distribution," *J. of Geophysical Research*, 88, 5925-5938.

Vincent, C. L. and Briggs, M. J., 1989, "Refraction and diffraction of irregular waves over a mound," *J. of Waterway, Port, Coastal, and Ocean Engineering*, 115, 269-284.

Watanabe, A., Hara, T., and Horikawa, K., 1984, "Study on breaking condition for compound wave trains," *Coastal Engineering in Japan*, 27, 71-82.

Weggel, J. R., 1972, "Maximum breaker height," *J. of Waterways, Harbors and Coastal Engineering Division*, 98, 529-548.

Wei, G. and Kirby, J. T., 1994, "A time-dependent numerical code for extended Boussinesq equations," *Research Report No. CACR-94-02*, Center For Applied Coastal Research, University of Delaware.

Appendix A

PARABOLIC APPROXIMATIONS FOR BREAKING WAVES

Parabolic Approximations for Monochromatic Breaking Waves

For monochromatic breaking waves, the mild-slope equation (4.9) can be used to solve the problem. When the deviation of the waves from the main direction is small and there is no reflection, we can use parabolic approximations and have only minor errors but great efficiency. The sudden increase of the energy dissipation rates at the breaking point does not cause any reflection, and the numerical discontinuities of the energy dissipation rates caused by wave breaking and shoaling do not cause any numerical problem in the parabolic approximations.

We extract the harmonic term with the wavenumber k_0 from the velocity potential $\hat{\phi}$ as

$$\hat{\phi}(x,y) = \check{\phi}(x,y)e^{i\int k_0 dx} \tag{A.1}$$

where $k_0(x)$ represents some weighted average of $k(x,y)$ along the transverse y-direction. The assumption of a mild slope gives the following order of magnitude:

$$\frac{|\nabla h|}{k_0 h} = O(\delta^2), \quad \frac{|\frac{\partial \check{\phi}}{\partial x}|}{k_0|\check{\phi}|} = O(\delta^2), \quad \frac{|\frac{\partial \check{\phi}}{\partial y}|}{k_0|\check{\phi}|} = O(\delta) \tag{A.2}$$

So, when terms to $O(\delta^2)$ are retained, we get the parabolic mild-slope equation for monochromatic breaking waves:

$$\frac{\partial}{\partial y}(CC_g\frac{\partial \check{\phi}}{\partial y}) + 2ik_0CC_g\frac{\partial \check{\phi}}{\partial x} + \{(k^2 - k_0^2)CC_g + i(\frac{\partial}{\partial x}(k_0CC_g) + \omega D_b)\}\check{\phi} = 0 \quad \text{(A.3)}$$

where the energy dissipation rate D_b is

$$D_b = 2\gamma\omega\frac{(\frac{\omega}{gh}|\check{\phi}|)^2}{1 - (\frac{\omega}{gh}|\check{\phi}|)^2} \quad \text{(A.4)}$$

We need to find the direction of the waves from velocity potential $\check{\phi}$ which has a relation:

$$\hat{\phi}(x,y) = A(x,y)e^{i(\int k\cos\theta dx + k\sin\theta dy)} = \check{\phi}(x,y)e^{i\int k_0 x} \quad \text{(A.5)}$$

Then we have

$$\frac{\frac{\partial \hat{\phi}}{\partial y}}{\frac{\partial \hat{\phi}}{\partial x}} = \frac{ik\sin\theta A + \frac{\partial A}{\partial y}}{ik\cos\theta A + \frac{\partial A}{\partial x}} = \tan\theta + O(\delta^2) \quad \text{(A.6)}$$

and

$$\frac{\frac{\partial \hat{\phi}}{\partial y}}{\frac{\partial \hat{\phi}}{\partial x}} = \frac{\frac{\partial \check{\phi}}{\partial y}}{\frac{\partial \check{\phi}}{\partial x} + ik_0\check{\phi}} = \frac{\frac{\partial \check{\phi}}{\partial y}}{ik_0\check{\phi}} + O(\delta^2) \quad \text{(A.7)}$$

So, we have

$$\theta = \arctan(\frac{\frac{\partial \check{\phi}}{\partial y}}{ik_0\check{\phi}}) \quad \text{(A.8)}$$

We use the Crank-Nicolson method to discretize the two-dimensional parabolic equation (A.3) so we get the following equation:

$$A\check{\phi}_{i+1,j-1} + B\check{\phi}_{i+1,j} + C\check{\phi}_{i+1,j+1} = D \quad \text{(A.9)}$$

where

$$\begin{aligned} A &= \frac{1}{4(\Delta y)^2}\{(CC_g)_{i,j} + (CC_g)_{i+1,j}\} \\ &\quad -\frac{1}{16(\Delta y)^2}\{(CC_g)_{i,j+1} - (CC_g)_{i,j-1}\end{aligned}$$

$$
\begin{aligned}
& +(CC_g)_{i+1,j+1} - (CC_g)_{i+1,j-1}\} \\
B &= -\frac{1}{2(\Delta y)^2}\{(CC_g)_{i,j} + (CC_g)_{i+1,j}\} \\
& +\frac{1}{4}\{((k^2 - k_0^2)CC_g)_{i,j} + ((k^2 - k_0^2)CC_g)_{i+1,j}\} \\
& +i\frac{1}{2\Delta x}\{(k_0 CC_g)_{i,j} + 3(k_0 CC_g)_{i+1,j}\} + \frac{1}{2}i\omega D_{bi,j} \\
C &= \frac{1}{4(\Delta y)^2}\{(CC_g)_{i,j} + (CC_g)_{i+1,j}\} \\
& +\frac{1}{16(\Delta y)^2}\{(CC_g)_{i,j+1} - (CC_g)_{i,j-1} + (CC_g)_{i+1,j+1} - (CC_g)_{i+1,j-1}\} \\
D &= -\frac{1}{4}\{(CC_g)_{i,j} + (CC_g)_{i+1,j}\}\{\check{\phi}_{i,j-1} - 2\check{\phi}_{i,j} + \check{\phi}_{i,j+1}\} \\
& -\frac{1}{16(\Delta y)^2}\{(CC_g)_{i,j+1} - (CC_g)_{i,j-1} \\
& +(CC_g)_{i+1,j+1} - (CC_g)_{i+1,j-1}\}\{\check{\phi}_{i,j+1} - \check{\phi}_{i,j-1}\} \\
& +[-\{\frac{1}{4}\{(k^2 - k_0^2)CC_g)_{i,j} + ((k^2 - k_0^2)CC_g)_{i+1,j}\} \\
& +i\frac{1}{2\Delta x}\{3(k_0 CC_g)_{i,j} + (k_0 CC_g)_{i+1,j}\} - \frac{1}{2}i\omega D_{bi,j}]\check{\phi}_{i,j}
\end{aligned} \tag{A.10}
$$

and where the subscripts i and j represent the spatial indices in $i\Delta x$ and $j\Delta y$. The Crank-Nicolson method is implicit and unconditionally stable. The local error is $O(\Delta x)^2$ or $O(\Delta y)^2$. The energy dissipation rates $D_{bi,j}$ are used in computing the velocity potentials $\check{\phi}_{i+1,j}$.

For one-dimensional cases, equation (A.3) becomes

$$
\frac{\partial \check{\phi}}{\partial x} = -\frac{\{\frac{\partial}{\partial x}(k_0 CC_g) + \omega D_b\}\check{\phi}}{2k_0 CC_g} = G(\check{\phi}) \tag{A.11}
$$

The Euler predictor-corrector method is used to discretize one-dimensional eqaution (A.11). In the predictor step, we have

$$
\check{\phi}_{i+1} = \check{\phi}_i + \Delta x G_i \tag{A.12}
$$

and in the corrector step, we have

$$
\check{\phi}_{i+1} = \check{\phi}_i + \frac{\Delta x}{2}\{G_i + G_{i+1}\} \tag{A.13}
$$

If the errors between predicted and corrected values are small enough, we proceed to the next spatial step; otherwise, we repeat correcting until we get the small errors. The local error of the Euler predictor-corrector method, (A.12) and (A.13), is $O(\Delta x)^3$.

Parabolic Approximations for Random Breaking Waves

For random breaking waves we can use the parabolic equation (A.3). First, we separate the whole spectrum into several spectra with density $\Delta S(f_l)$ and width Δf_l and, if there is directional spreading, separate with several spreading widths $\Delta\theta_m$ (see Figure A.1)

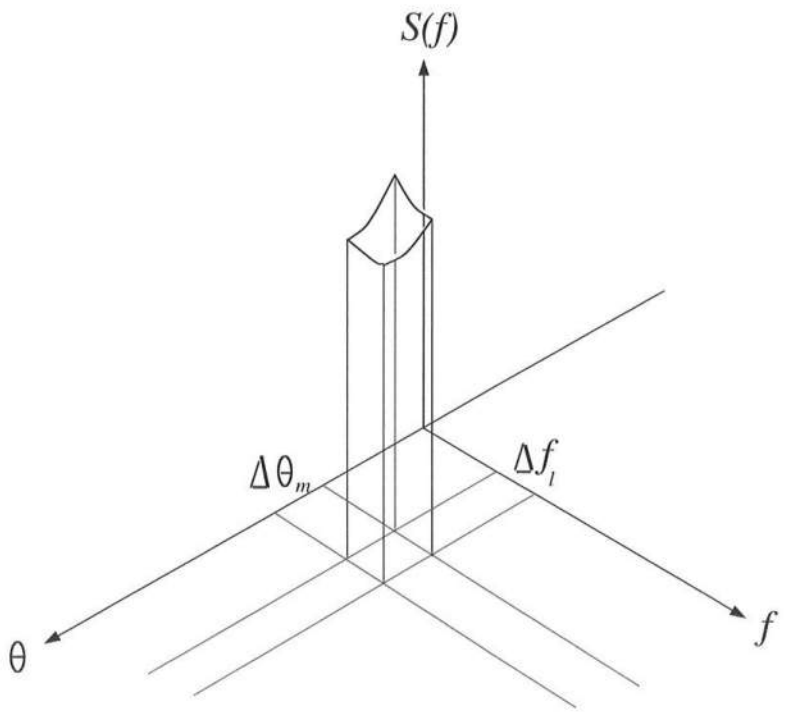

Figure A.1: Separation of directional power spectra

So, with each spectrum with each spreading width, we get the amplitude of water surface elevation as

$$a_{lm} = \sqrt{2S(f_l)\Delta f_l \Delta\theta_m} \tag{A.14}$$

The initial condition can be specified as

$$\check{\phi}_{1,j} = -i\frac{a_{lm}g}{\omega_l}, \quad j = 1, \cdots, J \tag{A.15}$$

By using the Crank-Nicolson method to discretize equation (A.3) (two-dimensional) or the Euler predictor-corrector method to discretize (A.11) (one-dimensional), we obtain the velocity potential $\check{\phi}_{i,j}$. At each step (i), we add the whole wave amplitudes as

$$|\check{\phi}| = |\sum_{l=1}^{L}\sum_{m=1}^{M}\check{\phi}_{lm}| \tag{A.16}$$

and test the breaking criterion; that is, if the ratio of total wave height to water depth is greater than the criterion, then we compute the energy dissipation rate D_b for each wave spectrum with each spreading width by

$$D_b = 2\gamma\omega_l\frac{(\frac{|\eta|_{lm}}{h})^2}{1-(\frac{|\eta|_{lm}}{h})^2} = 2\gamma\omega_l\frac{(\frac{\omega_l}{gh}|\check{\phi}_{lm}|)^2}{1-(\frac{\omega_l}{gh}|\check{\phi}_{lm}|)^2} \tag{A.17}$$

We get the propagation direction waves θ by

$$\theta_{lm} = \arctan(\frac{\frac{\partial\check{\phi}_{lm}}{\partial y}}{ik_0\check{\phi}_{lm}}) \tag{A.18}$$

We compute the velocity potential $\check{\phi}_{i+1,j}$.